



저작자표시-비영리-변경금지 2.0 대한민국

이용자는 아래의 조건을 따르는 경우에 한하여 자유롭게

- 이 저작물을 복제, 배포, 전송, 전시, 공연 및 방송할 수 있습니다.

다음과 같은 조건을 따라야 합니다:



저작자표시. 귀하는 원저작자를 표시하여야 합니다.



비영리. 귀하는 이 저작물을 영리 목적으로 이용할 수 없습니다.



변경금지. 귀하는 이 저작물을 개작, 변형 또는 가공할 수 없습니다.

- 귀하는, 이 저작물의 재이용이나 배포의 경우, 이 저작물에 적용된 이용허락조건을 명확하게 나타내어야 합니다.
- 저작권자로부터 별도의 허가를 받으면 이러한 조건들은 적용되지 않습니다.

저작권법에 따른 이용자의 권리는 위의 내용에 의하여 영향을 받지 않습니다.

이것은 [이용허락규약\(Legal Code\)](#)을 이해하기 쉽게 요약한 것입니다.

[Disclaimer](#)

Master's Thesis

Photoinduced electron/energy transfer-reversible  
addition-fragmentation chain transfer (PET-RAFT)  
using purely organic photocatalysts in the presence  
of oxygen

Yuna Song

Department of Materials Science and Engineering

Graduate School of UNIST

2020

Photoinduced electron/energy transfer-reversible  
addition-fragmentation chain transfer (PET-  
RAFT) using purely organic photocatalysts in the  
presence of oxygen

Yuna Song

Department of Materials Science and Engineering

Graduate School of UNIST

Photoinduced electron/energy transfer-reversible  
addition-fragmentation chain transfer (PET-  
RAFT) using purely organic photocatalysts in the  
presence of oxygen

A thesis/dissertation  
submitted to the Graduate School of UNIST  
in partial fulfillment of the  
requirements for the degree of  
Master of Science

Yuna Song

November 27, 2019

Approved by



Advisor

Min Sang Kwon

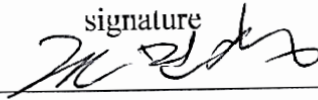
Photoinduced electron/energy transfer-reversible  
addition-fragmentation chain transfer (PET-  
RAFT) using purely organic photocatalysts in the  
presence of oxygen

Yuna Song

This certifies that the thesis/dissertation of Yuna Song is approved.

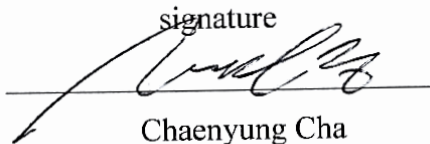
November 27, 2019

signature



Advisor: Min Sang Kwon

signature



Chaenyung Cha

signature



Wonjoo Lee

## Abstract

The necessity of a sustainable polymerization method renders a synthesis method to be more simple, efficient, and green. Reversible addition-fragmentation chain transfer (RAFT) polymerization is a typical method of living radical polymerization. This can control the degree of polymerization and the molecular weight depending on the reaction time and obtain the narrow molecular weight distribution. Recently, photoinduced electron/energy transfer (PET)-RAFT polymerization using photocatalysts has shown the excellent oxygen tolerance with use of transition metal-based catalysts, such as iridium or ruthenium complex. However, this approach is not effective for sustainable polymerization owing to the metal contaminations and hazards of toxicity, which necessitate the purification to remove residual transition metals after reaction.

Here, we discovered purely organic photocatalysts (OPC) with light absorption in the visible light region. The well-designed highly efficient OPC provides excellent control and narrow molecular weight distributions for PET-RAFT at extremely low catalyst loadings as well as low-energy light irradiation conditions, without additional reducing agents unlike other OPCs reported. In addition, by depth experimental and computational study, we present the following key factors showing the excellent oxygen tolerance with ppm-level catalyst loadings: the strong visible-light absorption and efficient generation of long-lived triplet states of the OPC, the oxidation stability and short retardation of chain-transfer agent (CTA), such as trithiocarbonate-based CTA.



## Contents

**Abstract**

**List of Figures**

**List of Tables**

<b>I. Introduction</b> .....	1
<b>II. Development of OPCs for PET-RAFT polymerizations</b> .....	6
<b>III. Experimental detail</b> .....	8
3.1 Materials .....	8
3.2 Instrumentation .....	9
3.3 Syntheses of 4DP-IPN .....	18
3.4 Experimental procedure .....	19
<b>IV. Results and discussion</b> .....	24
4.1 OPCs design logic.....	24
4.2 Polymerization studies under Argon.....	29
4.3 Oxygen tolerance .....	37
4.4 Oxygen tolerance of organic photoredox catalyst.....	41
4.5 Experimental validation of the outstanding performance of 4DP-IPN .....	45
4.6 UV-Vis and PL spectra, CV curves, and <sup>1</sup> H-NMR and <sup>13</sup> C-NMR spectra of selected OPCs and GPC traces and <sup>1</sup> H-NMR spectra of the resulting polymers .....	50
<b>V. Conclusion</b> .....	71
<b>VI. References</b> .....	72



## List of Figures

**Figure 1.** Concept of poly(methyl methacrylate) (PMMA) for PET-RAFT polymerization. Well-designed highly efficient OPC, 4DP-IPN, offers excellent oxygen tolerance, control and narrow molecular weight distributions of PMMA for PET-RAFT polymerization at very low catalyst loadings under visible-light irradiation conditions (*Reprinted with permission from Reference 1. Copyright 2019. American Chemical Society.*).

**Figure 2.** (a) Thiocarbonylthio (TCT) compounds which are reversible chain transfer agent (CTA)s for traditional RAFT polymerization activated via radical. The mechanisms for (b) conventional RAFT polymerization. The activated and deactivated mechanisms excluding RAFT equilibrium for photo-RAFT; (c) Photo-iniferter polymerization and (d) PET-RAFT polymerization which is composed of electron or energy transfer.

**Figure 3.** Previously reported structures of organic photocatalysts for PET-RAFT polymerization (*Reprinted with permission from Reference 1. Copyright 2019. American Chemical Society.*).

**Figure 4.** OPCs library developed in our recent work.

**Figure 5.** Summary of the development of organic photocatalysts for PET-RAFT polymerizations.

**Figure 6.** Example of calibration of GPC system.

**Figure 7.** Photophysical model to describe the dynamics and yields. States are given as capital letters; rate constants use the symbol “k”. The energy difference between the lowest excited singlet and triplet states is given as  $\Delta E$ .

**Figure 8.** Representative CV demonstrating a reversible (left) and an irreversible (right) redox behavior.<sup>38</sup>

**Figure 9.** CV curve of ferrocene recorded in our lab.

**Figure 10.** Syntheses scheme of 4DP-IPN.

**Figure 11.** Graphical Supporting Information for General Procedure for PET-RAFT Polymerization of MMA.

**Figure 12.** Proposed mechanisms for the PET-RAFT polymerization. <sup>3</sup>PC, the lowest triplet excited state of a photocatalyst; <sup>1/3</sup>PC, the lowest singlet and/or triplet excited states of a photocatalyst. (*Reprinted with permission from Reference 1. Copyright 2019. American Chemical Society.*).

**Figure 13.** General platform of the proposed OPCs, indicating the requirements for PET-RAFT

polymerization. (Reprinted with permission from **Reference 1**. Copyright 2019. American Chemical Society.).

**Figure 14.** Structures and properties of OPCs studied in the current work, selected from our OPC library. (Reprinted with permission from **Reference 1**. Copyright 2019. American Chemical Society.).

**Figure 15.** UV-Vis spectra (left) and CV curves (right) of (a) CPADB and (b) CDTPA. UV-Vis measurements were performed in DMSO with [CTA] = 20  $\mu$ M. CV measurements were done in 0.2 mM CH<sub>3</sub>CN solution with 0.1 M nBu<sub>4</sub>NPF<sub>6</sub> as supporting electrolyte at a scan rate of 100 mV/s.

**Figure 16.** Properties of CPADB and CDTPA: Molecular geometries in S<sub>0</sub> and T<sub>1</sub> (the latter is exclusively described by a HOMO→LUMO excitation); corresponding frontier MOs. Adiabatic and vertical transition energies in DMF.

**Figure 17.** Pictures of (a) individual parts and our LED set-ups in operation (b) under blue light and (c) under green light. (d) Basic information of photodiode for measuring the light intensity of the excitation light sources (blue and green LEDs) (e) Normalized emission spectra for the blue LEDs (top, maximum intensity wavelength = ca. 455 nm) and green LEDs (bottom, maximum intensity wavelength = ca. 515 nm).

**Figure 18.** (a) Negative control experiments of PET-RAFT of MMA in the presence of argon and air using CPADB. (b) <sup>1</sup>H-NMR spectra and GPC traces of the reaction mixtures obtained after PET-RAFT polymerizations of MMA under air (up) and argon (bottom).

**Figure 19.** Kinetic plots for PET-RAFT polymerization of MMA under Ar using 4DP-IPN (5 ppm). (a) ln([M]<sub>0</sub>/[M]<sub>t</sub>) versus reaction time. (b) M<sub>n</sub> versus conversion (black circle) and M<sub>w</sub>/M<sub>n</sub> versus conversion (red circle); for GPC traces at different reaction, see inset of **Figure 22c**. (c) Light ON/OFF experiment for PET-RAFT polymerization of MMA using CPADB and 4DP-IPN of 5 ppm. (d) GPC traces of PMMA (black) and diblock of PMMA-*b*-PMMA (red) (Reprinted with permission from **Reference 1**. Copyright 2019. American Chemical Society.).

**Figure 20.** Kinetic plots for PET-RAFT polymerizations of MMA in the presence of argon using Ir(ppy)<sub>3</sub> of 1 ppm. (a) ln([M]<sub>0</sub>/[M]<sub>t</sub>) versus reaction time. (b) M<sub>n</sub> versus conversion (black circle) and M<sub>w</sub>/M<sub>n</sub> versus conversion (blue circle). (c) GPC traces at different reaction time. (d) Light "ON"/"OFF" experiment for PET-RAFT polymerization of MMA using CPADB and Ir(ppy)<sub>3</sub> of 1 ppm. (e) <sup>1</sup>H-NMR spectra at different reaction time.

**Figure 21.** GPC traces of PMMA and diblock of PMMA-*b*-PMMA and <sup>1</sup>H-NMR spectra of washed (middle) and in-situ (bottom) 1<sup>st</sup> chain and in-situ (top) 2<sup>nd</sup> chain using (a) Ir(ppy)<sub>3</sub> of 1 ppm and (b) 4DP-IPN of 5 ppm under argon.

**Figure 22.** Kinetic plots for PET-RAFT polymerization of MMA under air for 4DP-IPN (5 ppm). (a)  $\ln([M]_0/[M]_t)$  versus a reaction time. (b)  $M_n$  versus conversion (black circle) and  $M_w/M_n$  versus conversion (red circle). Inset shows GPC traces at different reaction times. Experimental condition: [MMA]:[CPADB]:[4DP-IPN] = 200:1:0.001 in DMSO. (c)  $^1\text{H-NMR}$  spectra of the reaction mixtures obtained after the PET-RAFT polymerization of 18 h without purifications under air (up) and Ar (bottom) in the presence of CPADB, MMA, and 4DP-IPN of 5 ppm (*Reprinted with permission from Reference 1. Copyright 2019. American Chemical Society.*).

**Figure 23.**  $^1\text{H-NMR}$  spectra of the polymerization mixtures using CPADB and 4DP-IPN (5 ppm) at different reaction times. Suggested mechanism for the photo-oxidation of CPADB is given in the top.

**Figure 24.** Kinetic plots for PET-RAFT polymerizations of MMA in the presence of air using  $\text{Ir}(\text{ppy})_3$  of 1 ppm. (a)  $\ln([M]_0/[M]_t)$  versus a reaction time. (b)  $M_n$  versus conversion (black circle) and  $M_w/M_n$  versus conversion (blue circle). (c) GPC traces at a different reaction time. (d)  $^1\text{H-NMR}$  spectra of kinetic study at a different reaction time.

**Figure 25.** (a) Results of PET-RAFT polymerization of MMA in the presence of CDTPA using 4DP-IPN of 5 ppm under argon. All polymerizations were performed at room temperature under a 3 W blue LED (455 nm, ca. 2.5 mW/cm<sup>2</sup>). (b)  $^1\text{H-NMR}$  spectra and GPC traces of the reaction mixtures are obtained after PET-RAFT polymerizations of MMA.

**Figure 26.** (a) Results of PET-RAFT polymerizations of MMA in the presence of CDTPA using 4DP-IPN under Ar and/or air. All polymerizations were performed at room temperature under a 3 W green LED (515 nm, ca. 0.5 mW/cm<sup>2</sup>). Polymerizations under Ar were carried out in a sealed 20 mL vial with a total liquid volume of 2 mL (1:1, v/v of MMA/DMSO). Polymerizations under air were conducted in a sealed 4 mL vial with a total liquid volume of 3 mL. (b)  $^1\text{H-NMR}$  spectra of the reaction mixtures obtained after PET-RAFT polymerizations of 6 h without purifications under air (up) and Ar (bottom) in the presence of CDTPA and MMA with/without 4DP-IPN of 5 ppm (*Reprinted with permission from Reference 1. Copyright 2019. American Chemical Society.*).

**Figure 27.** (a) Chain extensions of PMMA in the presence of air using CDTPA and 4DP-IPN of 5 ppm. (b)  $^1\text{H-NMR}$  spectra of washed (middle) and in-situ (bottom) 1<sup>st</sup> chain and in-situ (top) 2<sup>nd</sup> chain under air. (c) GPC traces (right) of PMMA (black) and diblock of PMMA-*b*-PMMA (red) under air.

**Figure 28.** Photophysical and electrochemical properties of 4DP-IPN. (a) UV-Vis absorption (dark gray line) in DMSO ( $2 \times 10^{-5}$  M) and photoluminescence (PL) at room temperature (dark gray line), gated PL at 68 K (red line), and PL at 68 K (green line) in  $\text{CH}_3\text{CN}$  ( $2 \times 10^{-5}$  M). (b) Cyclic voltammetry of 2.0 mM 4DP-IPN in  $\text{CH}_3\text{CN}$  containing 0.1 M nBu<sub>4</sub>NPF<sub>6</sub> on a glassy carbon working electrode at variable scan rates from 20 to 100 mV/s. (c) Term diagrams of 4DP-IPN as obtained from the

experiments (in CH<sub>3</sub>CN) and by TD-DFT (in DMF) (*Reprinted with permission from Reference 1. Copyright 2019. American Chemical Society.*).

**Figure 29.** PL emission spectra of 4DP-IPN in CH<sub>3</sub>CN at r.t. (a) unpurged (b) after purging 10 min with dry N<sub>2</sub> gas,  $\lambda_{exc} = 387$  nm.

**Figure 30.** PL decays of 4DP-IPN in DMSO at RT,  $\lambda_{exc} = 405$  nm,  $\lambda_{det} = 540$  nm; experiment (red), mono-exponential fits (black). (a) unpurged,  $\nu_{rep} = 50$  kHz,  $\tau = 5.1$   $\mu$ s. (b) after purging (10 min, dry N<sub>2</sub> gas),  $\nu_{rep} = 1$  kHz,  $\tau = 82.8$   $\mu$ s.

**Figure 31.** PL emission spectra of 4DP-IPN in DMSO at r.t. (a) unpurged (b) after 10 min purging with dry N<sub>2</sub> gas,  $\lambda_{exc} = 387$  nm.

**Figure 32.** PL decays of 4DP-IPN in DMSO at RT,  $\lambda_{exc} = 405$  nm,  $\lambda_{det} = 540$  nm; experiment (red), mono-exponential fits (black). (a) unpurged,  $\nu_{rep} = 50$  kHz,  $\tau = 5.1$   $\mu$ s. (b) after purging (10 min, dry N<sub>2</sub> gas),  $\nu_{rep} = 1$  kHz,  $\tau = 82.8$   $\mu$ s.

**Figure 33.** Emission under continuous wave excitation and gated emission of 4DP-IPN in CH<sub>3</sub>CN at 65K.

**Figure 34.** PL Decays of 4DP-IPN in CH<sub>3</sub>CN at 65K, experiment (red), bi-exponential fits (black). (a) Phosphorescence decay,  $\lambda_{exc} = 405$  nm,  $\lambda_{det} = 560$  nm,  $\nu_{rep} = 0.33$  Hz.  $\tau_1 = 31$  ms ( $A_1 = 3.0 \cdot 10^{-1}$ , 17%),  $\tau_2 = 380$  ms ( $A_2 = 7.1 \cdot 10^{-1}$ , 83%). (b) Fluorescence decay,  $\lambda_{exc} = 405$  nm,  $\lambda_{det} = 525$  nm,  $\nu_{rep} = 2.5$  MHz.  $\tau_1 = 2.4$  ns ( $A_1 = 2.9 \cdot 10^{-1}$ , 56%),  $\tau_2 = 0.8$  ns ( $A_2 = 7.1 \cdot 10^{-1}$ , 44%).

**Figure 35.** Transient absorption (TA) experiment of 4DP-IPN was performed in CH<sub>3</sub>CN at r.t. (a) TA spectrum in the nanosecond temporal range, after pumping with 300 ps monochromatic pump pulses at 355 nm with 2  $\mu$ J pulse energy and a repetition rate of 500 Hz. The false color scale denotes green as zero signal, yellow as positive transient absorption (photo-induced absorption, PA) and blue as negative transient absorption (transient photobleach, PB). (b) Kinetic model for the simulation of the TA dynamics. Note that the slow processes from scheme 1 ( $k_{risc}$  and  $k_{T0}$ ) have been omitted because they cannot be obtained on a 100 ns time scale; note also that  $k_m = k_F + k_{nr}$ . Without measuring the PLQY, one cannot distinguish these processes leading to the same PA and PB dynamics. However, even without knowledge of PLQY, one can still get the ISC yield, defined as  $\Phi_{isc} = k_{isc} / (k_m + k_{isc})$ , directly from fitting the TA spectrum in panel (a). (c) t-SVD (eq. S13) of panel (a) (black solid lines in panel (c), and reproduction (black dashed lines) by a weighted superposition of the characteristic spectra for excited singlet and triplet states (blue and orange lines, defined acc. to eq. S14). (d) and (e) resulting dynamics of excited singlet and triplet states, according to eq. S12 (blue and orange symbols, respectively) and fitted dynamics according to panel b) (blue and orange solid lines, respectively).

**Figure 36.** UV-Vis and PL spectra of PCs were purchased commercially in DMSO (20  $\mu$ M).

**Figure 37.** UV-Vis and PL spectra of selected OPCs in DMF (20  $\mu$ M).

**Figure 38.** CV curves of PCs were purchased commercially in CH<sub>3</sub>CN (2 mM). For eosin Y and fluorescein, in CH<sub>3</sub>CN:H<sub>2</sub>O (1:1 v/v) (2 mM).

**Figure 39.** CV curves of selected OPCs in CH<sub>3</sub>CN (2 mM).

**Figure 40.** GPC traces of PET-RAFT polymerizations of MMA for **Table 2**. Experimental condition: [MMA]:[CPADB]:[Ir(ppy)<sub>3</sub>] = 200:1:0.0002 and [MMA]:[CPADB]:[OPC] = 200:1:0.001 in DMSO under a 3W 455 nm LED at room temperature under argon.

**Figure 41.** GPC traces of PET-RAFT polymerizations of MMA for **Table 2**. Experimental condition: [MMA]:[CPADB]:[Ir(ppy)<sub>3</sub>] = 200:1:0.0002 and [MMA]:[CPADB]:[OPC] = 200:1:0.001 in DMSO under a 3W 455 nm LED at room temperature under air.

**Figure 42.** <sup>1</sup>H-NMR spectra and GPC curves of the molecular weight controlled PMMA in the presence of argon using CPADB and 4DP-IPN of 5 ppm.

**Figure 43.** <sup>1</sup>H-NMR of Ir(ppy)<sub>3</sub> in CDCl<sub>3</sub> at r.t..

**Figure 44.** <sup>1</sup>H-NMR of eosin Y in CDCl<sub>3</sub> at r.t..

**Figure 45.** <sup>1</sup>H-NMR of fluorescein in CDCl<sub>3</sub> at r.t..

**Figure 46.** <sup>1</sup>H-NMR of 5Cz-BN in CDCl<sub>3</sub> at r.t..

**Figure 47.** <sup>1</sup>H-NMR of 4Cz-IPN in CDCl<sub>3</sub> at r.t..

**Figure 48.** <sup>1</sup>H-NMR of 4DP-IPN in CDCl<sub>3</sub> at r.t..

**Figure 49.** <sup>13</sup>C-NMR of 4DP-IPN in CDCl<sub>3</sub> at r.t..

**Figure 50.** <sup>1</sup>H-NMR of 2DP-BP in CDCl<sub>3</sub> at r.t..

**Figure 51.** <sup>1</sup>H-NMR of 2DHPZ-DPS in CDCl<sub>3</sub> at r.t..

**Figure 52.** <sup>1</sup>H-NMR of DMDP-TRZ in CDCl<sub>3</sub> at r.t..

**Figure 53.** In-situ <sup>1</sup>H-NMR of PMMA in the presence of CPADB, MMA, and Ir(ppy)<sub>3</sub> of 1 ppm under argon in CDCl<sub>3</sub> at r.t. (For **Table 2**. entry 1).

**Figure 54.** In-situ <sup>1</sup>H-NMR of PMMA in the presence of CPADB, MMA, and eosin Y of 5 ppm under argon in CDCl<sub>3</sub> at r.t. (For **Table 2**. entry 3).

**Figure 55.** In-situ <sup>1</sup>H-NMR of PMMA in the presence of CPADB, MMA, and fluorescein of 5 ppm under argon in CDCl<sub>3</sub> at r.t. (For **Table 2**. entry 5).

**Figure 56.** In-situ  $^1\text{H-NMR}$  of PMMA in the presence of CPADB, MMA, and 5Cz-BN of 5 ppm under argon in  $\text{CDCl}_3$  at r.t. (For **Table 2.** entry 7).

**Figure 57.** In-situ  $^1\text{H-NMR}$  of PMMA in the presence of CPADB, MMA, and 4Cz-IPN of 5 ppm under argon in  $\text{CDCl}_3$  at r.t. (For **Table 2.** entry 9).

**Figure 58.** In-situ  $^1\text{H-NMR}$  of PMMA in the presence of CPADB, MMA, and 4DP-IPN of 5 ppm under argon in  $\text{CDCl}_3$  at r.t. (For **Table 2.** entry 11).

**Figure 59.** In-situ  $^1\text{H-NMR}$  of PMMA in the presence of CPADB, MMA, and 2DP-BP of 5 ppm under argon in  $\text{CDCl}_3$  at r.t. (For **Table 2.** entry 13).

**Figure 60.** In-situ  $^1\text{H-NMR}$  of PMMA in the presence of CPADB, MMA, and 2DHPZ-DPS of 5 ppm under argon in  $\text{CDCl}_3$  at r.t. (For **Table 2.** entry 15).

**Figure 61.** In-situ  $^1\text{H-NMR}$  of PMMA in the presence of CPADB, MMA, and DMDP-TRZ of 5 ppm under argon in  $\text{CDCl}_3$  at r.t. (For **Table 2.** entry 17).

**Figure 62.** In-situ  $^1\text{H-NMR}$  of PMMA in the presence of CPADB, MMA, and  $\text{Ir(ppy)}_3$  of 1 ppm under air in  $\text{CDCl}_3$  at r.t. (For **Table 2.** entry 2).

**Figure 63.** In-situ  $^1\text{H-NMR}$  of PMMA in the presence of CPADB, MMA, and eosin Y of 5 ppm under air in  $\text{CDCl}_3$  at r.t. (For **Table 2.** entry 4).

**Figure 64.** In-situ  $^1\text{H-NMR}$  of PMMA in the presence of CPADB, MMA, and fluorescein of 5 ppm under air in  $\text{CDCl}_3$  at r.t. (For **Table 2.** entry 6).

**Figure 65.** In-situ  $^1\text{H-NMR}$  of PMMA in the presence of CPADB, MMA, and 5Cz-BN of 5 ppm under air in  $\text{CDCl}_3$  at r.t. (For **Table 2.** entry 8).

**Figure 66.** In-situ  $^1\text{H-NMR}$  of PMMA in the presence of CPADB, MMA, and 4Cz-IPN of 5 ppm under air in  $\text{CDCl}_3$  at r.t. (For **Table 2.** entry 10).

**Figure 67.** In-situ  $^1\text{H-NMR}$  of PMMA in the presence of CPADB, MMA, and 4DP-IPN of 5 ppm under air in  $\text{CDCl}_3$  at r.t. (For **Table 2.** entry 12).

**Figure 68.** In-situ  $^1\text{H-NMR}$  of PMMA in the presence of CPADB, MMA, and 2DP-BP of 5 ppm under air in  $\text{CDCl}_3$  at r.t. (For **Table 2.** entry 14).

**Figure 69.** In-situ  $^1\text{H-NMR}$  of PMMA in the presence of CPADB, MMA, and 2DHPZ-DPS of 5 ppm under air in  $\text{CDCl}_3$  at r.t. (For **Table 2.** entry 16).

**Figure 70.** In-situ  $^1\text{H-NMR}$  of PMMA in the presence of CPADB, MMA, and DMDP-TRZ of 5 ppm under air in  $\text{CDCl}_3$  at r.t. (For **Table 2.** entry 18).

## List of Tables

**Table 1.** Photophysical and electrochemical properties of OPCs in our library.

**Table 2.** Results for the PET-RAFT polymerization of MMA in the presence of different PCs at room temperature under Argon (Ar) and Air; 3 W Blue LED illumination (455 nm, ca. 2.5 mW/cm<sup>2</sup>)  
*(Reprinted with permission from **Reference 1**. Copyright 2019. American Chemical Society.)*

**Table 3.** Results of PET-RAFT polymerization of MMA in the presence of CPADB using 4DP-IPN of 1 ppm under argon. All polymerizations were performed at room temperature under a 3 W blue LED (455 nm, ca. 2.5 mW/cm<sup>2</sup>).

**Table 4.** Reproducibility test. Experiments were performed in many different set-ups by students in our group.

**Table 5.** Control of molecular weight of PMMA in the presence of argon using CPADB and 4DP-IPN of 5 ppm. <sup>1</sup>H-NMR spectra and GPC curves of the resulting polymers are in **Figure 42**.

**Table 6.** Chain extensions of PMMA in the presence of argon using Ir(ppy)<sub>3</sub> of 1 ppm and 4DP-IPN of 5 ppm.

**Table 7.** PLQY of 4DP-IPN at r.t. under N<sub>2</sub> purged condition.

## I. Introduction

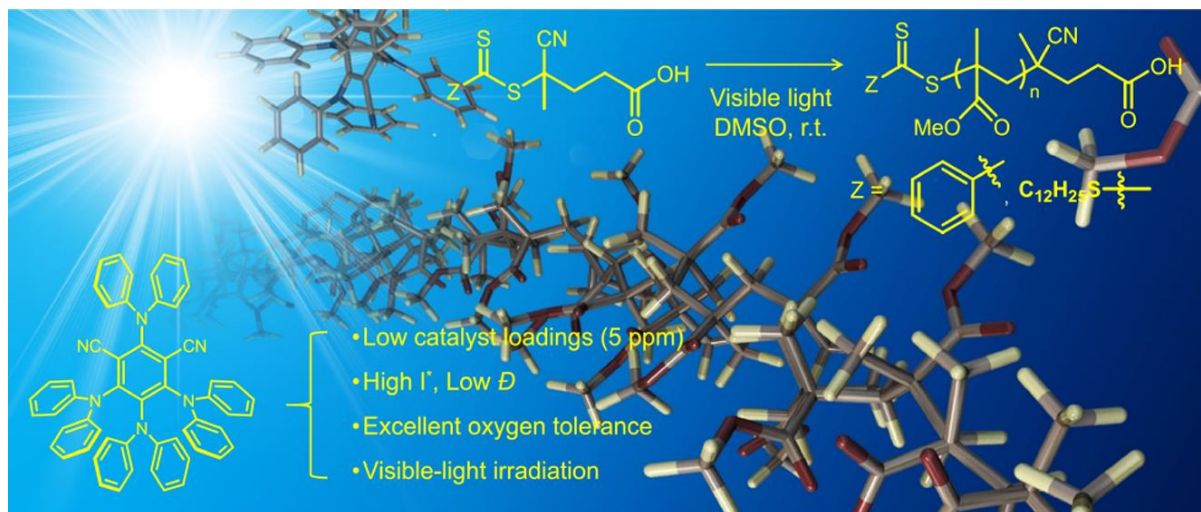


**Figure 1.** Concept of poly(methyl methacrylate) (PMMA) for PET-RAFT polymerization. Well-designed highly efficient OPC, 4DP-IPN, offers excellent oxygen tolerance, control and narrow molecular weight distributions of PMMA for PET-RAFT polymerization at very low catalyst loadings under visible-light irradiation conditions (*Reprinted with permission from Reference 1. Copyright 2019. American Chemical Society.*).

Reversible deactivation radical polymerization (RDRP), a controlled radical polymerization which includes reversible activation and deactivation process, has been rapidly developed to successfully encompass several other polymerizations such as nitroxide mediated polymerization (NMP), atom transfer radical polymerization (ATRP), and reversible addition-fragmentation chain transfer polymerization (RAFT). These polymerization techniques have a rapid initiation step and reduction of irreversible termination process<sup>2</sup>, which enable polymers to be well-defined with narrow molecular weight distributions. Moreover, as they have a high competency to diverse monomers and solvents, they are used in application in various fields, for example, additives, smart coatings, electronic devices, and drug delivery.<sup>3,4</sup>

Above all, photomediated controlled radical polymerization (photo-CRP) is an attractive process because it fulfills green chemistry with economic and environmental advantages by using low energy and proceeding at mild conditions with temporal/spatial control over chain growth.<sup>5-10</sup> Thus, this process is widely used in radiation curing, microelectronics, laser direct imaging technology, 3D printing, medicine, and imaging areas.<sup>11</sup> In the last few decades, there has been a rapid growth in developments of the various photo-CRPs such as photomediated atom transfer radical polymerizations (photo-



ATRP),<sup>12-14</sup> photomediated reversible addition-fragmentation chain transfer (photo-RAFT),<sup>15,16</sup> and many others.<sup>5-10</sup>

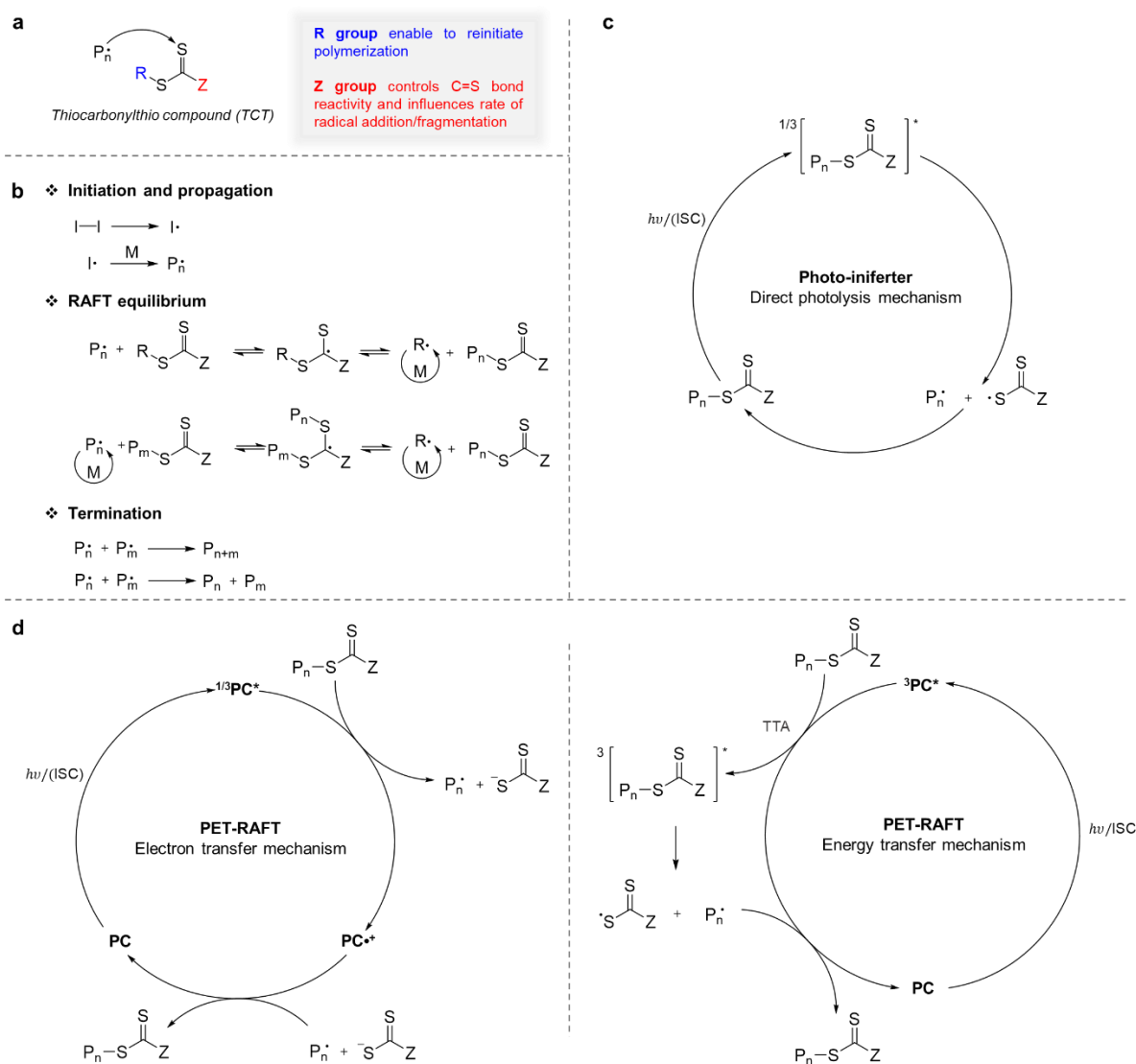
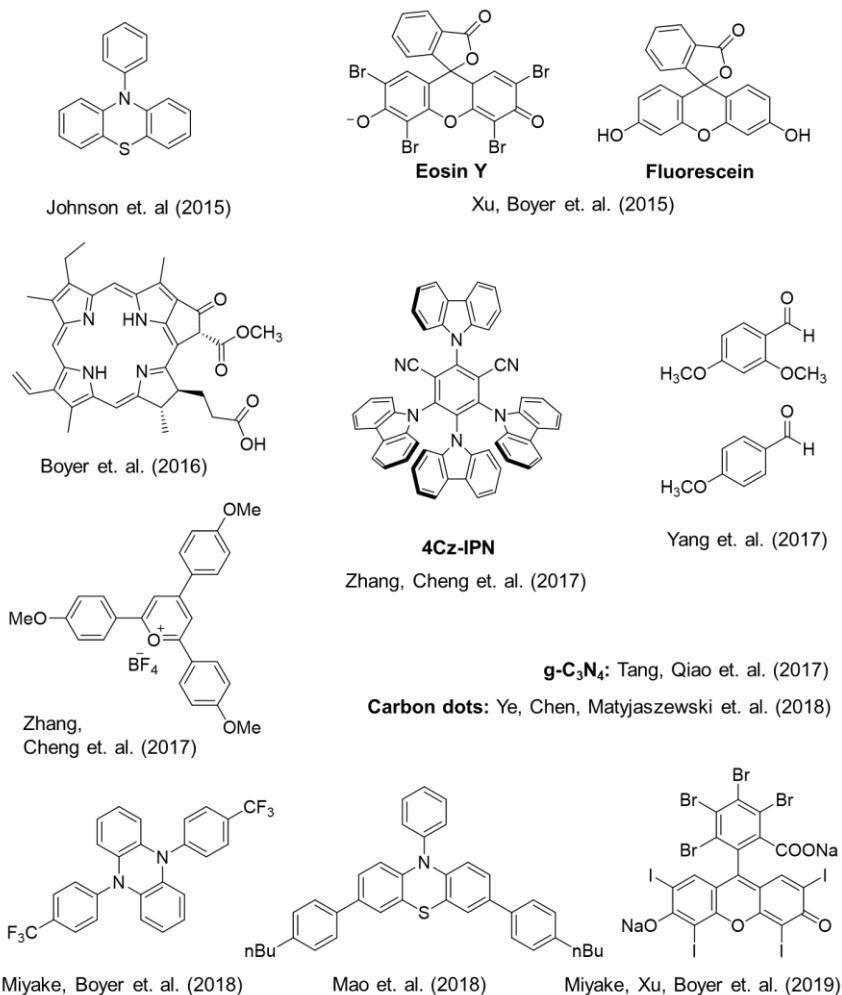


**Figure 2.** (a) Thiocarbonylthio (TCT) compounds which are reversible chain transfer agent (CTA)s for traditional RAFT polymerization activated via radical. The mechanisms for (b) conventional RAFT polymerization. The activated and deactivated mechanisms excluding RAFT equilibrium for photo-RAFT; (c) Photo-iniferter polymerization and (d) PET-RAFT polymerization which is composed of electron or energy transfer.

Since the RAFT has been introduced by Rizzardo, Moad, Thang and co-workers,<sup>2</sup> it has been widely recognized as a promising technique among the RDRP method owing to its novel use of a reversible chain transfer agent (CTA, i.e., RAFT agent) like a thiocarbonylthio compound (TCT) such as

dithiocarbonate, dithiocarbamate, trithiocarbonate, or xanthate (**Figure 2a** and **2b**). Furthermore, the rapid exchange between dormant and living chains leads to low ratios of rate constants of exchange to propagation, which results in narrow dispersity than other RDRPs.<sup>17</sup> Recently, many scientists have paid attention to light induced RAFT polymerization as a type of photo-RAFT. Unlike conventional RAFT, this could be initiated at low temperature that eliminates heating process for thermal initiation (**Figure 2c** and **2d**). Among the light sources, ultraviolet (UV) light can initiate CTA, but UV light energy is so strong that decomposition of CTAs is occurred, leading to at least two different initiating or transfer mechanisms causing loss of end group fidelities.<sup>18</sup> Currently, softer irradiation source such as visible light is a more efficient way to activate CTAs. These light sources are safer, cheaper, and environmentally friendly system (low energy consumption, no ozone released, and high lifetimes).<sup>19</sup>

❖ Previous works in O-RAFT

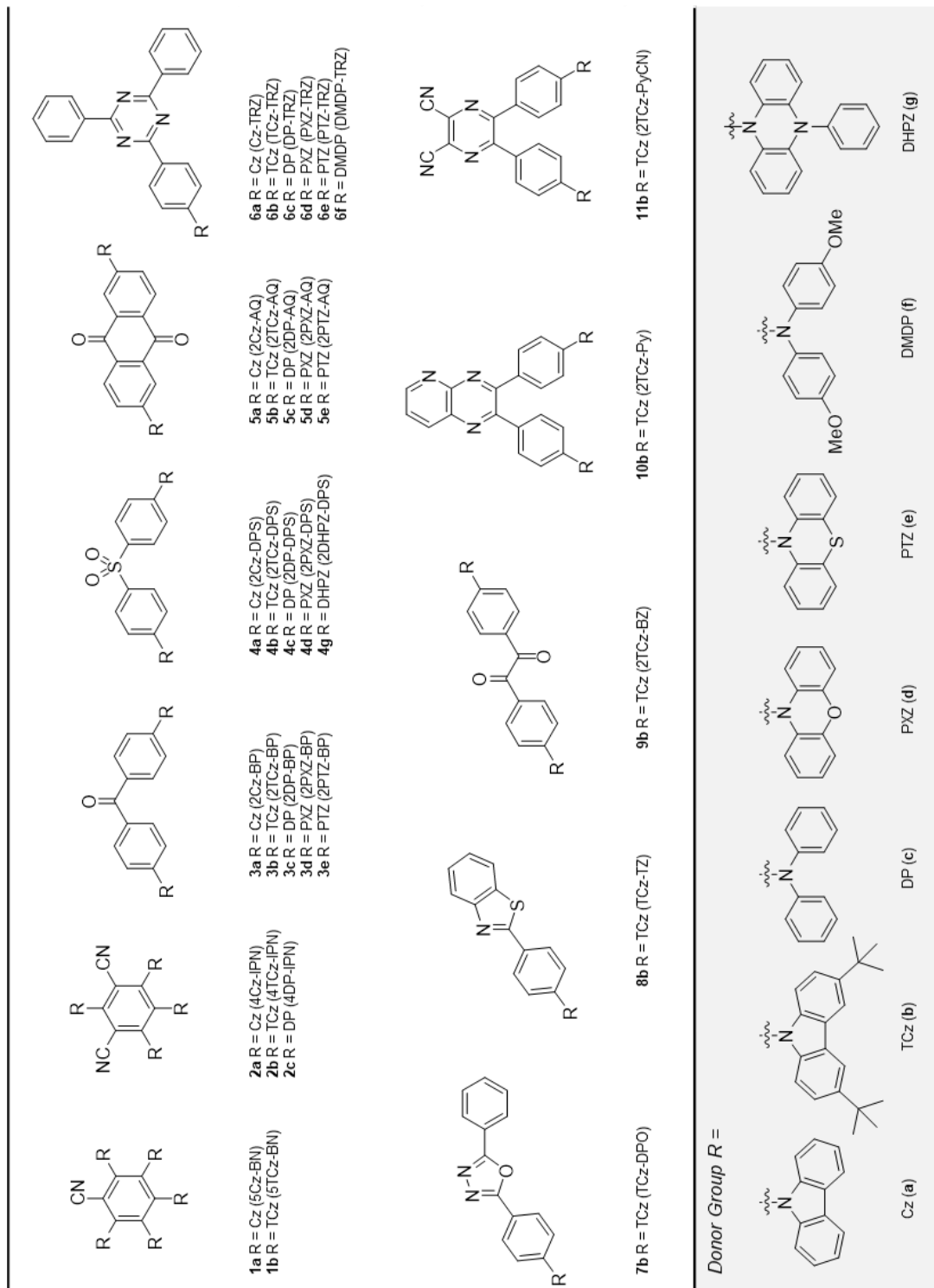


**Figure 3.** Previously reported structures of organic photocatalysts for PET-RAFT polymerization (Reprinted with permission from **Reference 1**. Copyright 2019. American Chemical Society.).

Since 2014, photoinduced electron/energy transfer RAFT (PET-RAFT) using photocatalysts developed by Boyer group<sup>20</sup> is considered as a versatile and greener approach. Also, it shows oxygen tolerance (i.e., non-deoxygenation system), broad compatibility to the mild reaction conditions (e.g., monomers, light sources, and photocatalysts), recyclability of photocatalysts, temporal/spatial control, high-molecular-weight polymers, and excellent end group fidelities.<sup>21</sup> Notably, the PET-RAFT could be polymerized without additional radical initiators because photocatalysts act as the electron/energy transfer from photocatalysts to CTAs. This strategy provides not only reducing the industrial cost by excluding chemical initiators or recycling the photocatalysts, but also decreasing the undesired side reactions or byproducts from the radical initiators that could contaminate the reaction culture. Although the photocatalyst is essential for PET-RAFT, the amounts of catalyst loadings are as low as ppm-level.

Thus, there have been many studies to discover more efficient photocatalysts for this system. Up to date, the transition metal-based catalysts were widely used for PET-RAFT with the oxygen tolerance. However, its toxicity and metal contamination issues still limited the broad use, although this could be overcome by additional purification.<sup>23,24</sup> To solve these drawbacks, pure OPCs have been suggested recently (**Figure 3**). However, when OPCs are used, high catalyst loadings are required, or additional reducing agents are required to exhibit the oxygen tolerance.

Herein, we present a highly efficient OPC, 4DP-IPN, by screening catalyst library of our model<sup>22</sup> that has been recently developed (**Figure 4**). This novel OPC successfully controls PET-RAFT polymerization of methyl methacrylate (MMA) at very low catalyst loadings (5 ppm) under visible-light irradiation, which is almost comparable to those of metal-based catalysts. In addition, we found that a trithiocarbonate-based CTA is more efficient CTA than dithiobenzoate-based CTA even in the presence of air without sacrificial reducing agents under weak green light irradiation conditions. We have emphasized that the essential elements for successful PET-RAFT with the excellent oxygen tolerance and ppm-level catalyst loadings are strong visible-light absorption of OPC, efficient generation of long-lived triplet states of OPC by highly twisted donor-acceptor moieties, and the photo-oxidation stability of a CTA.


**Figure 4.** OPCs library developed in our recent work.

## II. Development of OPCs for PET-RAFT polymerizations

To substitute the metal-based catalysts, organic dyes are widely suggested, such as rhodamine, eosin Y, fluorescein, Nile red, methylene blue, and 10-phenylphenothiazine (Ph-PTZ),<sup>14,23-32</sup> because of the absorption in the visible light, broad commercial availability, and low cost (**Figure 5**). Johnson and co-workers reported that Ph-PTZ is an effective OPC for the PET-RAFT polymerization. However, relatively high catalysts loadings around 200 ppm with respect to monomer (for Ir(ppy)<sub>3</sub>, 1 ppm or less) and UV-light irradiation is needed.<sup>23</sup> Chen group also use PTZ for PET-RAFT of fluorinated polymers under white irradiation, but this system also required high catalysts loadings (ca. 500 ppm).<sup>31</sup> Boyer and co-workers found that pheophorbide a (PheoA), an organic porphyrin which is proceeded from chlorophyll without any metal centre,<sup>25,33</sup> under red irradiation. In addition, they demonstrated that eosin Y and fluorescein act as OPCs and have oxygen tolerance in the presence of triethylamine as a sacrificial electron donor in a reductive pathway.<sup>24</sup> However, in this case, they experimented at very low oxygen volume system (0.2 ml oxygen gas volume in the vial). Miyake, Boyer and co-workers developed N,N-diaryl dithydrophenazines but they didn't identify the oxygen tolerance. Recently, Boyer group employed halogenated xanthene dyes at relatively low catalysts loadings (ca. 20 ppm) with good oxygen tolerance.<sup>32</sup>

Meanwhile, some organic agents are introduced because organic dyes have very low storage stability<sup>34</sup> and high possibility of degradation during the polymerization.<sup>35</sup> Zang, Cheng and co-workers reported 4Cz-IPN as OPC.<sup>36</sup> They also found 2,4,6-tri-(p-methoxyphenyl) pyrylium tetrafluoroborate under irradiation of various LED lights (purple, blue and white LEDs).<sup>27</sup> Yang and co-workers used benzaldehyde derivatives as photocatalysts.<sup>28</sup> However, all these cases required high catalysts loadings (ca. 250 ppm or very high).

Although there have been many attempts to discover new OPCs, high catalyst loadings are required in most OPCs. Also, the oxygen tolerance is not clearly observed excluding eosin Y (only in the presence of sacrificial electron donor) and halogenated xanthene dyes.

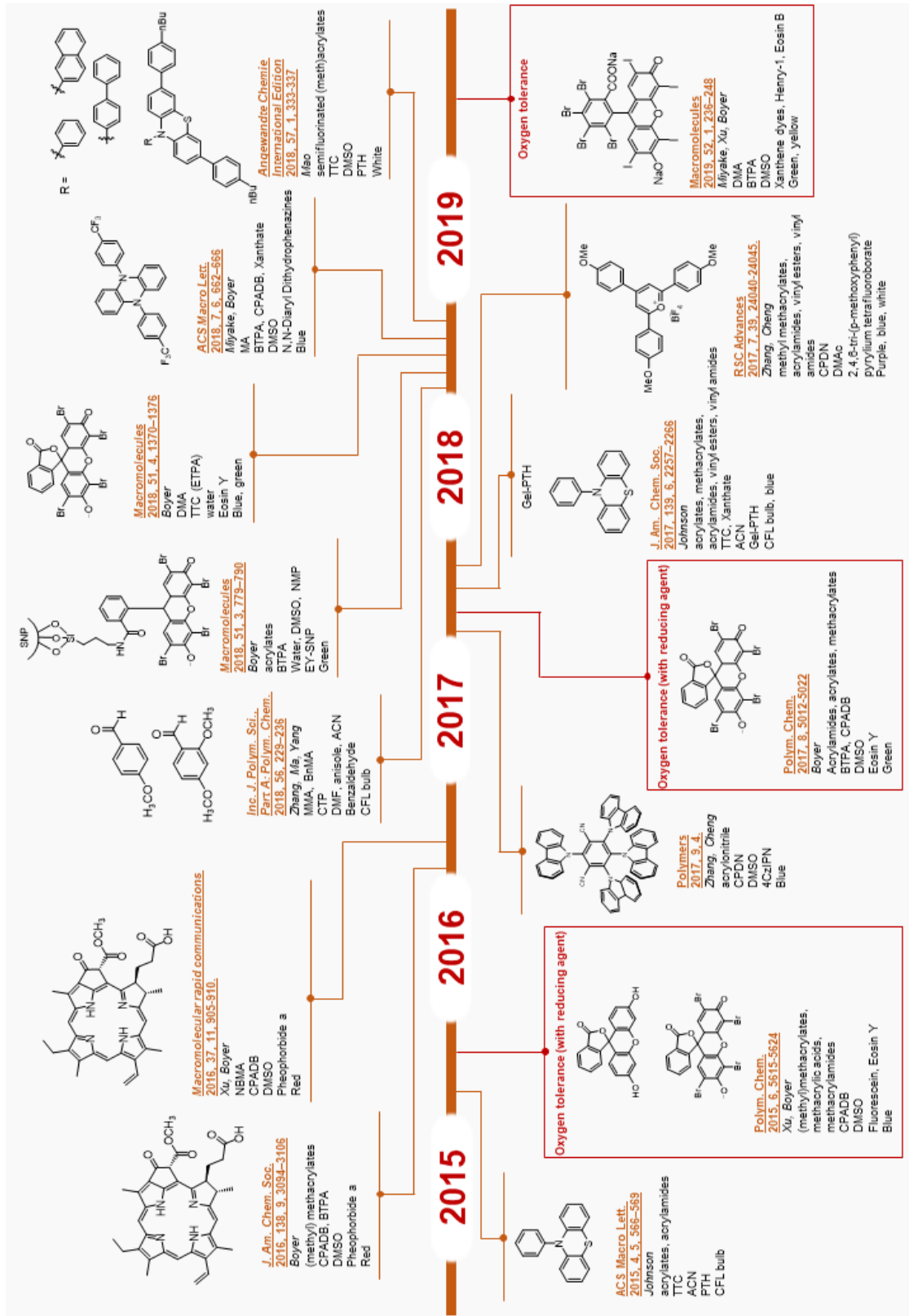


**Figure 5.** Summary of the development of organic photocatalysts for PET-RAFT polymerizations.

### III. Experimental detail

#### 3.1 Materials

All OPCs were synthesized according to the procedures previously reported by our group.<sup>22</sup> Tris(2-phenylpyridinato) iridium(III) (*fac*-Ir(ppy)<sub>3</sub>, TCI), tetrabromofluorescein (eosin Y, TCI), and fluorescein (Aldrich) were purchased commercially, and used without further purifications. Unless otherwise specified, all chemicals and solvents were purchased commercially, and used without further purification. The inhibitor in methyl methacrylate (MMA, Aldrich, contains  $\leq 30$  ppm MEHQ as inhibitor, 99%) was removed by percolating over an aluminum oxide (Aldrich, activated, basic, Brockmann I) column. Pre-prepared stock solutions of the PCs and the chain transfer agents (CTAs) were used for the higher reproducibility.

## 3.2 Instrumentation

### Characterization of Synthesized Polymers

The polymer composition was determined using a  $^1\text{H-NMR}$  spectrometer (Bruker, AVANCE III HD (400 MHz)) with chloroform-d ( $\text{CDCl}_3$ , contains 0.05% v/v tetramethylsilane (TMS), 99.8%) as the solvent.

The molecular weights (MWs) and MW distribution of polymers synthesized were determined by gel permeation chromatography (GPC (Young Lin YL9100 HPLC system)) coupled with a refractive index (RI) detector (Young Lin YL9170 RI detector) and three columns (**Figure 6**). Tetrahydrofuran (THF,

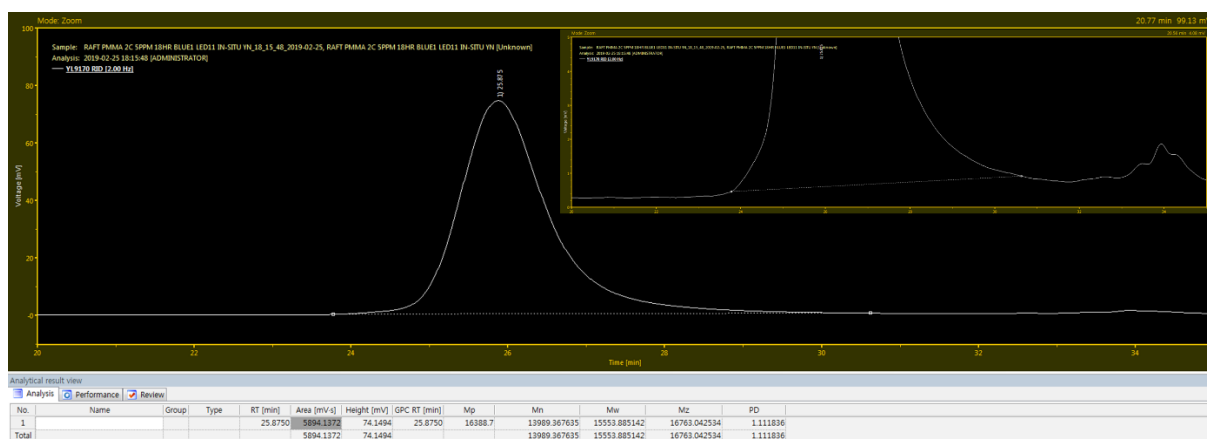


**Figure 6.** Example of calibration of GPC system.

Samchun Chemicals, HPLC, stabilized, > 99.9%) was used as the eluent at 35 °C with a flow rate of 0.8 mL/min. Polymethylmethacrylate (PMMA) standards were used for calibration.

### Photophysical Measurements

Absorbance measurements were done with a Cary 5000 UV-Vis-NIR spectrometer. Room temperature photoluminescence (PL) emission spectra were obtained using a HORIBA Jobin Yvon Fluoromax-4 spectrofluorimeter equipped with a 150 W Xe short arc lamp and Hamamatsu R928P PMT detector; the emission spectra were corrected for the sensitivity of the photomultiplier.

PL quantum yield at r.t. under  $\text{N}_2$  atmosphere was measured relative to the QY of 0.1M  $\text{H}_2\text{SO}_4$  quinine sulfate solution (with absorbance 0.11 at 387 nm) by using following equation:



$$\phi_S = \phi_R \times \frac{\int I_S}{\int I_R} \times \frac{A_R}{A_S} \times \frac{\eta_S^2}{\eta_R^2}$$

Where,  $\phi_S$  is the quantum yield of the samples,  $\phi_R$  is the quantum yield (0.577) of quinine sulfate solution in 0.1M H<sub>2</sub>SO<sub>4</sub>,  $I_S$  and  $I_R$  are the integrated fluorescence area,  $A_S$  and  $A_R$  are the absorbed amount of light (which relates to the absorbance via  $A = 1-10^{-E}$ ) for the sample and reference solutions, respectively.  $\eta_S$  and  $\eta_R$  are the refractive indices of the solvent for the sample and reference solutions.

Low temperature PL measurements were carried out in CH<sub>3</sub>CN solvent. Emission was dispersed in wavelength using an Acton SP2500 spectrometer and detected either by a Princeton Instruments Spec10:400BR CCD camera attached or by a low dark current hybrid photomultiplier (PMA 06, PicoQuant), both attached to the spectrometer. Gated phosphorescence spectra were acquired using a cw 405 nm laser module with TTL modulation input (maximum modulation frequency 20 kHz) and suitable triggering of the CCD. Trigger pulses for the laser and the CCD camera were provided by a Stanford Research Systems DG645 pulse and delay generator with 5 ps resolution. Phosphorescence spectra were acquired with a delay of 30ms after a 2s excitation pulse.

PL decay measurements were carried out by the time-correlated single photon counting (TCSPC) technique. The excitation source was a 405 nm pulsed diode laser (LDH-D-C-405 PicoQuant) of pulse width (FWHM) < 49 ps controlled by a PDL828 driver (PicoQuant) at a repetition rate of 2.5 MHz. A HydraHarp-400 TCSPC event timer with 1 ps time resolution and a Picoquant TimeHarp 260 nano TCSPC electronics with 1 ns resolution were employed to measure decays on short (nanosecond to microsecond) and long (microsecond to second) time scales, respectively. The decay time fitting procedure was carried out with the measured IRF by using the Fluofit software (PicoQuant). Smallest residual values were obtained in the fitting procedure. The phosphorescence decay measurements were carried out by using gated 405 nm cw excitation.

## Transient absorption spectroscopy

### ■ Calculation of intersystem crossing rates and yields

Scheme 1 summarizes the photophysical processes that have to be considered for the actual system. It leads to the following system of ordinary differential equations (ODE) that define the dynamics of the concentration of excited singlet and triplet states (S and T, respectively):

$$\left\{ \begin{array}{l} \frac{dS}{dt} = -(k_F + k_{nr} + k_{isc}) \cdot S + k_{risc} \cdot T \\ \frac{dT}{dt} = -(k_{T0} + k_{risc}) \cdot T + k_{isc} \cdot S \end{array} \right\} \quad (S1)$$

In eq. S1,  $k_F$  and  $k_{nr}$  are rate constants for the radiative (by fluorescence) and non-radiative singlet deactivation, respectively,  $k_{isc}$  and  $k_{risc}$  are the forward and backward (return) intersystem crossing rate constants, and the rate constant  $k_{T0}$  summarizes phosphorescence and radiation-less deactivation into the electronic ground state  $S_0$ .

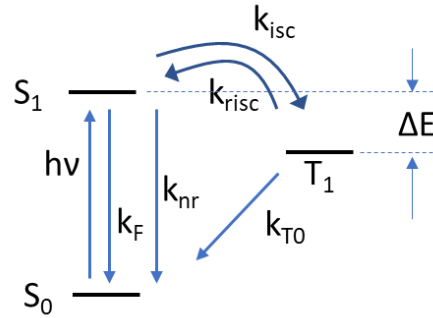


**Figure 7.** Photophysical model to describe the dynamics and yields. States are given as capital letters; rate constants use the symbol “k”. The energy difference between the lowest excited singlet and triplet states is given as  $\Delta E$ .

#### ■ By Fluorescence Transient

Time-resolved photoluminescence can be used as a probe for the time-resolved concentration of  $S(t)$ :

$$PL(t) = \left(\frac{dS}{dt}\right)_{PL} = r \cdot k_r \cdot S(t) \quad (S2)$$

ODE systems of the form of eq. S1 lead to biexponential kinetics for both  $S(t)$  and  $T(t)$ . Therefore, PL decay traces will not suffice to quantify the 5 rate constants of scheme 1. We used the following strategy to obtain reliable rate constants:

The radiative rate constant  $k_r$  was calculated using the formula of Strickler and Berg, which in simplified form reads  $k_{F,SB} = 4.34 \cdot 10^7 [s^{-1}eV^{-2}] \frac{E_{F,vert}^3}{E_{A,vert}} f$ . Starting from the TD-DFT calculated oscillator strength of  $f = 0.079$  and a vertical absorption and emission energies  $E_{A,vert} = 2.43$  eV and  $E_{F,vert} \approx 1.9$  eV, respectively for the lowest energetic CT transition, we obtain  $k_r = 1 \times 10^7$  s<sup>-1</sup>. By spectral modeling of the early transient absorption spectra, which are entirely dominated by the  $S_1$  state, we find that the oscillator strength for stimulated emission is approximately equal to that of the corresponding absorption band, for which we find  $f = 0.082$ , very close to the calculated value.

The PL quantum yield was measured as  $\phi_{PL} = 0.18$  in  $CH_3CN$ . Assuming  $k_{T0} \equiv 0$  (we will verify this assumption below), all photoexcited states must decay through the singlet channel, for which the PL quantum yield is defined as  $\phi_{PL} = \frac{k_F}{(k_F + k_{nr})}$ . From this relation, we get  $k_{nr} = 4.6 \times 10^7$  s<sup>-1</sup>.

As noted above, the decay of  $S(t)$  follows biexponential kinetics, producing a fast and a slow decay time ( $\tau_1$  and  $\tau_2$ , respectively). The fast process is caused by equilibration kinetics:

$$\frac{1}{\tau_1} = k_F + k_{nr} + k_{isc} \quad (S3)$$

We found  $\tau_1 = 3.3$  ns for both DMSO and  $\text{CH}_3\text{CN}$  so that  $k_{isc} = 2.5 \times 10^8 \text{ s}^{-1}$ . Therefore, the total yield of triplet states  $\phi_T = \frac{k_{isc}}{(k_F + k_{nr} + k_{isc})} = 0.82$ , signifying the upper limit to the overall photochemical polymerization yield when this material is used as a photocatalyst.

For the slower time constant of the PL traces we found  $\tau_2 = 100$   $\mu\text{s}$ . This is significative of the lifetime of the triplet state, detected by thermally activated delayed fluorescence (TADF, ref the Portuguese paper)<sup>37</sup> controlled by the thermodynamic equilibrium constant.

$$K = \frac{k_{risc}}{k_{isc}} = \exp\left(\frac{-\Delta E}{k_B T}\right) \quad (S4)$$

In eq. S4,  $\Delta E$  is the energy difference between the lowest excited singlet and triplet state,  $k_B = 8.617 \times 10^{-5} \text{ eV/K}$  is Boltzmann's constant and  $T = 293 \text{ K}$  is the temperature. By numerically solving ODE system S1 (setting  $k_{T0} = 0$ ) and fitting the resulting singlet dynamics  $S(t)$  with a biexponential function, we can reproduce the experimental values of  $\tau_1 = 3.3$  ns and  $\tau_2 = 100$   $\mu\text{s}$  if we assume  $\Delta E = 0.214$  eV and calculate  $k_{risc}$  using eq. S4. The experimentally obtained value is  $\Delta E = 0.2$  eV, obtained by comparing the onsets of the photoluminescence and phosphorescence spectra; using this value to solve ODE system S1, we obtain a slow decay time  $\tau_2 = 40$   $\mu\text{s}$ , thus underestimating the experimental triplet lifetime. For any value  $k_{T0} > 0$  we would add another decay path for triplet states, causing an even greater underestimation of the experimentally measured lifetimes. Estimating the error in the experimental determination of  $\Delta E$  to be 20 meV, we can therefore confirm the assumption we applied in the beginning of this chapter, that all triplet states decay exclusively through the TADF pathway and direct triplet recombination to the ground state is insignificant at room temperature.

#### ■ By Transient Absorption

Similar results are obtained by an independent study of transient absorption (TA) dynamics in the same sample. The differential absorption is defined as

$$\Delta A = A_{pu} - A_0, \quad (S5)$$

where  $A = -\ln T$  is the natural absorbance (base e) with the transmission  $T$ , and the suffixes “0” and “pu” refer to the unperturbed sample (all molecules in electronic ground state) and the sample perturbed by a pump pulse, respectively. In the latter case, some of the molecules are in an excited state. All states,

whether ground or excited states, have characteristic resonance energies, leading to characteristic absorption spectra that can be interrogated by a broadband (white) probe pulse.

The fact that the probe pulse is broadband allows us to measure  $A$  at various probe energies  $E_{pr}$ , thus obtaining a TA spectrum  $\Delta A(E_{pr})$ ; the fact that it is a pulse allows us to measure time-resolved TA spectra  $\Delta A(E_{pr}, t)$  where  $t$  is the pump-probe delay time. According to the Beer-Lambert Law,

$$A(E_{pr}) = \sum_i (\sigma_i(E_{pr}) \cdot s_i) \quad (S6)$$

every electronic state  $i \in \{1, \dots, n_{st}\}$  contributes additively to the overall natural absorbance due to its characteristic spectrum of absorption cross-sections  $\sigma_i(E_{pr})$  times the area density  $s = c \cdot d$ , where  $c$  is the concentration and  $d$  is the sample thickness. We consider a total of  $n_{st}$  contributing states. Inserting S6 into S5 yields

$$\Delta A = \sum_i (\sigma_i(E_{pr}) \cdot s_{i,pu}(t)) - \sum_i (\sigma_i(E_{pr}) \cdot s_{i,0}(t)) = \sum_i (\sigma_i(E_{pr}) \cdot \Delta s_i(t)) \quad (S7)$$

In the last term, we introduced  $\Delta s_i(t) = s_{i,pu}(t) - s_{i,0}(t)$  as the pump-induced change of concentration remaining at time  $t$  after the pump. Since the continuous functions  $\sigma_i(E_{pr})$  and  $\Delta s_i(t)$ , and thus  $\Delta A$ , are experimentally probed only at  $n_E$  probe energy points and at  $n_t$  time points, it is convenient to restate S7 in matrix notation. Introducing two-dimensional matrices  $\boldsymbol{\sigma}$  ( $n_{st}$  column vectors of absorption cross-sections  $\sigma_i(E_{pr})$ ) and  $\mathbf{s}$  ( $n_{st}$  row vectors of concentration-time dependences  $\Delta s_i(t)$ ), we obtain

$$\mathbf{A} = \boldsymbol{\sigma} \times \mathbf{s}, \quad (S8)$$

where  $\mathbf{A}$  is now an  $(n_E \times n_t)$  matrix of differential absorptions  $\Delta A(E_{pr}, t)$  measured at  $n_E$  probe energies and  $n_t$  time points. We can isolate  $\mathbf{s}$  by left-multiplying the inverse matrix  $\boldsymbol{\sigma}^{-1}$ :

$$\mathbf{s} = \boldsymbol{\sigma}^{-1} \times \mathbf{A} \quad (S9)$$

Eq. S9 shows that we can obtain the complete dynamics of all photoexcited states (i.e., the solution of ODE S1) if we know the set of characteristic spectra  $\boldsymbol{\sigma}$  for all contributing states, by multiplying the matrix inverse  $\boldsymbol{\sigma}^{-1}$  with the experimental differential absorption spectrum  $\mathbf{A}$ . However, since generally  $n_E \neq n_{st}$ ,  $\boldsymbol{\sigma}$  is not square, we cannot rigorously calculate its inverse. Here, we use the property of a *truncated singular value decomposition (t-SVD)* that it is always optimal in the least-squares sense, the  $n_s$  strongest singular values of an SVD,

$$\mathbf{A}_{exp} = \mathbf{U} \times \mathbf{s} \times \mathbf{V} = \mathbf{U}_s \times \mathbf{s}_s \times \mathbf{V}_s + \mathbf{U}_n \times \mathbf{s}_n \times \mathbf{V}_n = \mathbf{U}_s \times \mathbf{s}_s \times \mathbf{V}_s + \mathbf{N}; s \in \{1..n_{st}\}, \quad (S10)$$

are automatically selected such as to minimize the square  $\mathbf{N}^2$  of the residuals (noise)  $\mathbf{N}$ . in eq. S10, suffixes  $s$  and  $n$  refer to “signal-related” and “noise-related”, respectively. This means that performing

a t-SVD on an experimental differential absorption matrix  $\mathbf{A}_{\text{exp}}$  will yield a matrix of  $n_s$  column vectors  $\mathbf{U}_s$ , and a matrix of  $n_s$  row vectors  $\mathbf{T}_s = \mathbf{s}_s \times \mathbf{V}_s$ , that together represent a *bias-free global fit* to  $\mathbf{A}_{\text{exp}}$ .

The matrices  $\mathbf{U}_s$  and  $\mathbf{T}_s$  are closely related to our desired matrices  $\boldsymbol{\sigma}$  and  $\mathbf{s}$  in eq. S8, respectively, as we can see by inserting the identity  $\mathbf{R} \times \mathbf{R}^{-1}$  into eq. S10:

$$\mathbf{A}_{\text{exp}} = \mathbf{U}_s \times \mathbf{R} \times \mathbf{R}^{-1} \times \mathbf{T}_s + \mathbf{N} \quad (\text{S11})$$

We find that S11 is identical with S8 if

$$\mathbf{A} = \mathbf{A}_{\text{exp}} - \mathbf{N}; \quad \boldsymbol{\sigma} = \mathbf{U}_s \times \mathbf{R}; \quad \mathbf{s} = \mathbf{R}^{-1} \times \mathbf{T}_s \quad (\text{S12})$$

The matrix  $\mathbf{R}$  is called the *rotation matrix*; as shown by eq. S12, its matrix elements  $R_{ij}$  are the spectral weights of the  $i$ -th SVD spectrum  $\mathbf{U}_{s,i}$  in the characteristic spectrum of state  $j$ ,  $\sigma_j$ .  $\mathbf{R}$  can therefore also be called the *spectral weights matrix*.

In our experiment, we expect 3 states to contribute to  $\mathbf{A}$  in eq. S8: the singlet ground state  $S_0$ , the first excited singlet state  $S_1$  and the lowest energetic triplet state  $T_1$ . However, due to the energy conservation rule

$$c(T_1) + c(S_1) + c(S_0) = c_{\text{tot}}, \quad (\text{S13})$$

where  $c_{\text{tot}}$  is the total concentration of molecules that can be either in the ground state or in one of the excited states, we will obtain only two linearly independent SVD spectra in eq. S10. Due to the linear dependence of one of the concentrations on the other ones, in our kinetic scheme 1 the number of signal-related SVD states is therefore  $n_s = n_{st} - 1 = 2$ .

Due to this linear dependence, we will define the characteristic spectra for  $S_1$  and  $T_1$  by incorporating the associated reduction of ground state absorption (“ground state bleach”):

$$\sigma'_{S_1}(E_{pr}) = \sigma_{S_1}(E_{pr}) - \sigma_{S_0}(E_{pr}); \quad \sigma'_{T_1}(E_{pr}) = \sigma_{T_1}(E_{pr}) - \sigma_{S_0}(E_{pr}) \quad (\text{S14})$$

Eq. S14 can be validated by introducing it into S7; one finds that the energy conservation rule eq. S13 is automatically respected.

Now that the mathematical formalism is clear, we need to find  $\sigma'_{S_1}(E_{pr})$  and  $\sigma'_{T_1}(E_{pr})$  to solve eq. S12 to obtain the complete photoexcitation dynamics in  $\mathbf{s}$ . Looking at Scheme 1, we can take advantage of the fact that due to the spin selection rule, the pump pulse exclusively generates  $S_1$  states. Hence, we can use eq. S7 to obtain the characteristic spectrum of  $S_1$  states if we measure  $\Delta A$  at short enough times so that triplet states have not yet been formed. In this case eq. S7 simplifies to:

$$\Delta A(t \rightarrow 0) = \sigma_{S_1}(E_{pr}) \cdot \Delta s_{S_1}(t) + \sigma_{S_0}(E_{pr}) \cdot \Delta s_{S_0}(t) = \sigma'_{S_1}(E_{pr}) \cdot \Delta s_{S_1}(t), \quad (\text{S15})$$

because in this case the energy conservation law simplifies to  $\Delta c(S_1) = -\Delta c(S_0)$ . As long as no decay to the ground state has yet occurred, the area density of excited states equals the area density (flux) of absorbed photons  $J_{ph,abs}$ . Therefore, we get:

$$\sigma'_{S_1}(E_{pr}) = \frac{\Delta A(t \rightarrow 0)}{J_{ph,abs}}, \quad (S16)$$

showing the usefulness of eq. 14. In practice, we took the  $\Delta A$  spectrum at  $t=20$  ps to accommodate internal vibrational relaxation and solvent relaxation after impulsive excitation.

The characteristic spectrum of  $T_1$  states is obtained in a similar way. According to Scheme 1, for times much longer than the equilibration time  $\tau_1$ , there will be an equilibrium between  $S_1$  and  $T_1$  states that will be far on the side of  $T_1$ . As the experimentally detected energy difference is  $\Delta E = 0.2$  eV, the equilibrium ratio  $c(S_1)/c(T_1)$  will be less than 1/1000 allowing us to neglect singlet states in eq. S7 in this case:

$$\Delta A(t \gg \tau_1) = \sigma'_{T_1}(E_{pr}) \cdot \Delta s_{T_1}(t). \quad (S17)$$

The problem here is that we do not know a priori the remaining triplet concentration at time  $t$ . Again, the definition of  $\sigma'_{T_1}(E_{pr})$  in eq. S14 turns out very helpful: As we know the absolute cross-sections of the ground state  $\sigma_{S_0}(E_{pr})$ , we can find both  $\Delta s_{T_1}(t)$  and  $\sigma'_{T_1}(E_{pr})$  at the same time by a curve optimization scheme, varying the spectral shape  $\sigma_{T_1}(E_{pr})$  by introducing one or more positive Gaussians, taking advantage of the fact that triplet states do not show stimulated emission (formally negative TA).

Finally, having obtained the absolute time-resolved concentrations of  $S_1$  and  $T_1$  states, we can reproduce their dynamics by numerically solving ODE system S1 and varying the rate constants in a non-linear optimization algorithm, thus obtaining all rate constants except  $k_r$  and  $k_{nr}$ , which cannot be distinguished and are summarized into  $k_m = k_r + k_{nr}$ .

## Electrochemical Measurements

Cyclic voltammetry (CV) experiments were carried out with a VersaSTAT3-200 (Princeton Applied Research) using an onecompartment electrolysis cell consisting of a glassy carbon working electrode, a platinum wire counter electrode, and a quasi  $Ag^+/Ag$  (sat. KCl) reference electrode bought from AT FRONTIER (Part No. R303). Specifically, the electrode is a silver wire that is coated with a thin layer of silver chloride and an insulated lead wire connects the silver wire with measuring instrument. The electrode also consists of a porous plug on the one end which will allow contact between the field environment with the silver chloride electrolyte. Saturated potassium chloride is added inside the body

of the electrode to stabilize the silver chloride concentration and in this condition the electrode's reference potential is known to be +0.197 V at 25 °C.

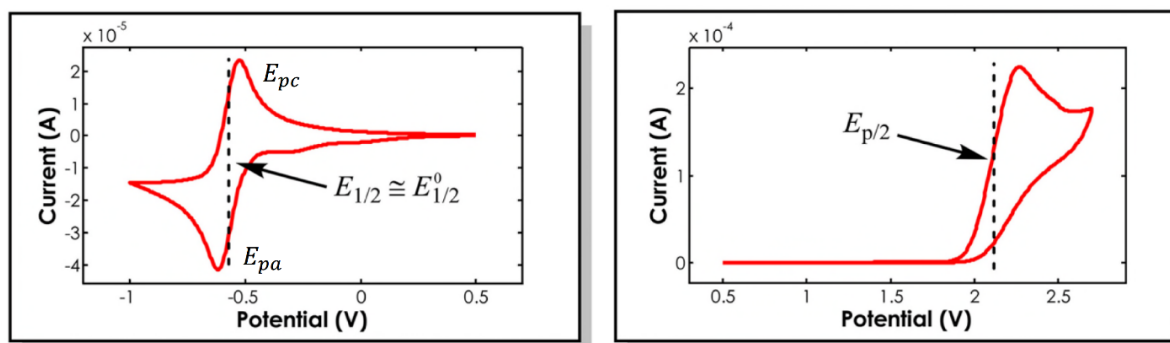


**Figure 8.** Representative CV demonstrating a reversible (left) and an irreversible (right) redox behavior.<sup>38</sup>

For our OPCs and *fac*-Ir(ppy)<sub>3</sub>, the measurements were done in 2 mM CH<sub>3</sub>CN (Alfa aesar, anhydrous, 99.8+%) solution with 0.1 M tetrabutylammonium hexafluorophosphate (n-Bu<sub>4</sub>NPF<sub>6</sub>, Aldrich, Electrochemical grade) as supporting electrolyte at a scan rate of 100 mV/s. For fluorescein and eosin Y, the measurements were done in 2 mM CH<sub>3</sub>CN:H<sub>2</sub>O (1:1 v/v) solution with 0.1 M n-Bu<sub>4</sub>NPF<sub>6</sub> as supporting electrolyte at a scan rate of 100 mV/s. The redox potential was calibrated after each experiment against the ferrocenium/ferrocene couple (Fc<sup>+</sup>/Fc), which allowed conversion of all potentials to the aqueous saturated calomel electrode (SCE) scale by using  $E_0(\text{Fc}^+/\text{Fc}) = 0.42 \text{ V vs. SCE in CH}_3\text{CN}$ . The working solution was degassed with N<sub>2</sub> for 15 min (30 min for fluorescein and eosin Y) before measurement and then kept under a positive N<sub>2</sub> pressure during the measurement.

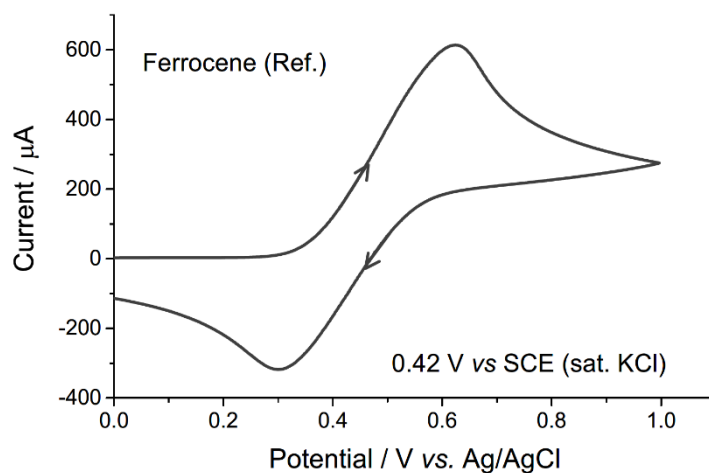


**Figure 9.** CV curve of ferrocene recorded in our lab.

For the compounds showing a reversible redox behavior, the standard reduction potentials of PC<sup>+</sup> ( $E_{ox}^0$ ) and PC ( $E_{red}^0$ ) in the ground state were obtained from CV as the half sum of anodic ( $E_{pa}$ ) and cathodic ( $E_{pc}$ ) peak potentials such as following:

$$E_{ox}^o \approx E_{1/2}^o = \frac{(E_{pa} + E_{pc})}{2}$$

$$E_{red}^o \approx E_{1/2}^o = \frac{(E_{pa} + E_{pc})}{2}$$

For the compounds exhibiting an irreversible redox behavior, the standard reduction potentials of PC<sup>+</sup> and PC in the ground state were taken from half-peak potentials ( $E_{1/2}^0$ ), which correspond to the potential at half the maximum current in the CV as a way to estimate  $E_{1/2}^0$ . However, in such compounds having an irreversible redox behavior, it should be noted that the values are not truly reflective of  $E_{1/2}^0$  due to the issues explained in the previous literature.<sup>39</sup>

Basically, we conducted all experiments with a standard condition to maintain internal consistency; this includes that all measurements were performed with the same scan rate (100 mV/s) and the same solution of electrolytes. In addition, following the suggestion by Addison,<sup>40</sup> we converted measured potential values from silver–silver chloride into saturated calomel electrode (SCE) and the redox potentials of the compounds including OPCs and substrates are reported in volts against the SCE.

### Quantum-chemical Calculations

Geometrical, electronic and optical properties of the 4DP-IPN catalyst and of initiators CPADB, CDTPA were carried out by (time-dependent) density functional theory, (TD)DFT, using the Gaussian09 program package, using the B3LYP functional with the 6-311+G\* basis set.<sup>41-43</sup> For this, the geometries were optimized in vacuum, all single point calculations were carried out in dimethylformamid (DMF) solution, using the polarizable continuum model (PCM).



### 3.3 Syntheses of 4DP-IPN

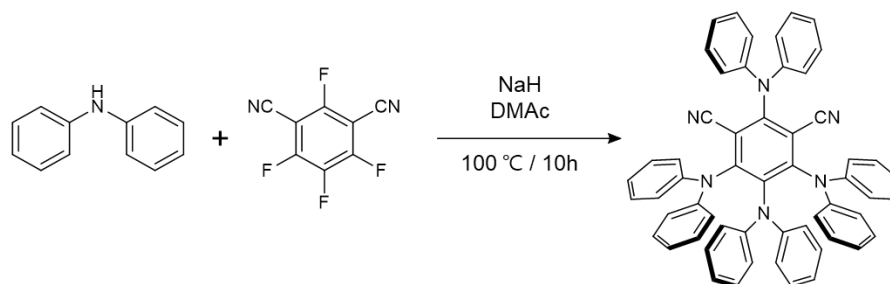


**Figure 10.** Syntheses scheme of 4DP-IPN.

**2,4,5,6-tetrakis(diphenylamino)benzene-1,3-dinitrile (4DP-IPN):** A solution of NaH (60% in oil, 0.477 g, 11.94 mmol) and diphenylamine (1.48 g, 8.75 mmol) in anhydrous dimethyl acetamide DMAc (5 mL) was stirred for 30 min in an ice bath under argon atmosphere. After 30 min, tetrafluoroisophthalonitrile (0.4 g, 1.99 mmol) dissolved in DMAc (5 mL) was slowly added to the reaction mixture and stirred further for 10 hours at 100 °C. Afterwards, distilled water (2 mL) was poured into the reaction mixture to quench the leftover NaH and methanol was added to precipitate the crude product, which was further purified by column chromatography on silica gel ( $\text{CH}_2\text{Cl}_2$ :hexane, 2:3 v/v) to give pure product (1.32 g, 83.4% yield).  $^1\text{H-NMR}$  (400 MHz,  $\text{CDCl}_3$ ):  $\delta$  7.31-7.27 (t, 4H), 7.12-7.08 (t, 12H), 7.07-7.03 (t, 2H), 6.95-6.88 (m, 8H), 6.73 (d, 10H), 6.57 (d, 4H).  $^{13}\text{C-NMR}$  ( $\text{CDCl}_3$ , 100 MHz, ppm):  $\delta$  154.15, 151.68, 145.47, 144.61, 143.06, 140.24, 129.34, 128.56, 127.52, 124.11, 123.87, 122.91, 122.57, 121.02, 113.11, 112.97. HRMS  $m/z$  (ESI $^+$ ) Calculated for  $\text{C}_{56}\text{H}_{40}\text{N}_6$  ( $\text{M}^++1$ ) 797.33, found: 797.33. analysis (calcd., found for  $\text{C}_{56}\text{H}_{40}\text{N}_6$ ): C (84.40, 82.51), H (5.06, 4.94), N (10.55, 9.97). For  $^1\text{H-NMR}$  and  $^{13}\text{C-NMR}$  are in **Figure 48, 49**.

### 3.4 Experimental procedure

#### Procedure for negative control experiment in the presence of argon and air

A procedure for the standard reaction conditions [MMA]:[CTA]:[PC] = [200]:[1]:[0] under argon was carried out as follow. A 20 mL glass vial equipped with a stirring bar was charged with MMA (1.0 mL, 9.29 mmol) and CPADB (0.046 mmol), and anhydrous DMSO (1 mL; Aldrich, anhydrous, 99.9%) as the solvent, inside a glove box, for the polymerization. Afterwards, the vial was capped with a rubber septum and sealed with parafilm, and bubbled with argon for 30 min outside the glove box. Subsequently, the polymerization was carried out under a 3 W 455 nm LED (ca. 2.5 mW/cm<sup>2</sup>) irradiation at room temperature. After 18 h, a 0.1 mL aliquot of the reaction mixture was removed via syringe and dissolved in a vial containing CDCl<sub>3</sub>. Without storing, the aliquot was then immediately analyzed using <sup>1</sup>H-NMR for conversion. The sample used for <sup>1</sup>H-NMR analysis was then dried under a reduced pressure and re-dissolved in THF for the number-average molecular weight (M<sub>n</sub>) and polydispersity analyses using GPC.

In the presence of air, a 4 mL glass vial equipped with a stirring bar was charged with MMA (1.5 mL, 13.9 mmol), CPADB (0.070 mmol) and DMSO (1.5 mL) as the solvent. After, the vial was capped with a rubber septum and sealed with parafilm, and bubbled with air (DEOKYANG, O<sub>2</sub> 21 mol%, H<sub>2</sub>O 2 x 10<sup>-6</sup> mol%) for 30 min outside the glove box. After then, the process is the same as above.

#### General procedure for PET-RAFT polymerizations of MMA in the presence of argon and air

A typical PET-RAFT procedure for the standard reaction conditions [MMA]:[CTA]:[OPC] = [200]:[1]:[0.001] and [MMA]:[CTA]:[Ir(ppy)<sub>3</sub>] = [200]:[1]:[0.0002] under argon was carried out as follow. A 20 mL glass vial equipped with a stirring bar was charged with MMA (1.0 mL, 9.29 mmol), CPADB (0.046 mmol), OPC (4.65 x 10<sup>-5</sup> mmol) and DMSO (1.0 mL) as the solvent, inside a glove box, for reaction condition [MMA]:[CTA]:[OPC] = [200]:[1]:[0.001]. For reaction condition [MMA]:[CTA]:[Ir(ppy)<sub>3</sub>] = [200]:[1]:[0.0002]; Ir(ppy)<sub>3</sub> (9.29 x 10<sup>-6</sup> mmol) in DMSO (1.0 mL) was used. After, the vial was capped with a rubber septum and sealed with parafilm, and bubbled with argon for 30 min outside the glove box. Subsequently, the polymerization was carried out under a 3 W 455 nm LED (ca. 2.5 mW/cm<sup>2</sup>) irradiation at room temperature. After 18 h, a 0.1 mL aliquot of the reaction mixture was removed via a syringe and dissolved in a vial containing CDCl<sub>3</sub>. Without storing, the aliquot was then immediately analyzed by <sup>1</sup>H-NMR for conversion. The sample used for <sup>1</sup>H-NMR analysis was then dried under a reduced pressure and re-dissolved in THF for the M<sub>n</sub> and polydispersity analyses using GPC.

For experiments under green LED, the polymerization was carried out for 6 h under a 3 W 515 nm

LED (ca. 0.5 mW/cm<sup>2</sup>) irradiation at room temperature. Other process is the same as above.

In the presence of air, a 4 mL glass vial equipped with a stirring bar was charged with MMA (1.5 mL, 13.9 mmol), CPADB (0.070 mmol), OPC (6.97 x 10<sup>-5</sup> mmol) and DMSO (1.5 mL) as a solvent, inside a glove box, for reaction condition [MMA]:[CTA]:[OPC] = [200]:[1]:[0.001]. For a reaction condition, [MMA]:[CTA]:[Ir(ppy)<sub>3</sub>] = [200]:[1]:[0.0002]: Ir(ppy)<sub>3</sub> (1.39 x 10<sup>-5</sup> mmol) in DMSO (1.5 mL) was used. After, the vial was capped with a rubber septum and sealed with parafilm, and bubbled with air for 30 min outside the glove box. After then, the process is the same as above.

### Experimental procedure for kinetic studies in the presence of argon and air

A typical PET-RAFT procedure for the standard reaction conditions [MMA]:[CTA]:[4DP-IPN] = [200]:[1]:[0.001] and [MMA]:[CTA]:[Ir(ppy)<sub>3</sub>] = [200]:[1]:[0.0002] under argon were carried out as follow. A 20 mL glass vial equipped with a stirring bar was charged with MMA (1.5 mL, 13.9 mmol), CPADB (0.070 mmol), 4DP-IPN (6.97 x 10<sup>-5</sup> mmol) and DMSO (1.5 mL) as solvent, inside a glove box, for reaction condition [MMA]:[CTA]:[OPC] = [200]:[1]:[0.001]. For reaction condition [MMA]:[CPADB]:[Ir(ppy)<sub>3</sub>] = [200]:[1]:[0.0002]: Ir(ppy)<sub>3</sub> (1.39 x 10<sup>-5</sup> mmol) in DMSO (1.5 mL) was used. After, the vial was capped with a rubber septum and sealed with parafilm, and bubbled with argon for 30 min outside the glove box. Subsequently, the polymerization was carried out under a 3 W 455 nm LED (ca. 2.5 mW/cm<sup>2</sup>) irradiation at room temperature. A 0.1 mL aliquot of the reaction mixture was taken via a syringe at predetermined interval times and dissolved in a vial containing CDCl<sub>3</sub>. Without storing, each aliquot was then immediately analyzed using <sup>1</sup>H-NMR for conversion. The samples used for <sup>1</sup>H-NMR analyses were then dried under a reduced pressure and re-dissolved in THF for M<sub>n</sub> and polydispersity analyses using GPC.

In the presence of air, a 4 mL glass vial equipped with a stirring bar was charged with MMA (1.5 mL, 13.9 mmol), CPADB (0.070 mmol), 4DP-IPN (6.97 x 10<sup>-5</sup> mmol) and DMSO (1.5 mL) as solvent, inside a glove box, for reaction condition [MMA]:[CTA]:[OPC] = [200]:[1]:[0.001]. For reaction condition [MMA]:[CTA]:[Ir(ppy)<sub>3</sub>] = [200]:[1]:[0.0002]: Ir(ppy)<sub>3</sub> (1.39 x 10<sup>-5</sup> mmol) in DMSO (1.5 mL) was used. After, the vial was capped with a rubber septum and sealed with parafilm, and bubbled with air for 30 min outside the glove box. After then, the process is the same as above. However, because of the weakness of the small rubber septa for 4 mL vials, kinetic study in the presence of air was done by dividing time intervals into three parts to prevent further addition of oxygen from atmosphere; 0 min ~ 1 h, 2 h ~ 6 h, 9 h ~ 18 h. The experiments were done under the same LED set-up condition for the same catalyst.

### Experimental procedure for temporal control in the presence of argon

A typical PET-RAFT procedure for the standard reaction conditions [MMA]:[CPADB]:[4DP-IPN] = [200]:[1]:[0.001] and [MMA]:[CPADB]:[Ir(ppy)<sub>3</sub>] = [200]:[1]:[0.0002] under argon were carried out as follow. A 20 mL glass vial equipped with a stirring bar was charged with MMA (1.5 mL, 13.9 mmol), CPADB (0.070 mmol), 4DP-IPN ( $6.97 \times 10^{-5}$  mmol) and DMSO (1.5 mL) as solvent, inside a glove box, for reaction condition [MMA]:[CTA]:[OPC] = [200]:[1]:[0.001]. For reaction condition [MMA]:[CPADB]:[Ir(ppy)<sub>3</sub>] = [200]:[1]:[0.0002]: Ir(ppy)<sub>3</sub> ( $1.39 \times 10^{-5}$  mmol) in DMSO (1.5 mL) was used. After, the vial was capped with a rubber septum and sealed with parafilm, and bubbled with argon for 30 min outside the glove box. Subsequently, the polymerization was carried out by switching the irradiation source on and off for predetermined interval times (under a 3 W 455 nm LED (ca. 2.5 mW/cm<sup>2</sup>) irradiation at room temperature). The total reaction time including both “ON” and “OFF” steps was 22 h. A 0.1 mL aliquot of the reaction mixture was taken via a syringe at each interval and dissolved in a vial containing CDCl<sub>3</sub>. Without storing, the aliquot was then immediately analyzed using <sup>1</sup>H-NMR for determining the conversion.

### Experimental procedure for chain extension in the presence of argon and air

A typical PET-RAFT procedure for the standard reaction conditions [MMA]:[CPADB or Macroinitiator]:[4DP-IPN] = [200]:[1]:[0.001] under argon was carried out as follow. A 20 mL glass vial equipped with a stirring bar was charged with MMA (1.0 mL, 9.29 mmol), CPADB (0.046 mmol), 4DP-IPN ( $4.65 \times 10^{-5}$  mmol) and DMSO (1.0 mL) as solvent, inside a glove box. After, the vial was capped with a rubber septum and sealed with parafilm, and bubbled with argon for 30 min outside the glove box. Subsequently, the polymerization was carried out under a 3W 455 nm LED (ca. 2.5 mW/cm<sup>2</sup>) irradiation at room temperature. For the first chain, the reaction was carried out for 12 h. To isolate the first chain, the reaction mixture was first diluted with 3 mL of THF and dissolved completely, then poured into beaker containing methanol (75 mL) which caused the polymer to precipitate. Subsequent stirring for 30 min followed by vacuum filtration resulted in dried polymer which can be used as a macroinitiator ( $M_n = 12,500$  Da,  $D = 1.07$ ). Again, a 20 mL glass vial equipped with a stirring bar was charged with MMA (0.2 mL, 1.86 mmol), macroinitiator (0.116 g,  $9.29 \times 10^{-3}$  mmol), 4DP-IPN ( $9.29 \times 10^{-6}$  mmol) and DMSO (1.2 mL) as solvent. After, the vial was capped with a rubber septum and sealed with parafilm, and bubbled with argon for 30 min outside the glove box. Subsequently, the polymerization was carried out under a 3 W 455 nm LED (ca. 2.5 mW/cm<sup>2</sup>) irradiation at room temperature. For the second chain, the reaction was carried out for 8 h. A 0.1 mL aliquot of the reaction mixture was removed via a syringe and dissolved in a vial containing CDCl<sub>3</sub>. Without storing, the aliquot was then immediately analyzed using <sup>1</sup>H-NMR for determining the conversion. The sample used

for  $^1\text{H-NMR}$  analysis was then dried under reduced pressure and re-dissolved in THF for  $M_n$  and polydispersity analysis using GPC.

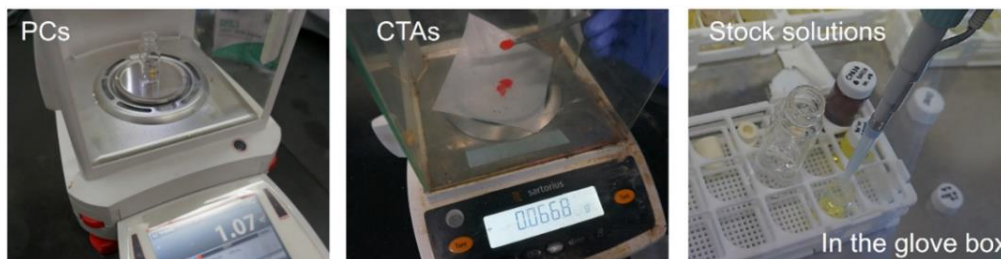
In the presence of air, a 4 mL glass vial equipped with a stirring bar was charged with MMA (1.5 mL, 13.9 mmol), CDTPA (0.070 mmol), 4DP-IPN ( $6.97 \times 10^{-5}$  mmol) and DMSO (1.5 mL) as solvent, inside a glove box. After, the vial was capped with a rubber septum and sealed with parafilm, and bubbled with air for 30 min outside the glove box. Subsequently, the polymerization was carried out under a 3 W 515 nm LED (ca.  $0.5 \text{ mW/cm}^2$ ) irradiation at room temperature. For the first chain, the reaction was carried out for 5 h. To isolate the first chain, the reaction mixture was first diluted with 4.5 mL of THF and dissolved completely, then poured into beaker containing methanol (120 mL) which caused the polymer to precipitate. Subsequent stirring for 30 min followed by vacuum filtration resulted in dried polymer which can be used as a macroinitiator ( $M_n = 15,800$ ,  $D = 1.15$ ). Again, a 20 mL glass vial equipped with a stirring bar was charged with MMA (0.378 mL, 3.51 mmol), macroinitiator (0.278 g, 0.018 mmol), 4DP-IPN ( $1.76 \times 10^{-5}$  mmol) and DMSO (2.482 mL) as solvent. After, the vial was capped with a rubber septum and sealed with parafilm, and bubbled with air for 30 min outside the glove box. Subsequently, the polymerization was carried out under a 3 W 515 nm LED (ca.  $0.5 \text{ mW/cm}^2$ ) irradiation at room temperature. For the second chain, the reaction was carried out for 3 h. A 0.1 mL aliquot of the reaction mixture was removed via a syringe and dissolved in a vial containing  $\text{CDCl}_3$ . Without storing, the aliquot was then immediately analyzed using  $^1\text{H-NMR}$  for conversion. The sample used for  $^1\text{H-NMR}$  analysis was then dried under a reduced pressure and re-dissolved in THF for  $M_n$  and polydispersity analysis using GPC.

### Experimental procedure for molecular weight control experiments in the presence of argon

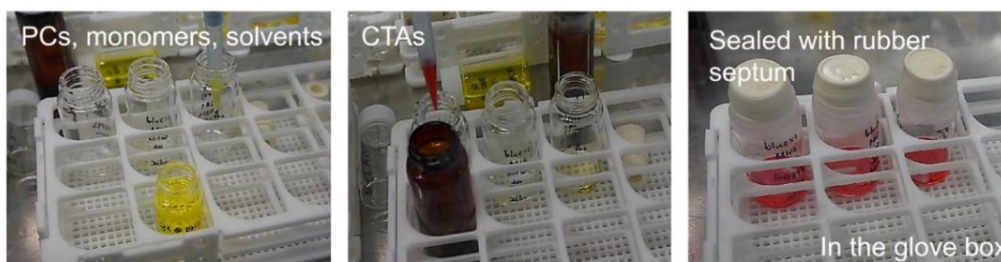
A typical PET-RAFT procedure for the standard reaction conditions of molecular weight control  $[\text{MMA}]:[\text{CPADB}]:[\text{4DP-IPN}] = [200]:[4]:[0.001]$  (target degree of polymerization (DP) = 50, MMA (1.0 mL, 9.29 mmol), CPADB (0.186 mmol), 4DP-IPN ( $4.65 \times 10^{-5}$  mmol) and DMSO (1.0 mL) as solvent),  $[\text{MMA}]:[\text{CPADB}]:[\text{4DP-IPN}] = [200]:[2]:[0.001]$  (target DP = 100, MMA (1.0 mL, 9.29 mmol), CPADB (0.093 mmol), 4DP-IPN ( $4.65 \times 10^{-5}$  mmol) and DMSO (1.0 mL) as solvent), and  $[\text{MMA}]:[\text{CPADB}]:[\text{4DP-IPN}] = [200]:[0.5]:[0.001]$  (target DP = 400, MMA (1.0 mL, 9.29 mmol), CPADB (0.023 mmol), 4DP-IPN ( $4.65 \times 10^{-5}$  mmol) and DMSO (1.5 mL) as solvent) under argon were carried out as follow. A 20 mL glass vial equipped with a stirring bar was charged with predetermined amounts of reagents, inside a glove box. After, the vial was capped with a rubber septum and sealed with parafilm, and bubbled with argon for 30 min outside the glove box. Subsequently, the polymerization was carried out under a 3 W 455 nm LED (ca.  $2.5 \text{ mW/cm}^2$ ) irradiation at room temperature. After 36 h (6 h for reaction condition  $[\text{MMA}]:[\text{CPADB}]:[\text{4DP-IPN}] = [200]:[0.5]:[0.001]$ ),

a 0.1 mL aliquot of the reaction mixture was removed via a syringe and dissolved in a vial containing  $\text{CDCl}_3$ . Without storing, the aliquot was then immediately analyzed using  $^1\text{H-NMR}$  for conversion. The sample used for  $^1\text{H-NMR}$  analysis was then dried under a reduced pressure and re-dissolved in THF for  $M_n$  and polydispersity analysis using GPC.

■STEP 1: Prepare stock solutions of PCs and CTA in the glove box



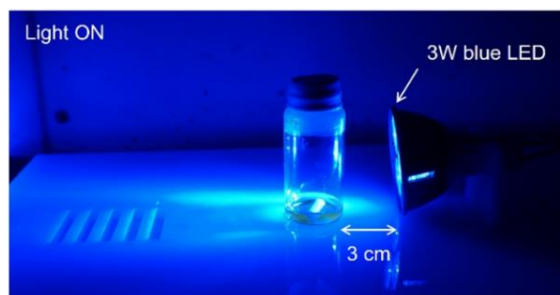
■STEP 2: Add PC, CTA, monomer, and solvent to 20 mL (of 4 mL for the polymerizations under air) vial with magnetic bar and seal with rubber septum inside the glove box.



■STEP 3: Cover with aluminum foils and degas with argon (or air) for 30 min.



■STEP 4: Irradiate under a 3W blue (or green) LED with stirring at r.t. for predetermined time.



■STEP 5: For kinetic studies (or in-situ monitoring of polymerizations), aliquot of the reaction mixture is taken by syringe and dissolved in a vial containing  $\text{CDCl}_3$  for  $^1\text{H}$  NMR. The samples used for  $^1\text{H}$  NMR analyses are then dried under reduced pressure and re-dissolved in THF for  $M_n$  and polydispersity analyses by GPC. For isolations, the reaction mixture is first diluted with 3 mL of THF and dissolved completely. Then, pour into beaker containing methanol (75 mL) and stir for 30 min and collect the polymers by vacuum filtration.

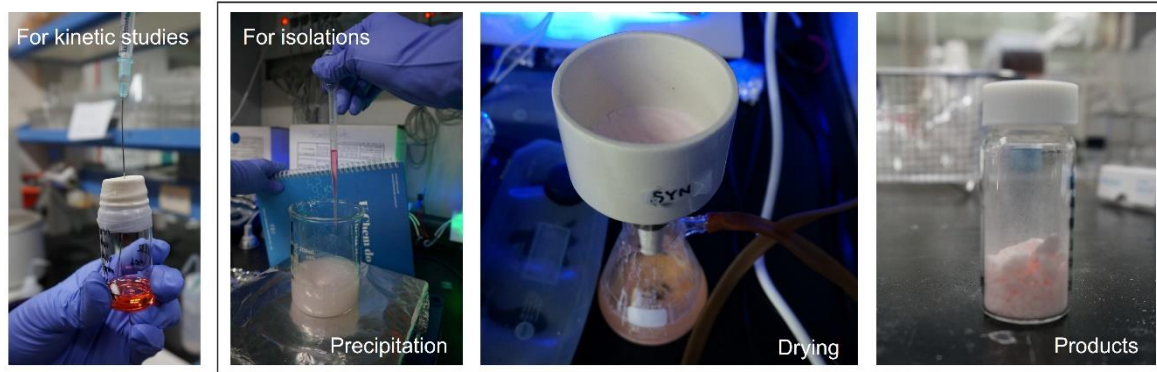


**Figure 11.** Graphical Supporting Information for General Procedure for PET-RAFT Polymerization of MMA.



## IV. Results and discussion

### 4.1 OPCs design logic

Good candidates for highly efficient PET-RAFT polymerization should show strong absorption in the visible and efficient triplet generation; in fact, triplet excited states have long lifetimes and are also less susceptible to back electron transfer between radical ions,<sup>44</sup> which thus assures efficient electron/energy transfer. For these reasons, ruthenium(II) and iridium(III) polypyridyl complexes, i.e., with long-lived lowest excited triplet ( $T_1$ ) states, are used as key PCs in a variety of photomediated reactions,<sup>45-47</sup> including photo-ATRP and PET-RAFT.<sup>5-10,13-16,21</sup> According to the recent reports by Boyer and co-workers,<sup>31</sup> the  $T_1$  states of PCs play an essential role in the oxygen tolerance of PET-RAFT. The  $T_1$  state reacts with molecular oxygen to form reactive oxygen species (ROS) by a type I and/or type II mechanism (**Figure 12**), which is well defined in the field of photodynamic therapy. The generated ROS are subsequently consumed by quenchers, thereby greatly reducing the dissolved oxygen concentration in the reaction medium and consequently providing oxygen tolerance.<sup>48</sup> Despite these facts, only a limited number of organic molecules that produce triplet states have been utilized as an OPC in photocatalysis,<sup>44</sup> in particular organocatalyzed PET-RAFT polymerizations.<sup>14,23-32</sup>

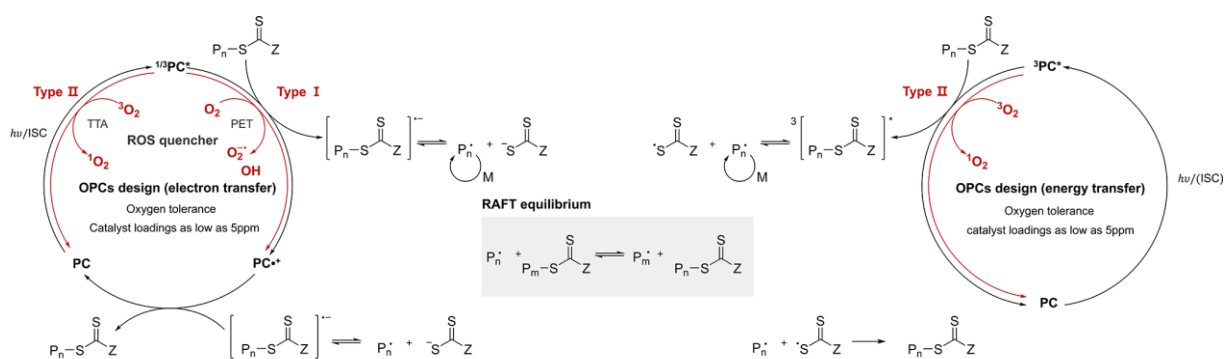
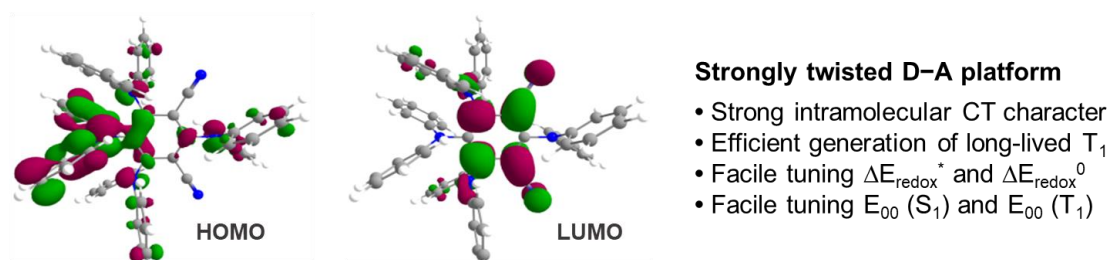


**Figure 12.** Proposed mechanisms for the PET-RAFT polymerization.  $^3PC$ , the lowest triplet excited state of a photocatalyst;  $^1/3PC$ , the lowest singlet and/or triplet excited states of a photocatalyst. (Reprinted with permission from **Reference 1**. Copyright 2019. American Chemical Society.).

We recently proposed a general platform for the design of highly efficient OPCs, i.e., strongly twisted D-A structures, which successfully addressed several important challenges in O-ATRP (**Figure 13**).<sup>22</sup>

The designed OPCs based on this platform have strong intramolecular charge-transfer (CT) character in the  $S_1$  state, and thus the  $T_1$  state is efficiently populated in the OPCs. Further, crucial catalyst parameters (e.g., ground/excited state redox potentials and triplet energies) can also be systematically tuned in broad ranges by simply adjusting the D and A groups. We therefore envisioned that our strategy could be applied to develop highly efficient OPCs for the visible-light-driven PET-RAFT with excellent oxygen tolerance.



**OPC requirements:**  $E_{\text{ox}}^* < -0.93 \text{ V}$ ,  $E_{\text{ox}}^0 > -0.93 \text{ V}$ ,  $E_{00}(S_1) < 2.90 \text{ eV}$ ,  $E_{00}(T_1) > 1.51 \text{ eV}$

**Figure 13.** General platform of the proposed OPCs, indicating the requirements for PET-RAFT polymerization. (Reprinted with permission from *Reference 1*. Copyright 2019. American Chemical Society.).

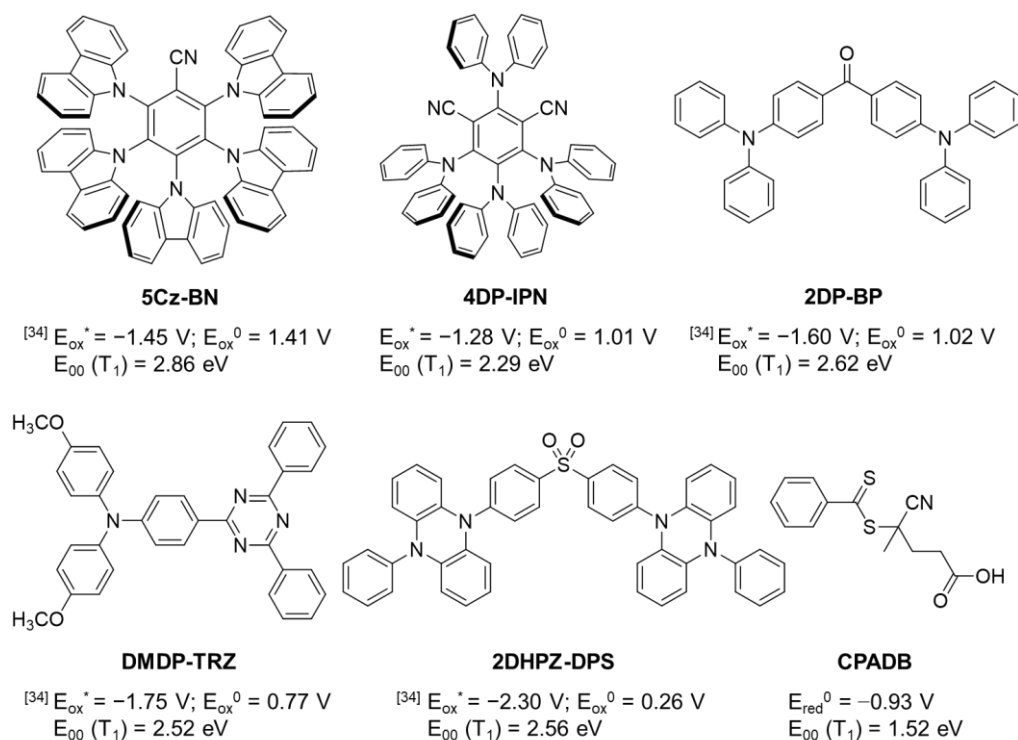


**Figure 14.** Structures and properties of OPCs studied in the current work, selected from our OPC library. (Reprinted with permission from *Reference 1*. Copyright 2019. American Chemical Society.).

**Table 1.** Photophysical and electrochemical properties of OPCs in our library.

Entry	Absorption (nm)	Excited state energies (eV)			Ground state redox potentials (V vs SCE)			Excited state redox potentials (V vs SCE)				CV reversibility	
	$\lambda_{max}(\lambda_{onset})$	$E_{00}(S_1)$	$E_{00}(T_1)$	$\Delta E_{ST}$	$E_{ox}^o$	$E_{red}^o$	$E_{ox}^*(S_1)$	$E_{ox}^*(T_1)$	$E_{red}^*(S_1)$	$E_{red}^*(T_1)$	$PC^{+}$	$PC^{-}$	
<b>1a</b>	384 (450)	2.93	2.86	0.07	+1.41	-1.50	-1.52	-1.45	1.43	1.36	<i>ir</i>	<i>r</i>	
<b>1b</b>	400 (469)	2.84	2.78	0.06	+1.12	-1.61	-1.72	-1.66	1.23	1.17	<i>r</i>	<i>r</i>	
<b>2a</b>	431 (485)	2.72	2.75	-0.03	+1.52	-1.21	-1.2	-1.23	1.51	1.54	<i>ir</i>	<i>r</i>	
<b>2b</b>	451 (513)	2.62	2.62	0.00	+1.30	-1.31	-1.32	-1.32	1.31	1.31	<i>r</i>	<i>r</i>	
<b>2c</b>		2.59	2.42	0.17	+1.01	-1.66	-1.58	-1.41	0.93	0.76	<i>r</i>	<i>r</i>	
<b>3a</b>	360 (418)	3.1	2.95	0.15	+1.28	-1.64	-1.82	-1.67	1.46	1.31	<i>ir</i>	<i>r</i>	
<b>3b</b>	363 (436)	3.06	2.93	0.13	+1.05	-1.66	-2.01	-1.88	1.4	1.27	<i>r</i>	<i>r</i>	
<b>3c</b>	375 (445)	3.04	2.62	0.42	+1.02	-1.84	-2.02	-1.6	1.2	0.78	<i>r</i>	<i>r</i>	
<b>3d</b>	401 (485)	2.71	2.52	0.19	+0.79	-1.61	-1.92	-1.73	1.1	0.91	<i>r</i>	<i>r</i>	
<b>3e</b>	343 (433)	3.21	2.93	0.28	+0.74	-1.73	-2.47	-2.19	1.48	1.2	<i>r</i>	<i>r</i>	
<b>4a</b>	338 (385)	3.46	3.12	0.34	+1.32	-1.96	-2.14	-1.8	1.5	1.16	<i>lr</i>	<i>ir</i>	
<b>4b</b>	346 (397)	3.35	3.08	0.27	+1.26	-2.06	-2.09	-1.82	1.29	1.02	<i>r</i>	<i>ir</i>	
<b>4c</b>	346 (399)	3.3	2.85	0.45	+1.06	-2.15	-2.24	-1.79	1.15	0.7	<i>r</i>	<i>ir</i>	
<b>4d</b>	383 (454)	2.83	2.81	0.02	+0.84	-1.87	-1.99	-1.97	0.96	0.94	<i>r</i>	<i>ir</i>	
<b>4g</b>	431 (524)	2.59	2.56	0.03	+0.26	-1.98	-2.33	-2.30	0.61	0.58	<i>r</i>	<i>r</i>	
<b>5a</b>	433 (541)	2.36	2.19	0.17	+1.43	-0.84	-0.93	-0.76	1.52	1.35	<i>lr</i>	<i>r</i>	
<b>5b</b>	463 (563)	2.44	2.29	0.15	+1.28	-0.87	-1.16	-1.01	1.57	1.42	<i>r</i>	<i>r</i>	
<b>5c</b>	445 (588)	2.27	n.d.	n.d.	+1.20	-0.83	-1.07	n.d.	1.44	n.d.	<i>lr</i>	<i>r</i>	
<b>5d</b>	529 (677)	n.d.	n.d.	n.d.	+0.79	-0.74	n.d.	n.d.	n.d.	n.d.	<i>r</i>	<i>r</i>	
<b>5e</b>	408 (538)	2.53	n.d.	n.d.	+0.82	-0.91	-1.71	n.d.	1.62	n.d.	<i>r</i>	<i>r</i>	
<b>6a</b>	359 (422)	3.27	2.88	0.39	+1.30	-1.63	-1.97	-1.58	1.64	1.25	<i>ir</i>	<i>r</i>	
<b>6b</b>	373 (439)	3.1	2.85	0.25	+1.20	-1.65	-1.9	-1.65	1.45	1.2	<i>r</i>	<i>r</i>	
<b>6c</b>	388 (465)	2.96	2.59	0.37	+1.0	-1.73	-1.96	-1.59	1.23	0.86	<i>ir</i>	<i>r</i>	
<b>6d</b>	411 (481)	2.65	2.43	0.22	+0.73	-1.63	-1.92	-1.7	1.02	0.8	<i>r</i>	<i>r</i>	
<b>6e</b>	363 (468)	3.3	2.82	0.48	+0.73	-1.62	-2.57	-2.09	1.68	1.2	<i>r</i>	<i>r</i>	
<b>6f</b>	390 (501)	2.66	2.52	0.14	+0.77	-1.76	-1.89	-1.75	0.9	0.76	<i>r</i>	<i>r</i>	
<b>7b</b>	348 (406)	3.46	n.d.	n.d.	+1.21	-2.05	-2.25	n.d.	1.41	n.d.	<i>r</i>	<i>r</i>	
<b>8b</b>	360 (420)	3.28	n.d.	n.d.	+1.18	-1.91	-2.1	n.d.	1.37	n.d.	<i>r</i>	<i>r</i>	
<b>9b</b>	387 (488)	2.93	2.58	0.35	+1.26	-1.07	-1.67	-1.32	1.86	1.51	<i>r</i>	<i>r</i>	
<b>10b</b>	396 (507)	2.84	2.35	0.49	+1.20	-1.37	-1.64	-1.15	1.47	0.98	<i>r</i>	<i>r</i>	
<b>11b</b>	386 (470)	2.75	2.49	0.26	+1.21	-1.06	-1.54	-1.28	1.69	1.43	<i>r</i>	<i>r</i>	

We first selected OPCs from our library<sup>22</sup> by considering triplet exciton generation, visible-light absorption, ground and excited state redox potentials, and triplet energies (**Figure 14**; for our OPC library, **Figure 4** and **Table 1**). It should be noted that we here consider both redox potentials and triplet energies for the selection of OPCs, as two different mechanisms (i.e., photoinduced electron and energy transfer) can be involved in PET-RAFT (**Figure 12**). In fact, according to recent reports,<sup>49,50</sup> photoinduced energy transfer is the more plausible pathway in PET-RAFT polymerization using Ir(ppy)<sub>3</sub> or Ru(bpy)<sub>3</sub><sup>2+</sup>; however, it is still unclear for polymerization reactions using other type of catalysts. For our chosen RAFT agent (i.e., CPADB; for molecular structure, **Figure 14**), the ground state reduction potential ( $E_{\text{red}}^0 \approx -0.93$  V; potential versus SCE, **Figure 15**) and (relaxed) triplet energy  $E_{00}(T_1) = 1.51$  eV (obtained from TD-DFT; for details, **Figure 16**) are quite low. Therefore, rather low levels for  $E_{\text{ox}}^0$ ,  $E_{\text{ox}}^*(T_1)$ , and  $E_{00}(T_1)$  are required ( $E_{\text{ox}}^0 > \text{ca. } -0.93$  V,  $E_{\text{ox}}^*(T_1) < \text{ca. } -0.93$  V, and  $E_{00}(T_1) > 1.51$  eV, respectively). As a comparison for the chosen OPCs, we also investigated Ir(ppy)<sub>3</sub>, fluorescein, eosin Y, and 4Cz-IPN. A full description of the synthetic approaches, UV-Vis, cyclic voltammetry (CV), and <sup>1</sup>H-NMR is found in the **Figures 36–39** and **43–52**.

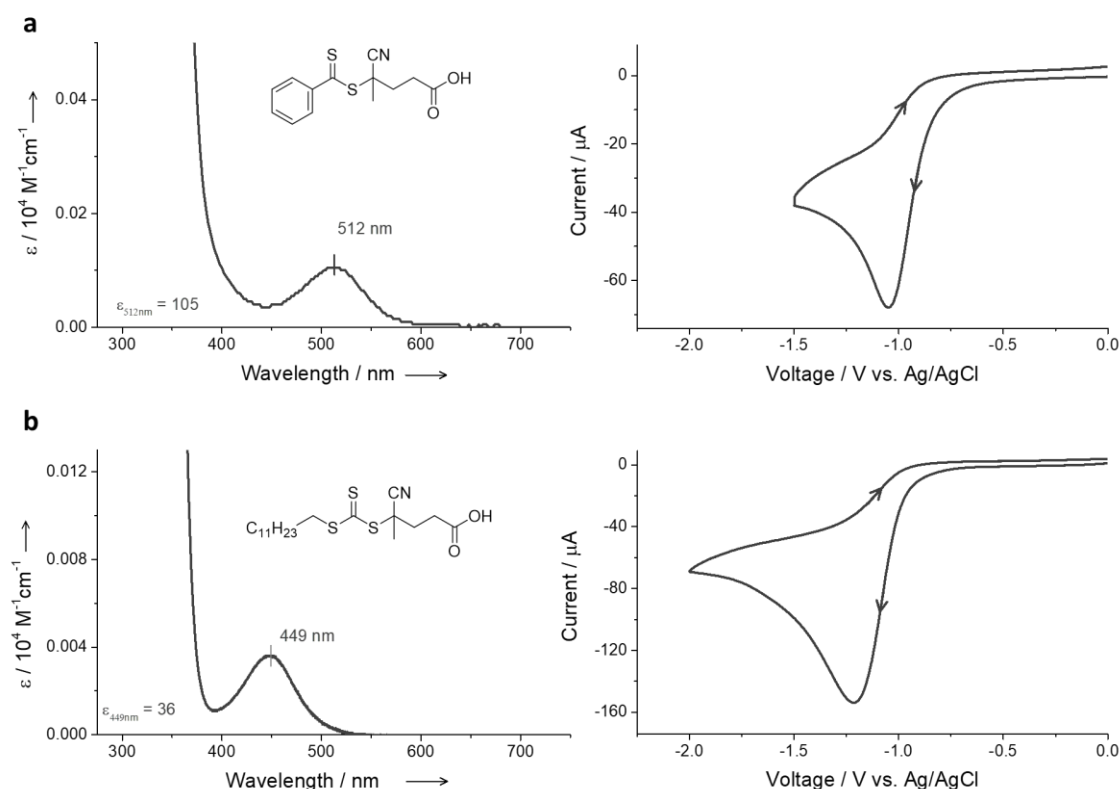


**Figure 15.** UV-Vis spectra (left) and CV curves (right) of (a) CPADB and (b) CDTPA. UV-vis measurements were performed in DMSO with [CTA] = 20  $\mu$ M. CV measurements were done in 0.2 mM CH<sub>3</sub>CN solution with 0.1 M nBu<sub>4</sub>NPF<sub>6</sub> as supporting electrolyte at a scan rate of 100 mV/s.

in DMF: B3LYP/6-311+G\*

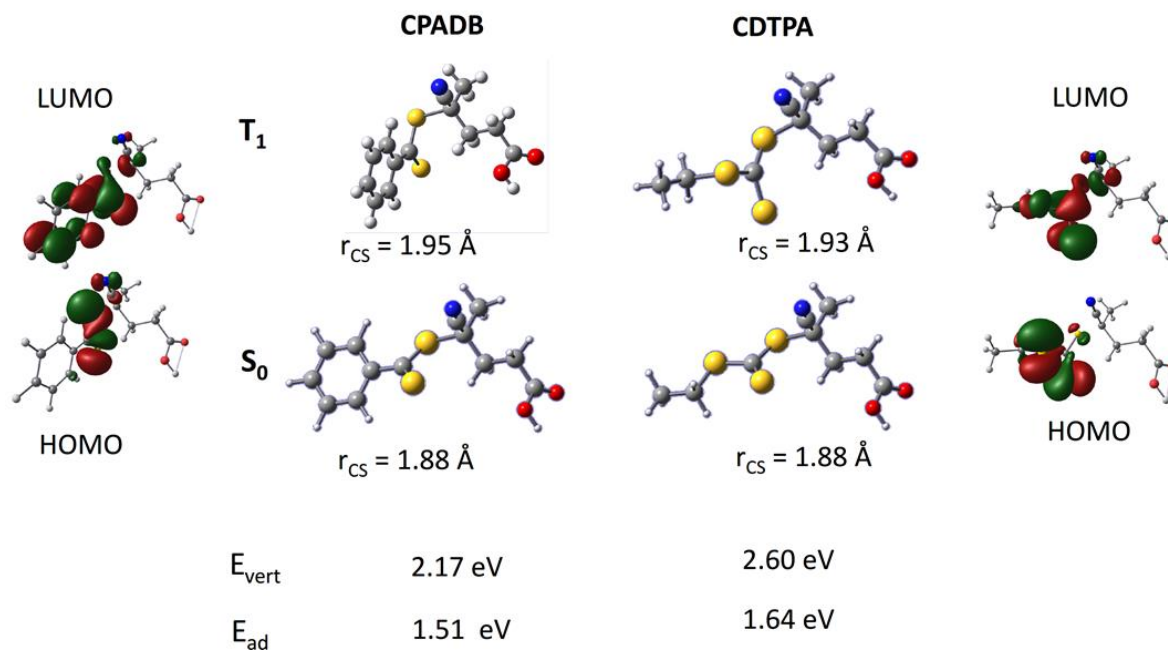
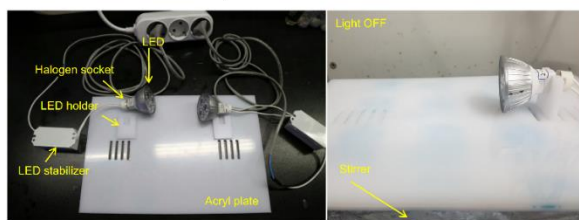


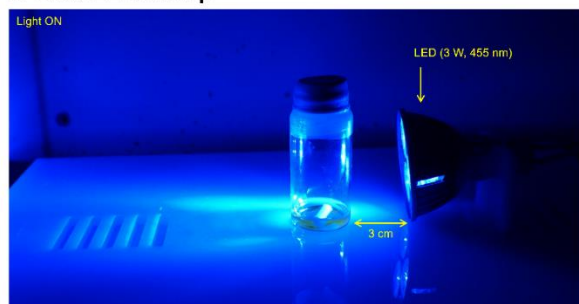
**Figure 16.** Properties of CPADB and CDTPA: Molecular geometries in  $S_0$  and  $T_1$  (the latter is exclusively described by a HOMO→LUMO excitation); corresponding frontier MOs. Adiabatic and vertical transition energies in DMF.

## 4.2 Polymerization studies under Argon

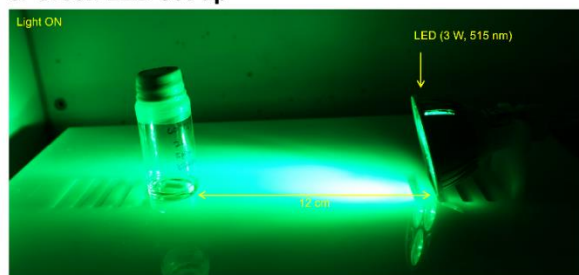
a. Normal LED set-up



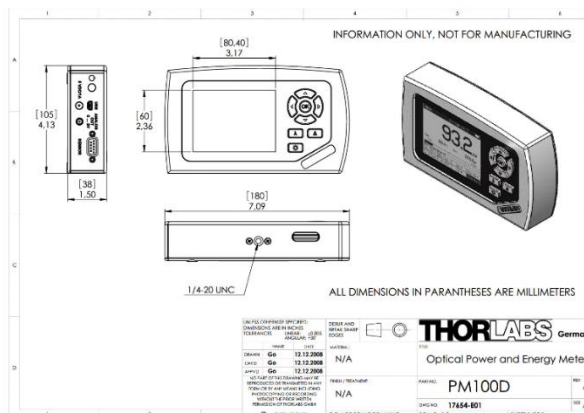
b. Blue LED set-up



c. Green LED set-up



d. Photodiode



e. Emission spectra

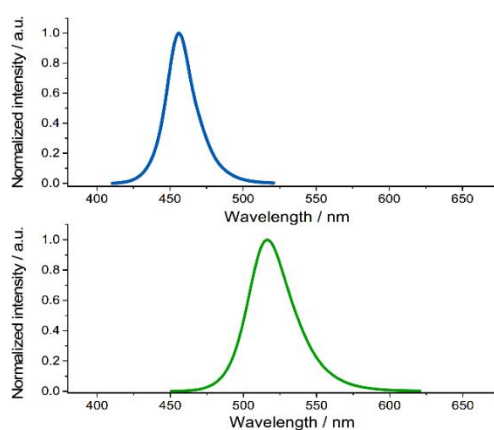
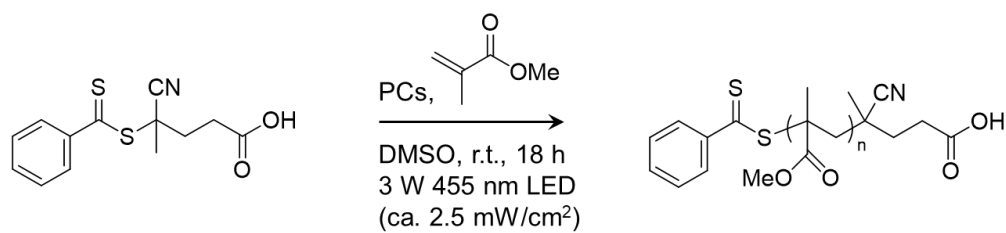


**Figure 17.** Pictures of (a) individual parts and our LED set-ups in operation (b) under blue light and (c) under green light. (d) Basic information of photodiode for measuring the light intensity of the excitation light sources (blue and green LEDs) (e) Normalized emission spectra for the blue LEDs (top, maximum intensity wavelength = ca. 455 nm) and green LEDs (bottom, maximum intensity wavelength = ca. 515 nm).

We investigated the photocatalytic performance of the chosen OPCs under 3 W blue LED irradiation conditions (for the details of polymerization setup, **Figure 17**). DMSO was selected as a solvent since it is commonly used for PET-RAFT, and, more importantly, it works as an effective ROS quencher.<sup>20,51,52</sup> As a negative control, the polymerization of MMA was performed in the absence of a PC under argon (Ar) atmosphere (**Table 2**, entry control, and **Figure 18**). This control experiment gave poly(methyl methacrylate) (PMMA) in relatively low yield of 20% but showed a good control of polymerization exemplified by a dispersity ( $\mathcal{D}$ ) value of 1.17 and an initiator efficiency ( $I^*$ ) of 0.73 (**Table 2**). This

indicates that CPADB acts as a photoiniferter as reported in previous works.<sup>15,53</sup> To validate our PET-RAFT setup, we then performed the same polymerization with Ir(ppy)<sub>3</sub> of 1 ppm under Ar. As shown in **Table 2**, entry 1, the obtained results are well in accordance with the data from Boyer's group,<sup>20</sup> clearly certifying the reliability of our data.

**Table 2.** Results for the PET-RAFT polymerization of MMA in the presence of different PCs at room temperature under Argon (Ar) and Air; 3 W Blue LED illumination (455 nm, ca. 2.5 mW/cm<sup>2</sup>) (Reprinted with permission from **Reference 1**. Copyright 2019. American Chemical Society.).



Entry	PCs	Atmosphere	[M]:[I]:[PC]	$\alpha$ (%)	$M_{n,theo}$ (g/mol)	$M_{n,exp}$ (g/mol)	$\bar{D}$	$I^*$
Control	No catalyst	Ar	200:1:0	20	4400	6000	1.17	0.73
Control	No catalyst	Air	200:1:0	9	2000	5000	1.28	0.40
1	Ir(ppy) <sub>3</sub>	Ar	200:1:0.0002	86	17600	21900	1.23	0.80
2	Ir(ppy) <sub>3</sub>	Air	200:1:0.0002	72	14800	23600	1.39	0.63
3	Eosin Y	Ar	200:1:0.001	47	9600	11000	1.12	0.87
4	Eosin Y	Air	200:1:0.001	8	1800	4200	1.32	0.43
5	Fluorescein	Ar	200:1:0.001	41	8400	9300	1.12	0.90
6	Fluorescein	Air	200:1:0.001	3	860	2900	1.29	0.30
7	5Cz-BN	Ar	200:1:0.001	29	6100	8100	1.15	0.75
8	5Cz-BN	Air	200:1:0.001	35	7400	11600	1.16	0.64
9	4Cz-IPN	Ar	200:1:0.001	40	8200	10400	1.13	0.79
10	4Cz-IPN	Air	200:1:0.001	22	4600	8000	1.36	0.58
11	4DP-IPN	Ar	200:1:0.001	62	12700	14000	1.11	0.91
12	4DP-IPN	Air	200:1:0.001	70	14200	24100	1.26	0.59
13	2DP-BP	Ar	200:1:0.001	38	7800	8600	1.14	0.91
14	2DP-BP	Air	200:1:0.001	10	2300	4500	1.29	0.51
15	2DHPZ-DPS	Ar	200:1:0.001	12	2600	4300	1.20	0.60
16	2DHPZ-DPS	Air	200:1:0.001	21	4600	8000	1.18	0.58
17	DMDP-TRZ	Ar	200:1:0.001	33	6800	9200	1.13	0.74
18	DMDP-TRZ	Air	200:1:0.001	43	8900	13800	1.15	0.64

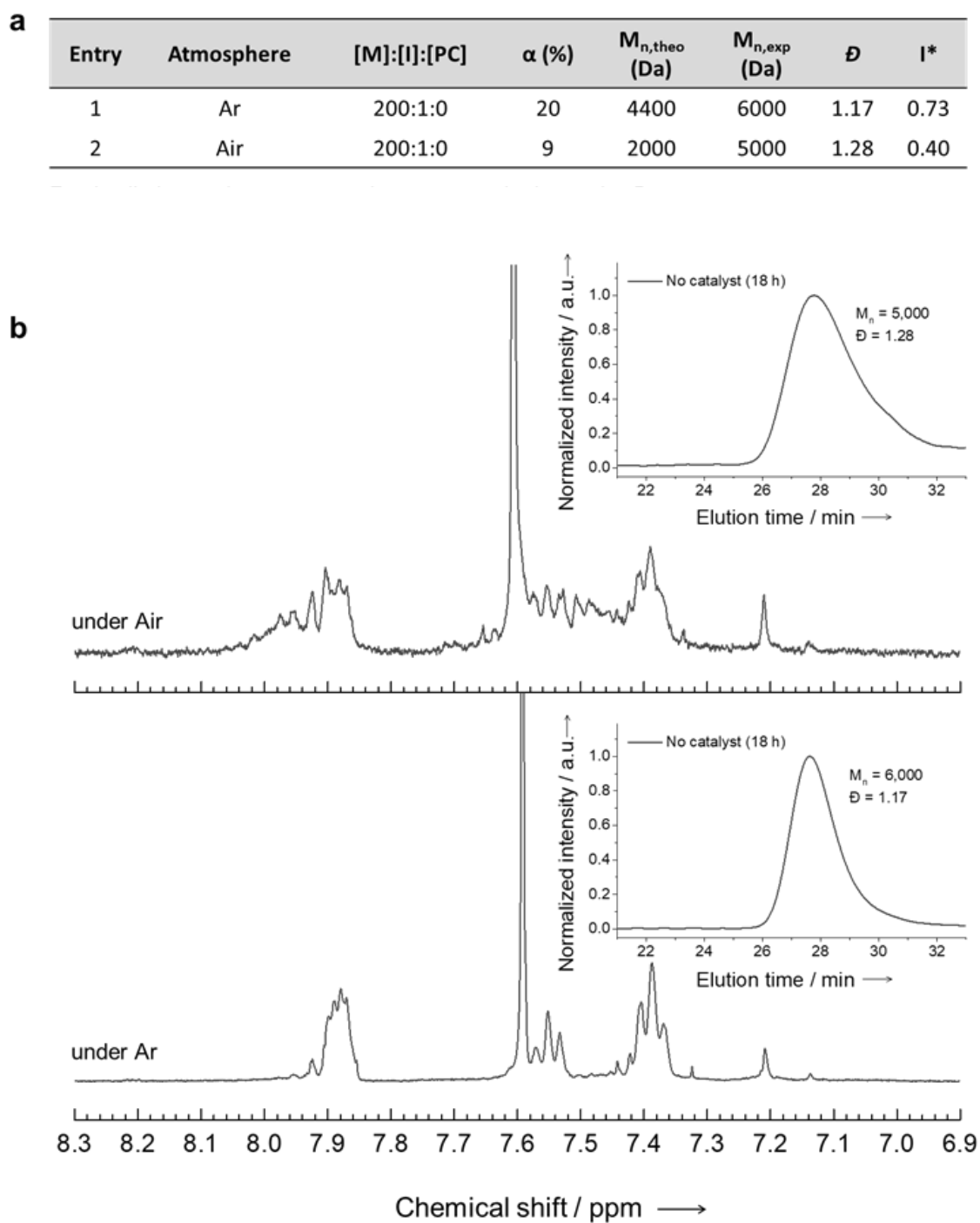


**Figure 18.** (a) Negative control experiments of PET-RAFT of MMA in the presence of argon and air using CPADB. (b) <sup>1</sup>H-NMR spectra and GPC traces of the reaction mixtures obtained after PET-RAFT polymerizations of MMA under air (up) and argon (bottom).



The results of PET-RAFT of MMA with the selected OPCs are summarized in **Table 2**; we here used 5 ppm of OPCs for polymerizations, as the results for 1 ppm were not satisfying (**Table 3**). For all OPCs, PMMA polymers were obtained with a considerably narrow molecular weight distribution ( $\mathcal{D} = 1.11\text{--}1.23$ ) and high initiator efficiencies ( $I^* = 0.60\text{--}0.91$ ; **Table 2**). In particular, 4DP-IPN facilitated considerably high conversion of 62% with an excellent control ( $\mathcal{D} = 1.11$  and  $I^* = 0.91$ ), comparable to those of  $\text{Ir}(\text{ppy})_3$ ; for other OPCs, polymers were mostly obtained in less than ca. 40% conversion. All results were highly reproducible as seen in **Table 4**. Using 4DP-IPN, the number-average molecular weight ( $M_n$ ) of PMMA can also be modulated in the range of 4.2–27 kg/mol with a narrow molecular weight distribution ( $\mathcal{D} < 1.20$ ), high initiator efficiency ( $I^* > 0.70$ ), and reasonable conversions (**Table 5**). Polymerization kinetics were then monitored by  $^1\text{H-NMR}$  and GPC for 4DP-IPN (5 ppm) under Ar (**Figure 19a,b**); kinetics for  $\text{Ir}(\text{ppy})_3$  (1 ppm) were performed for comparison (**Table 6**). A linear relationship of monomer conversion vs an exposure time, and of  $M_n$  vs conversion, was found for both PCs, demonstrating the living character of these polymerizations. Moreover, after 18 h of polymerization, characteristic chemical shifts of the functionality of dithiobenzoate at 7.88, 7.52, and 7.36 ppm are clearly seen in  $^1\text{H-NMR}$ ; no indication of byproducts was found, which confirms the high end-group fidelities of the polymers (**Figures 20, 21, 3c**). As expected, the chain extension of PMMA with MMA was also successful, resulting in the synthesis of PMMA-*b*-PMMA with a narrow molecular weight distribution ( $\mathcal{D} = 1.12$ , **Figures 21**). Through light “ON” and “OFF” experiments, we also observed a good temporal control in polymerization (**Figures 19c and 20**).

**Table 3.** Results of PET-RAFT polymerization of MMA in the presence of CPADB using 4DP-IPN of 1 ppm under argon. All polymerizations were performed at room temperature under a 3 W blue LED (455 nm, ca. 2.5 mW/cm<sup>2</sup>).

Entry <sup>a</sup>	PC	Bubbling	[M]:[I]:[PC]	Conversion (%)	$M_{n,\text{theo}}$ (Da)	$M_{n,\text{exp}}$ (Da)	$\mathcal{D}$	$I^*$
1 <sup>b</sup>	4DP-IPN	Ar	200:1:0.001	62	12700	14000	1.11	0.91
2	4DP-IPN	Ar	200:1:0.0002	41	8500	10300	1.11	0.83
3	4DP-IPN	Ar	200:1:0.0002	41	8600	10400	1.11	0.83

**Table 4.** Reproducibility test. Experiments were performed in many different set-ups by students in our group.

Entry <sup>a</sup>	PC	Bubbling	[M]:[I]:[PC]	Conversion (%)	$M_{n,theo}$ (Da)	$M_{n,exp}$ (Da)	$\bar{D}$	$I^*$
1 <sup>b</sup>	4DP-IPN	Ar	200:1:0.001	62	12700	14000	1.11	0.91
2	4DP-IPN	Ar	200:1:0.001	63	13000	13900	1.13	0.94
3	4DP-IPN	Ar	200:1:0.001	76	15500	17400	1.14	0.89
4	4DP-IPN	Ar	200:1:0.001	67	13600	15400	1.13	0.88
5	4DP-IPN	Ar	200:1:0.001	69	14000	16600	1.14	0.84
6	4DP-IPN	Ar	200:1:0.001	58	11800	13300	1.13	0.89
7 <sup>b</sup>	4DP-IPN	Air	200:1:0.001	70	14200	24100	1.26	0.59
8	4DP-IPN	Air	200:1:0.001	74	15000	25100	1.22	0.60
9	4DP-IPN	Air	200:1:0.001	88	17900	26700	1.34	0.67
10	4DP-IPN	Air	200:1:0.001	89	18100	23900	1.27	0.76
11	4DP-IPN	Air	200:1:0.001	76	15400	24200	1.37	0.64
12 <sup>c</sup>	4DP-IPN	Air	200:1:0.001	84	17100	36400	1.42	0.47

**Table 5.** Control of molecular weight of PMMA in the presence of argon using CPADB and 4DP-IPN of 5 ppm. <sup>1</sup>H-NMR spectra and GPC curves of the resulting polymers are in **Figure 42**.

Entry <sup>a</sup>	PC	Bubbling	[M]:[I]:[PC]	Conversion (%)	$M_{n,theo}$ (Da)	$M_{n,exp}$ (Da)	$\bar{D}$	$I^*$
1 <sup>b</sup>	4DP-IPN	Ar	200:4:0.001	64	3500	4200	1.13	0.83
2 <sup>b</sup>	4DP-IPN	Ar	200:2:0.001	78	8100	8300	1.13	0.98
3 <sup>c</sup>	4DP-IPN	Ar	200:1:0.001	62	12700	14000	1.11	0.91
4 <sup>d</sup>	4DP-IPN	Ar	200:0.5:0.001	51	20700	27000	1.20	0.77

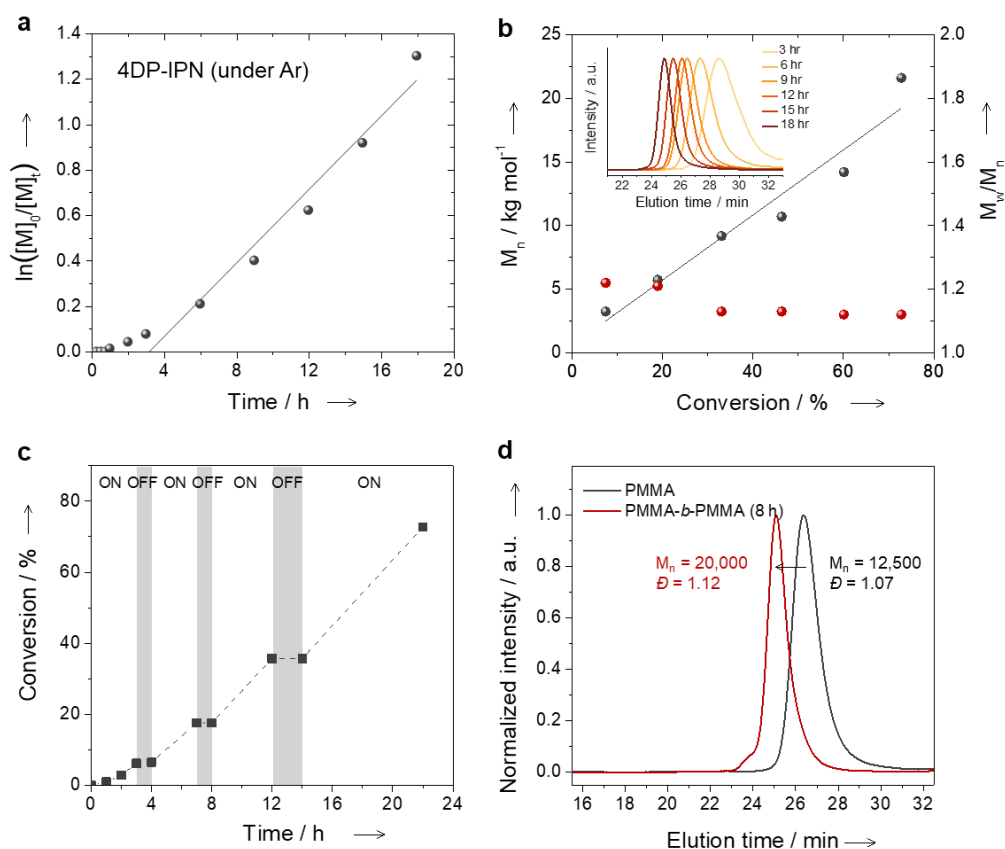


**Figure 19.** Kinetic plots for PET-RAFT polymerization of MMA under Ar using 4DP-IPN (5 ppm). **(a)**  $\ln([M]_0/[M]_t)$  versus reaction time. **(b)**  $M_n$  versus conversion (black circle) and  $M_w/M_n$  versus conversion (red circle); for GPC traces at different reaction, see inset of **Figure 22c**. **(c)** Light ON/OFF experiment for PET-RAFT polymerization of MMA using CPADB and 4DP-IPN of 5 ppm. **(d)** GPC traces of PMMA (black) and diblock of PMMA-*b*-PMMA (red) (*Reprinted with permission from Reference 1. Copyright 2019. American Chemical Society.*).

**Table 6.** Chain extensions of PMMA in the presence of argon using  $\text{Ir}(\text{ppy})_3$  of 1 ppm and 4DP-IPN of 5 ppm.

Entry	PC	Atmosphere	[M]:[I]:[PC]	$\alpha$ (%)	$M_{n,theo}$ (Da)	$M_{n,exp}$ (Da)	$\bar{D}$	$I^*$
1 <sup>a</sup>	$\text{Ir}(\text{ppy})_3$	Ar	200:1:0.0002	53	10800	14000	1.14	0.77
2 <sup>b</sup>	$\text{Ir}(\text{ppy})_3$	Ar	200:1:0.0002	-	-	15700	1.07	
3 <sup>c</sup>	$\text{Ir}(\text{ppy})_3$	Ar	200:1:0.0002	-	-	23900	1.12	
4 <sup>a</sup>	4DP-IPN	Ar	200:1:0.001	36	7500	10600	1.14	0.71
5 <sup>b</sup>	4DP-IPN	Ar	200:1:0.001	-	-	12500	1.07	
6 <sup>c</sup>	4DP-IPN	Ar	200:1:0.001	-	-	20000	1.12	

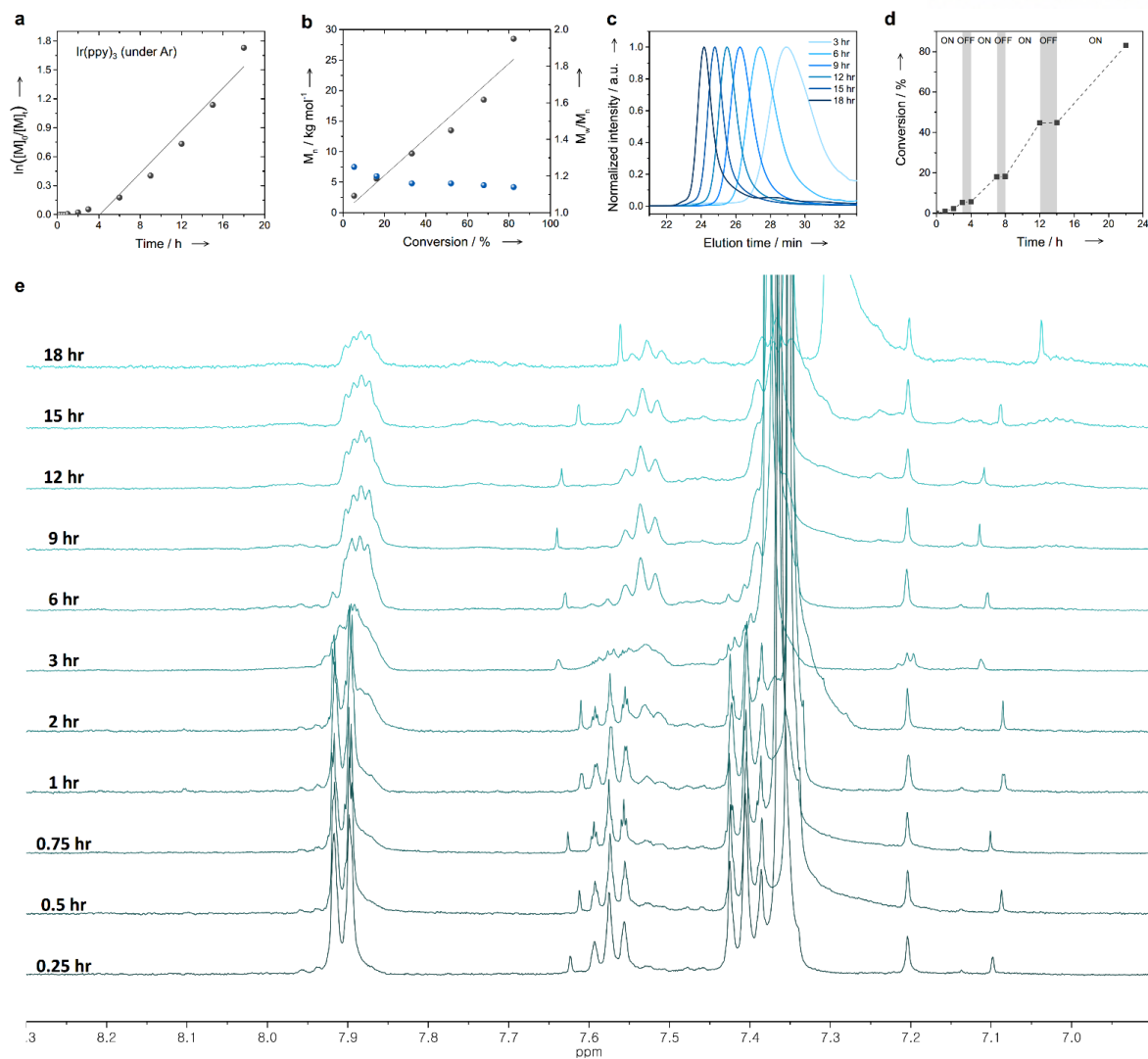


**Figure 20.** Kinetic plots for PET-RAFT polymerizations of MMA in the presence of argon using  $\text{Ir}(\text{ppy})_3$  of 1 ppm. **(a)**  $\ln([M]_0/[M]_t)$  versus reaction time. **(b)**  $M_n$  versus conversion (black circle) and  $M_w/M_n$  versus conversion (blue circle). **(c)** GPC traces at different reaction time. **(d)** Light "ON"/"OFF" experiment for PET-RAFT polymerization of MMA using CPADB and  $\text{Ir}(\text{ppy})_3$  of 1 ppm. **(e)**  $^1\text{H-NMR}$  spectra at different reaction time.

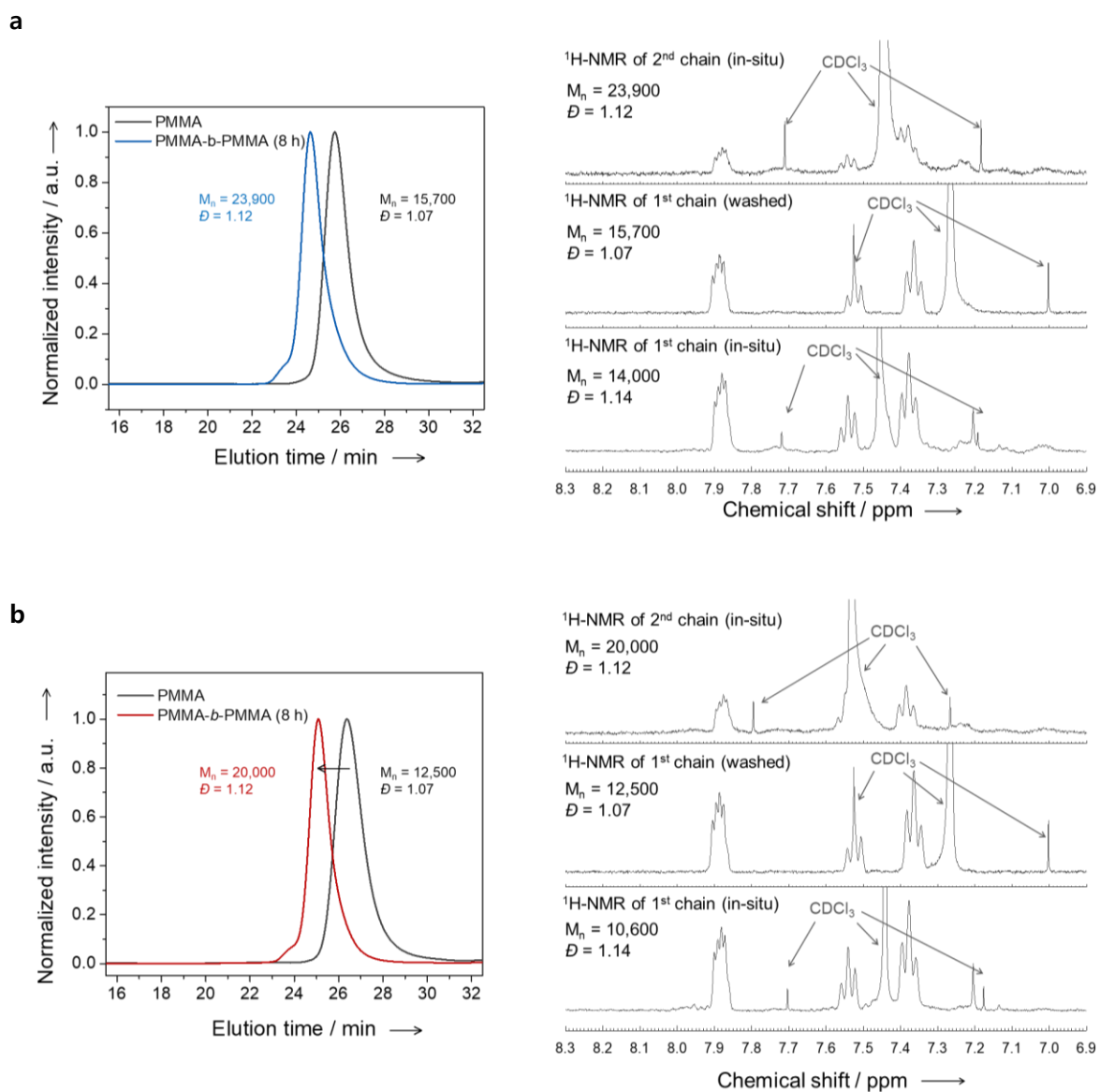


**Figure 21.** GPC traces of PMMA and diblock of PMMA-*b*-PMMA and  $^1\text{H-NMR}$  spectra of washed (middle) and in-situ (bottom) 1<sup>st</sup> chain and in-situ (top) 2<sup>nd</sup> chain using (a) Ir(ppy)<sub>3</sub> of 1 ppm and (b) 4DP-IPN of 5 ppm under argon.

### 4.3 Oxygen tolerance

In a next step, we investigated the oxygen tolerance of PET-RAFT polymerization using our OPCs. To increase the reproducibility and minimize the effect of moisture, mixed solutions of monomers, initiators, and catalysts were prepared in the glovebox and bubbled with commercially purchased air for 30 min outside the glovebox. According to Boyer's procedure,<sup>20,51,52</sup> all polymerizations were carried out in a sealed vial of 4 mL using a total liquid volume of 3 mL (1:1, v/v of monomer/solvent).

As shown in **Table 2**, polymerization in the presence of 4DP-IPN of 5 ppm under air provided a fairly good control ( $\bar{D} = 1.26$  and  $I^* = 0.59$ ) with a reasonable conversion of 70%, which is better than the performance of most catalysts (and comparable to that of  $\text{Ir}(\text{ppy})_3$ ) under the same conditions but clearly inferior to the results under Ar atmosphere. To reveal the origin of the lack of control for polymerization under air, the reaction was monitored by  $^1\text{H-NMR}$  (**Figures 22 and 23**); polymerization with  $\text{Ir}(\text{ppy})_3$  of 1 ppm under same conditions was also monitored for comparison (**Figure 24**). Interestingly, new chemical shift signals at 7.96, 7.59, and 7.44 ppm appeared 3 h after the reaction and became distinct after 18 h of the reaction (**Figures 22c and 23**). The characteristics of the new signals (i.e., broad shape and downfield shift from the signals of the dithiobenzoate functional group) imply that the end functional group of polymers had changed to a more electron-deficient functional group such as a thioester and a dithioester S-oxide group (**Figure 22c**). We speculated that dithiobenzoate moiety would have been oxidized through the reaction with the remaining ROS, which were not fully quenched by DMSO. This assumption is also supported by the fact that thioketone moiety is oxidized to the corresponding ketone and thiocarbonyl S-oxides (sulfine) in the presence of air and photosensitizer under blue LED irradiation conditions (**Figure 22c**).<sup>54</sup> In any case, the detailed mechanism of photoinduced oxidation of dithiobenzoate group is not yet fully understood, although the suggested mechanism is given in **Figure 23**. In fact, there is no report on the photoinduced oxidation of CTAs (while the photodegradation of CTAs under Ar atmosphere has recently been investigated by Qiao and co-workers<sup>53</sup>).

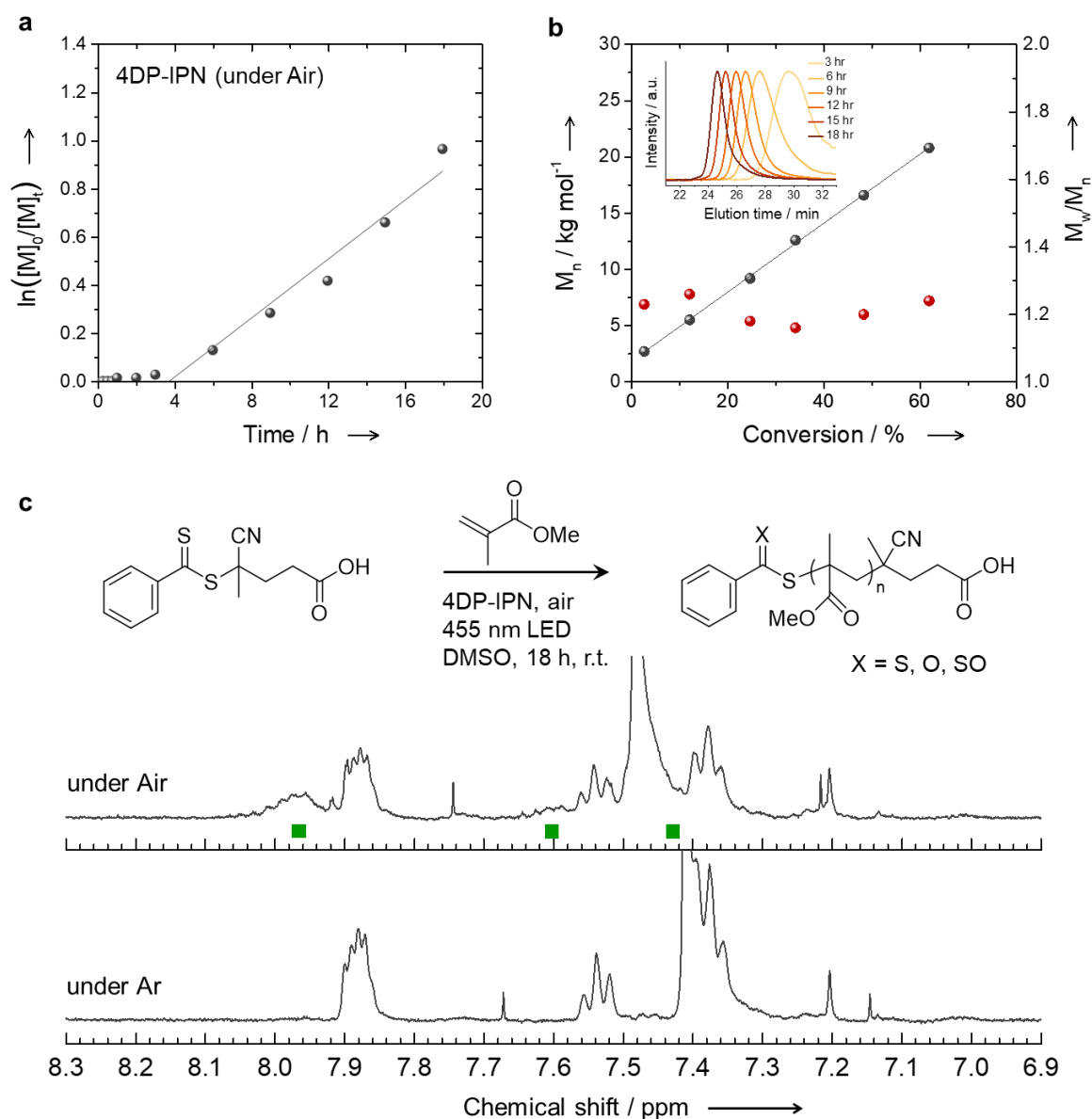


**Figure 22.** Kinetic plots for PET-RAFT polymerization of MMA under air for 4DP-IPN (5 ppm). **(a)**  $\ln([M]_0/[M]_t)$  versus a reaction time. **(b)**  $M_n$  versus conversion (black circle) and  $M_w/M_n$  versus conversion (red circle). Inset shows GPC traces at different reaction times. Experimental condition:  $[MMA]:[CPADB]:[4DP-IPN] = 200:1:0.001$  in DMSO. **(c)** <sup>1</sup>H-NMR spectra of the reaction mixtures obtained after the PET-RAFT polymerization of 18 h without purifications under air (up) and Ar (bottom) in the presence of CPADB, MMA, and 4DP-IPN of 5 ppm (*Reprinted with permission from Reference 1. Copyright 2019. American Chemical Society.*).

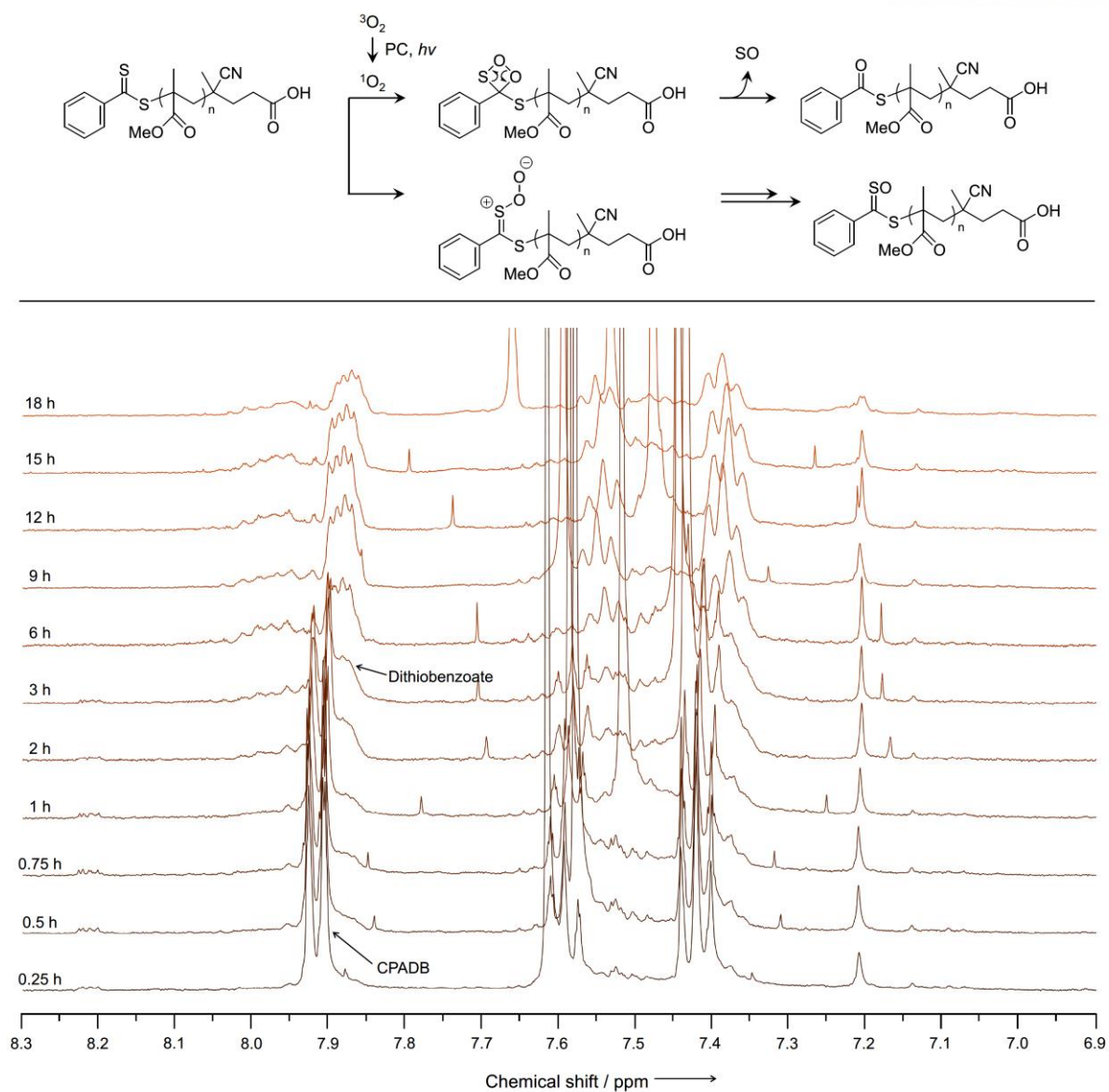


**Figure 23.** <sup>1</sup>H-NMR spectra of the polymerization mixtures using CPADB and 4DP-IPN (5 ppm) at different reaction times. Suggested mechanism for the photo-oxidation of CPADB is given in the top.



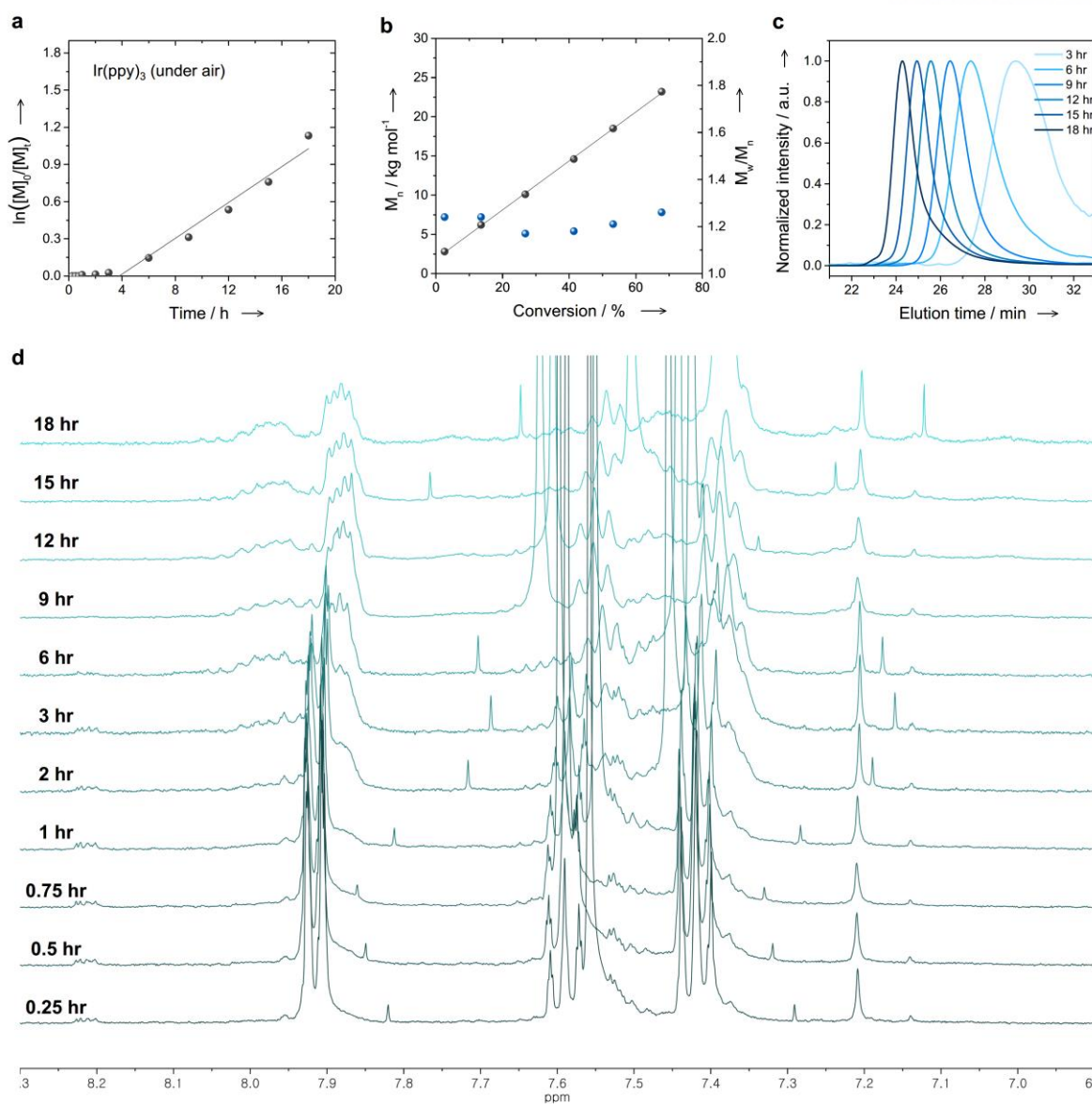


**Figure 24.** Kinetic plots for PET-RAFT polymerizations of MMA in the presence of air using  $\text{Ir}(\text{ppy})_3$  of 1 ppm. **(a)**  $\ln([M]_0/[M]_t)$  versus a reaction time. **(b)**  $M_n$  versus conversion (black circle) and  $M_w/M_n$  versus conversion (blue circle). **(c)** GPC traces at a different reaction time. **(d)** <sup>1</sup>H-NMR spectra of kinetic study at a different reaction time.

#### 4.4 PET-RAFT polymerizations with trithiocarbonate-based CTA

According to He and co-workers,<sup>55</sup> the stability of dithioester compounds toward radical-induced oxidation greatly depends on the functional groups incorporated in the RAFT agent (i.e., Z- and R-groups, **Figure 2a**). In their work, trithiocarbonate compounds showed better oxidation stability compared to dithioester compounds, as trithiocarbonates have strong electron-donating moieties as a Z-group. Since the radical-induced oxidation and photosensitized oxidation are mechanistically similar, we decided to change CTA from CPADB to 4-cyano-4-[(dodecylsulfanylthiocarbonyl)sulfanyl]pentanoic acid (CDTPA). Fortunately, the triplet energy ( $E_{00}(T1) = 1.64$  eV; as obtained by TD-DFT, **Figure 16**) and the reduction potential ( $E_{red}^0 = -1.07$  V; **Figure 15**) of CDTPA are well matched with those of 4DP-IPN.

The polymerization of MMA was first performed in the presence of 4DP-IPN (5 ppm) and CDTPA under Ar atmosphere using a 3 W blue LED (2.5 mW/cm<sup>2</sup>). Interestingly, this polymerization gave a fairly high conversion of 64% in only 3 h and showed a very poor control of polymerization exemplified by a dispersity ( $\bar{D}$ ) value of 1.92 and an initiator efficiency ( $I^*$ ) of 0.90. In the resulting polymers, the characteristic signal of trithiocarbonate functionality at 3.24 ppm are not seen in <sup>1</sup>H-NMR, confirming that the trithiocarbonate groups at chain ends were decomposed during the polymerization, and thus the polymerization was not controlled at all (**Figure 25**).

To prevent the decomposition of trithiocarbonate functionality, we then performed the same polymerization under a 3 W green LED having weaker light intensity (ca. 0.5 mW/cm<sup>2</sup>). As shown in **Figure 26a**, entry 1, changing the light source allowed for a high conversion of 80% with a good control ( $\bar{D} = 1.20$  and  $I^* = 0.99$ ). Further, the trithiocarbonate functionality was also clearly seen in <sup>1</sup>H-NMR (**Figure 26b**) without any signature of side products, which demonstrates the high-endgroup fidelities. Here, considerably high conversion was achieved in only 6 h, which is much shorter than the polymerization time of the polymerizations using CPADB (62% conversion in 18 h). This is ascribed to a rate-retardation effect commonly found in the dithiobenzoate-based RAFT polymerization of MMA, although the origin of the phenomenon remains under debate;<sup>55,56</sup> in fact, commonly, the rate-retardation effect using CDTPA is significantly lower than that in the dithiobenzoate-based RAFT polymerization.<sup>57,58</sup>

Polymerization using 4DP-IPN (5 ppm) in the presence of CDTPA under air gave an excellent control ( $\bar{D} = 1.26$  and  $I^* = 0.88$ ) with high conversions of 77% (**Figure 26a**); here, the reaction was performed through our general procedure under air, but with a weak 3 W green LED light. We could not observe any signals of end-group decompositions originating from photo-oxidation and so on, which clearly demonstrates the high-end-group fidelities (**Figure 26b**). Chain extension experiment further confirms that polymers can be prepared in a controlled manner even under air (**Figure 27**).

**a**

Entry <sup>a</sup>	PC	Atmosphere	[M]:[I]:[PC]	$\alpha$ (%)	$M_{n,theo}$ (Da)	$M_{n,exp}$ (Da)	$\bar{D}$	$I^*$	Reaction time (h)
1	4DP-IPN	Ar	200:1:0.001	32	6700	9000	1.38	0.74	1
2	4DP-IPN	Ar	200:1:0.001	61	12400	14000	1.77	0.89	2
3	4DP-IPN	Ar	200:1:0.001	64	13100	14500	1.92	0.90	3

a. The reactions were performed at room temperature under a 3 W blue LED (455 nm, ca. 2.5 mW/cm<sup>2</sup>). CDTPA was used as a CTA.

**b**

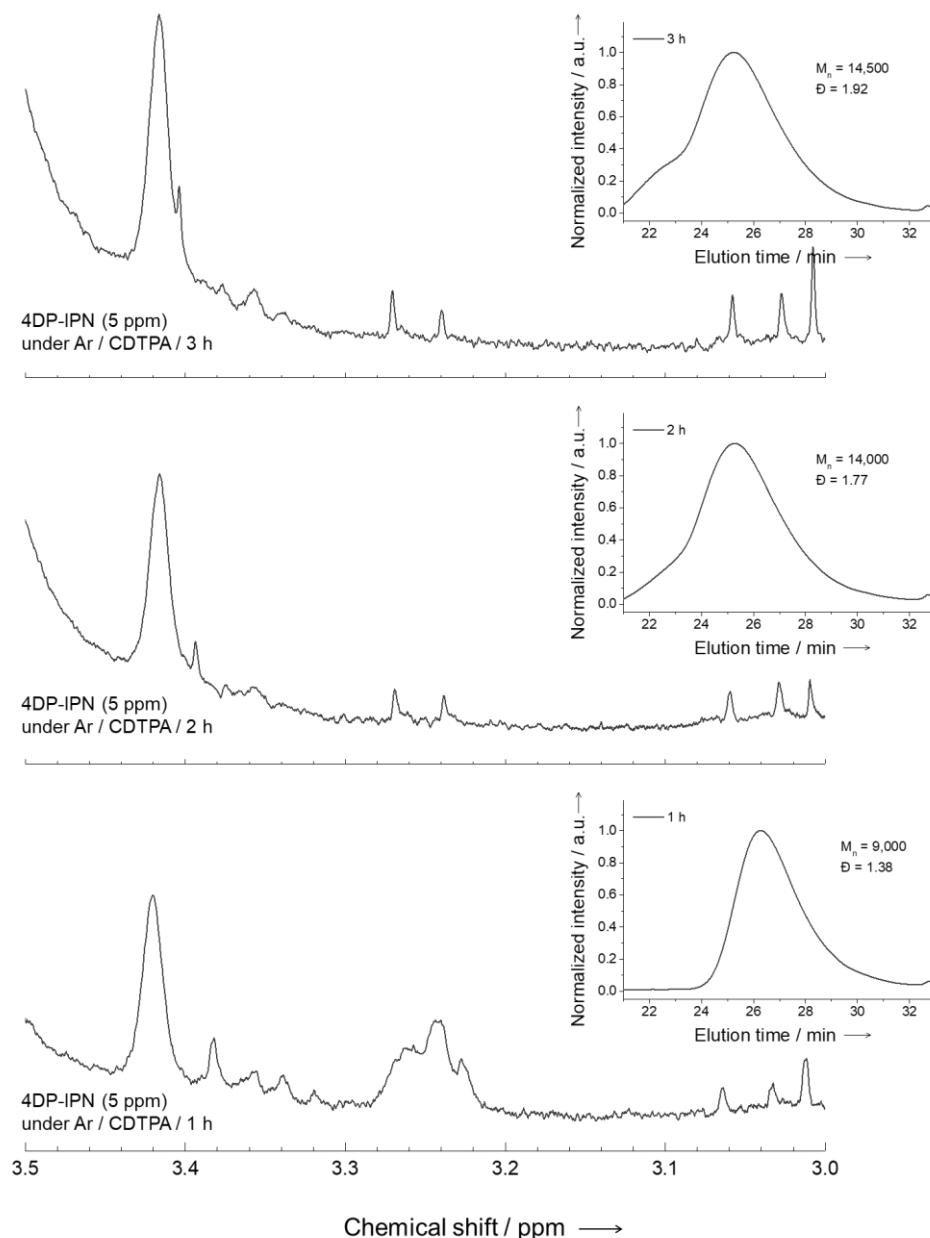


**Figure 25.** (a) Results of PET-RAFT polymerization of MMA in the presence of CDTPA using 4DP-IPN of 5 ppm under argon. All polymerizations were performed at room temperature under a 3 W blue LED (455 nm, ca. 2.5 mW/cm<sup>2</sup>). (b) <sup>1</sup>H-NMR spectra and GPC traces of the reaction mixtures are obtained after PET-RAFT polymerizations of MMA.

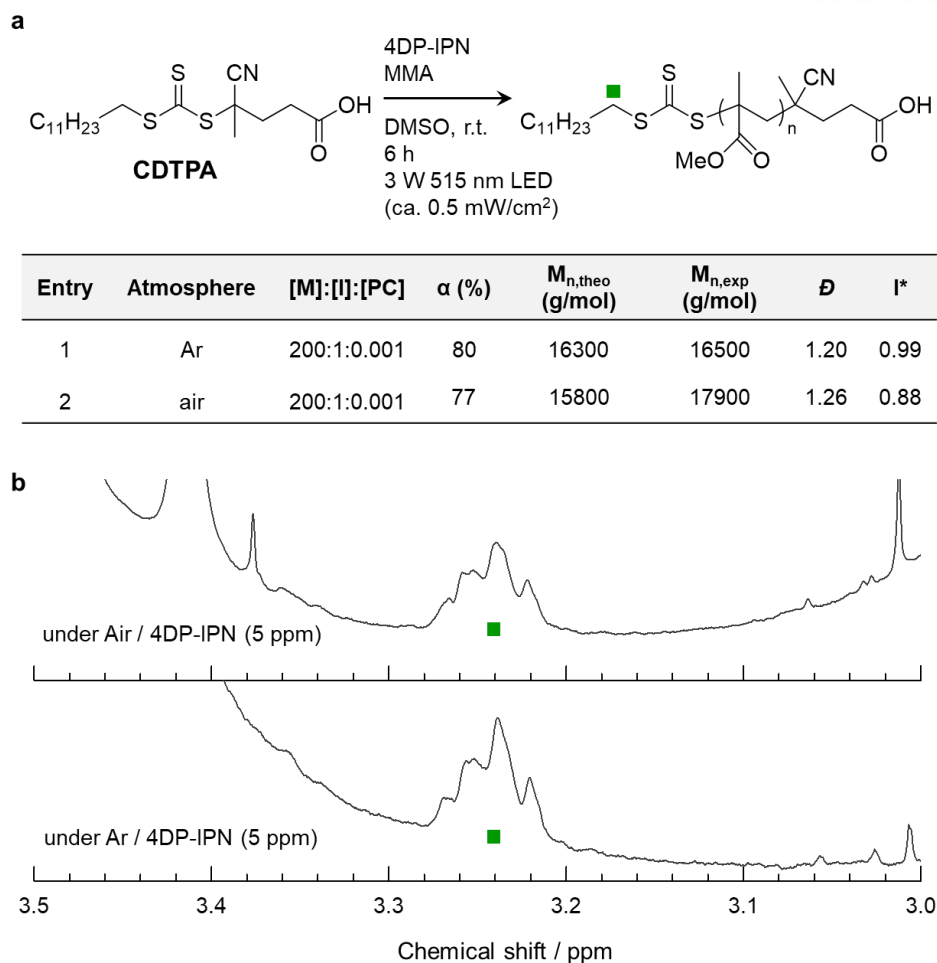


**Figure 26.** (a) Results of PET-RAFT polymerizations of MMA in the presence of CDTPA using 4DP-IPN under Ar and/or air. All polymerizations were performed at room temperature under a 3 W green LED (515 nm, ca. 0.5 mW/cm<sup>2</sup>). Polymerizations under Ar were carried out in a sealed 20 mL vial with a total liquid volume of 2 mL (1:1, v/v of MMA/DMSO). Polymerizations under air were conducted in a sealed 4 mL vial with a total liquid volume of 3 mL. (b) <sup>1</sup>H-NMR spectra of the reaction mixtures obtained after PET-RAFT polymerizations of 6 h without purifications under air (up) and Ar (bottom) in the presence of CDTPA and MMA with/without 4DP-IPN of 5 ppm (Reprinted with permission from Reference 1. Copyright 2019. American Chemical Society.).

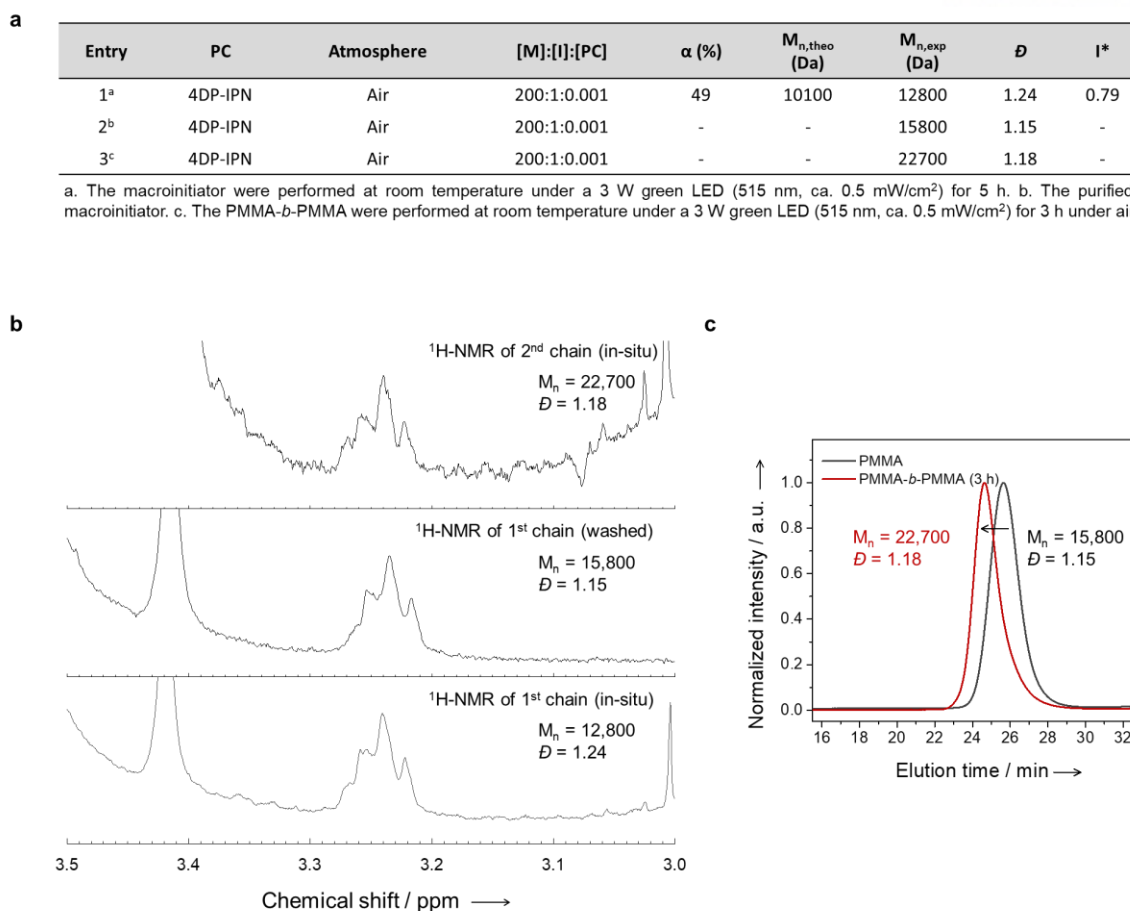


**Figure 27.** (a) Chain extensions of PMMA in the presence of air using CDTPA and 4DP-IPN of 5 ppm. (b) <sup>1</sup>H-NMR spectra of washed (middle) and in-situ (bottom) 1<sup>st</sup> chain and in-situ (top) 2<sup>nd</sup> chain under air. (c) GPC traces (right) of PMMA (black) and diblock of PMMA-*b*-PMMA (red) under air.

## 4.5 Experimental validation of the outstanding performance of 4DP-IPN

We finally investigated the photophysical and electrochemical properties of 4DP-IPN to understand its excellent catalyst performance. Fairly strong visible-light absorption; proper  $E_{\text{ox}}^0$  of 1.30 V,  $E_{\text{ox}}^*(\text{T1})$  of  $-1.17$  V, and  $E_{00}(\text{T1})$  of 2.29 eV; and a highly stable radical cation were observed (**Figure 28a,b**).

Time-resolved photoluminescence (PL) and transient absorption (TA) studies were then conducted to quantify the rate constants in **Figure 28c**, **29–35** and **Table 7**. While PL experiments at room temperature are sensitive only to the emission from  $S_1$  states (phosphorescence being suppressed), TA allows tracing the concentrations of both  $S_1$  and  $T_1$  states in a single experiment (**Figure 35**). Therefore, it is useful to perform both experiments; all details are given in the supporting information. Both experiments yield similar values, for the intersystem crossing (ISC) rate constant  $k_{\text{ISC}} = 2.5 (2.1) \times 10^8 \text{ s}^{-1}$  for PL (TA) as well as for the triplet yield  $\Phi_{\text{ISC}} = 0.82 (0.77)$  for PL (TA). Both PL and TA agree to the finding that at room temperature, direct relaxation of  $T_1$  to the ground state (via  $k_{\text{PH}}$  and  $k_{\text{nr}}$ ) are negligible; the only available relaxation channel is through the  $S_1/T_1$  equilibrium leading to thermally activated delayed fluorescence (TADF; **Figures 28c** and **29–32**); in fact, the observed  $100 \mu\text{s}$  TADF lifetime yields an offset between  $S_1$  and  $T_1$  of 0.19 eV, in good agreement with the experiment and the TD-DFT results (**Figure 28c**). The TD-DFT results further suggest that the high ISC efficiency is due to the well-balanced intramolecular CT character of  $S_1$  and the low lying  $T_n$  states. In  $S_1$ , intramolecular CT gives sufficient oscillator strength  $f$  to promote fluorescence ( $f = 0.08$ ; **Figure 28c**). At the same time,  $T_{2,3}$  are energetically close to  $S_1$  and exhibit largely different intramolecular CT character compared to  $S_1$  (**Figure 28c**); this promotes efficient spin-orbit coupling (SOC). In fact, this is considered as a central design element of the multibranched 4DP-IPN, allowing for multiple intramolecular CT configurations, combined with good light absorption and matching redox properties.

The results further highlight the potential of the novel material. High triplet yields explain good light sensitivity while long triplet lifetimes explain the efficiency toward polymerization at just 5 ppm. The absence of a direct decay channel means that the triplet lifetime is entirely controlled by the  $S_1/T_1$  energetic offset; subtle changes in the molecular structure will therefore lead to strong changes of the triplet lifetime. This property should be taken into account when the material is further tuned toward unity triplet yield.

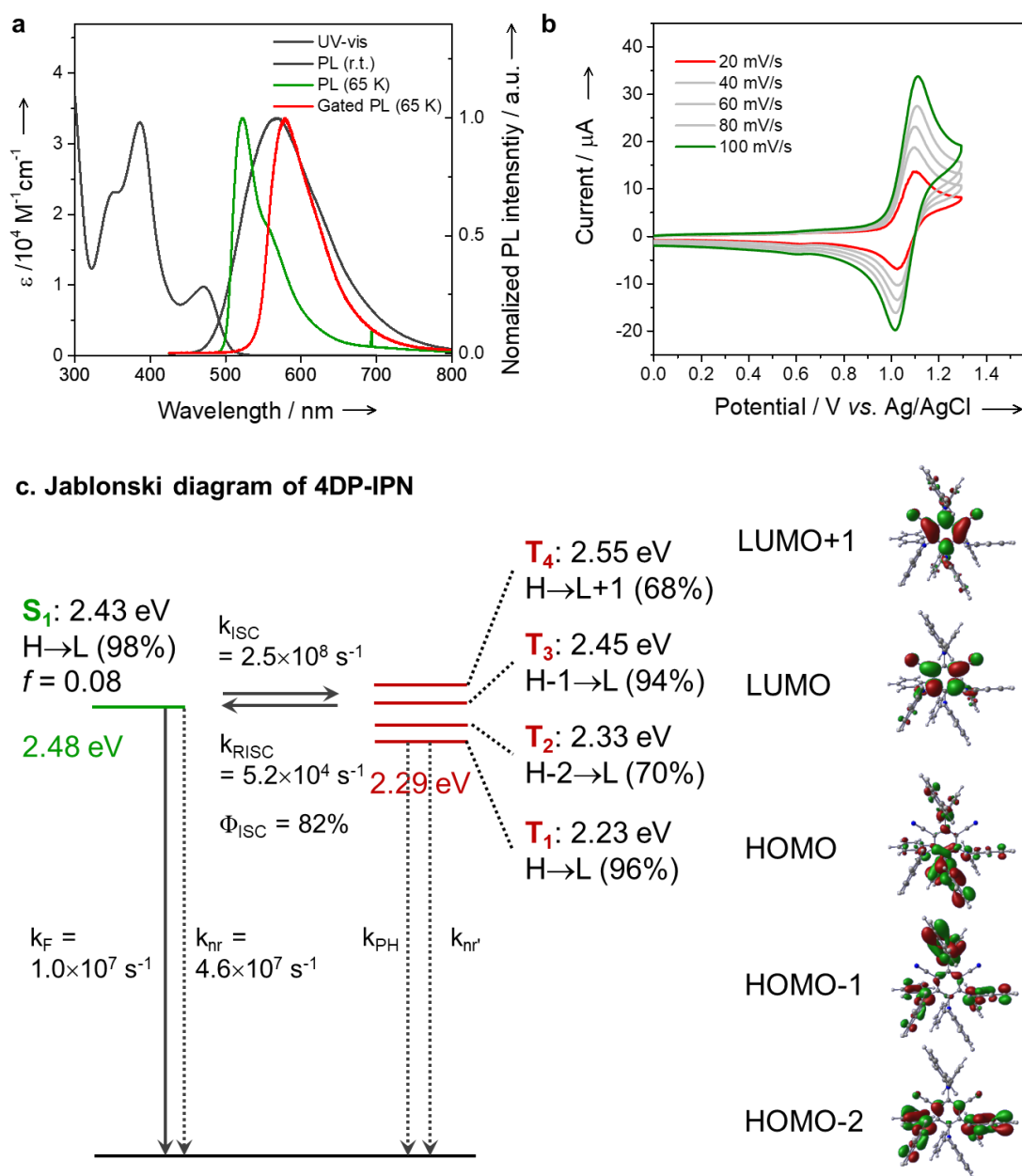


**Figure 28.** Photophysical and electrochemical properties of 4DP-IPN. (a) UV-vis absorption (dark gray line) in DMSO ( $2 \times 10^{-5}$  M) and photoluminescence (PL) at room temperature (dark gray line), gated PL at 68 K (red line), and PL at 68 K (green line) in  $\text{CH}_3\text{CN}$  ( $2 \times 10^{-5}$  M). (b) Cyclic voltammetry of 2.0 mM 4DP-IPN in  $\text{CH}_3\text{CN}$  containing 0.1 M  $\text{nBu}_4\text{NPF}_6$  on a glassy carbon working electrode at variable scan rates from 20 to 100 mV/s. (c) Term diagrams of 4DP-IPN as obtained from the experiments (in  $\text{CH}_3\text{CN}$ ) and by TD-DFT (in DMF) (*Reprinted with permission from Reference 1. Copyright 2019. American Chemical Society.*).

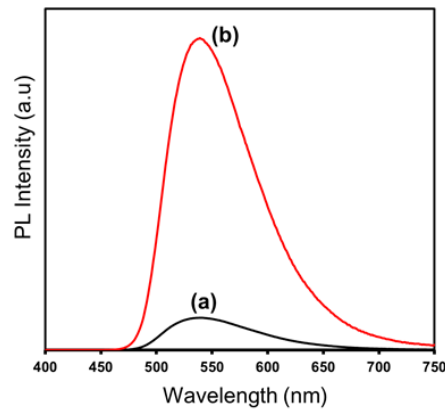


**Figure 29.** PL emission spectra of 4DP-IPN in CH<sub>3</sub>CN at r.t. (a) unpurged (b) after purging 10 min with dry N<sub>2</sub> gas,  $\lambda_{\text{exc}} = 387$  nm.

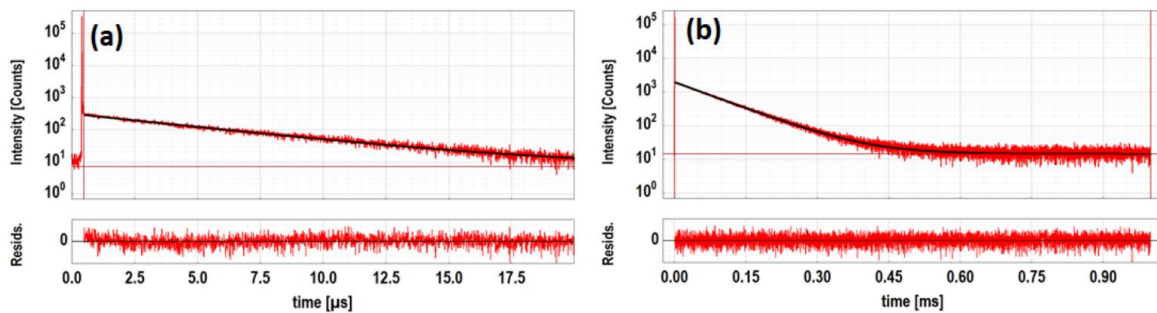


**Figure 30.** PL decays of 4DP-IPN in DMSO at RT,  $\lambda_{\text{exc}} = 405$  nm,  $\lambda_{\text{det}} = 540$  nm; experiment (red), mono-exponential fits (black). (a) unpurged,  $\nu_{\text{rep}} = 50$  kHz,  $\tau = 5.1$   $\mu\text{s}$ . (b) after purging (10 min, dry N<sub>2</sub> gas),  $\nu_{\text{rep}} = 1$  kHz,  $\tau = 82.8$   $\mu\text{s}$ .

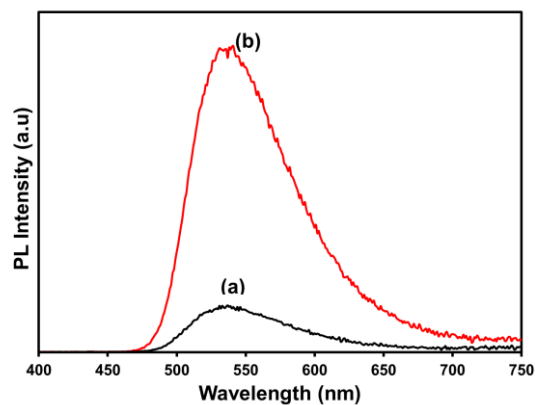


**Figure 31.** PL emission spectra of 4DP-IPN in DMSO at r.t. (a) unpurged (b) after 10 min purging with dry N<sub>2</sub> gas,  $\lambda_{\text{exc}} = 387$  nm.



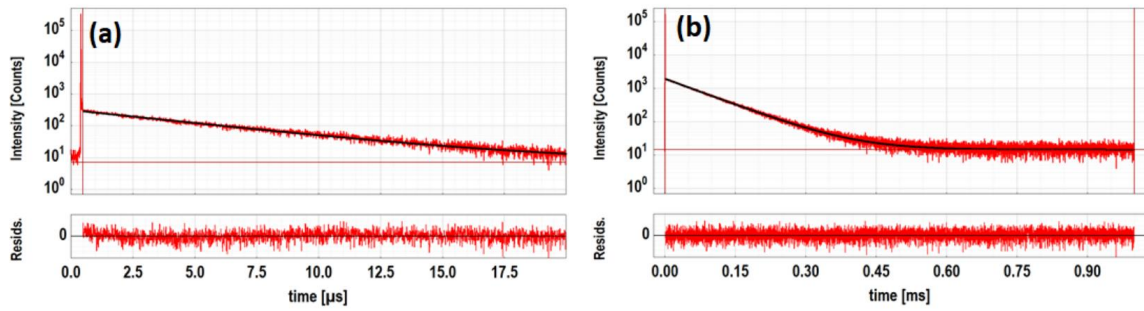


**Figure 32.** PL decays of 4DP-IPN in DMSO at RT,  $\lambda_{exc} = 405$  nm,  $\lambda_{det} = 540$  nm; experiment (red), mono-exponential fits (black). (a) unpurged,  $\nu_{rep}=50$  kHz,  $\tau = 5.1$   $\mu$ s. (b) after purging (10 min, dry N<sub>2</sub> gas),  $\nu_{rep}=1$  kHz,  $\tau = 82.8$   $\mu$ s

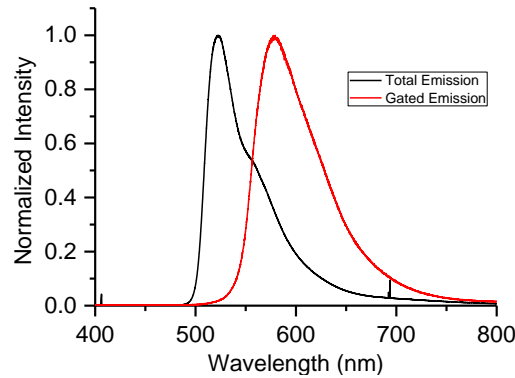


**Figure 33.** Emission under continuous wave excitation and gated emission of 4DP-IPN in CH<sub>3</sub>CN at 65K.

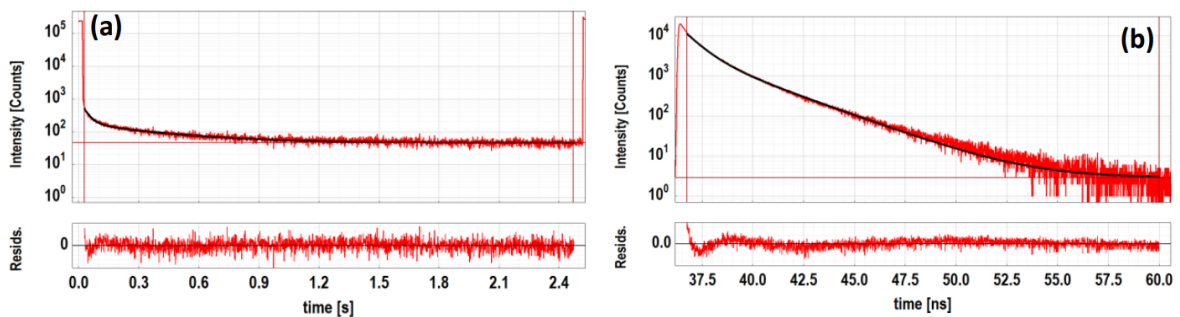


**Figure 34.** PL Decays of 4DP-IPN in CH<sub>3</sub>CN at 65K, experiment (red), bi-exponential fits (black). (a) Phosphorescence decay,  $\lambda_{exc} = 405$  nm,  $\lambda_{det} = 560$  nm,  $\nu_{rep}=0.33$  Hz.  $\tau_1 = 31$  ms ( $A_1=3.0 \cdot 10^{-1}$ , 17%),  $\tau_2 = 380$  ms ( $A_2=7.1 \cdot 10^{-1}$ , 83%). (b) Fluorescence decay,  $\lambda_{exc} = 405$  nm,  $\lambda_{det} = 525$  nm,  $\nu_{rep}= 2.5$  MHz.  $\tau_1 = 2.4$  ns ( $A_1= 2.9 \cdot 10^{-1}$ , 56%),  $\tau_2=0.8$  ns ( $A_2= 7.1 \cdot 10^{-1}$ , 44%).

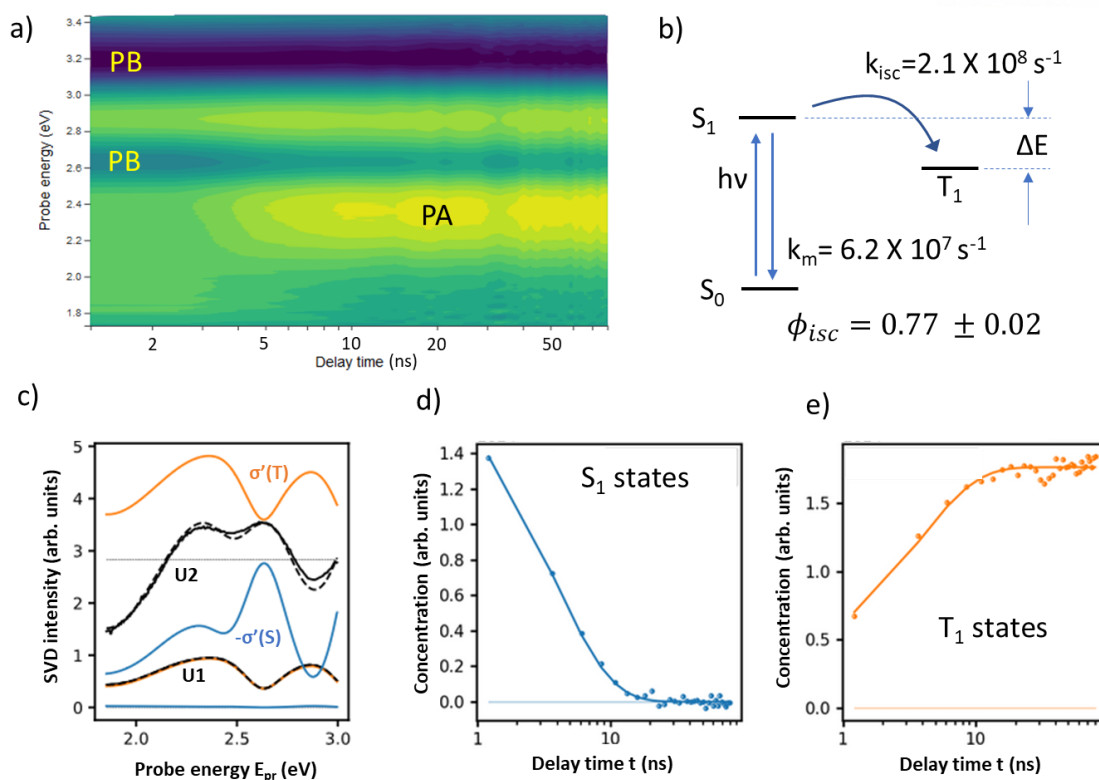


**Figure 35.** Transient absorption (TA) experiment of 4DP-IPN was performed in CH<sub>3</sub>CN at r.t. (a) TA spectrum in the nanosecond temporal range, after pumping with 300 ps monochromatic pump pulses at 355 nm with 2  $\mu$ J pulse energy and a repetition rate of 500 Hz. The false color scale denotes green as zero signal, yellow as positive transient absorption (photo-induced absorption, PA) and blue as negative transient absorption (transient photobleach, PB). (b) Kinetic model for the simulation of the TA dynamics. Note that the slow processes from scheme 1 ( $k_{\text{risc}}$  and  $k_{\text{T0}}$ ) have been omitted because they cannot be obtained on a 100 ns time scale; note also that  $k_{\text{m}}=k_{\text{F}}+k_{\text{nr}}$ . Without measuring the PLQY, one cannot distinguish these processes leading to the same PA and PB dynamics. However, even without knowledge of PLQY, one can still get the ISC yield, defined as  $\Phi_{\text{isc}} = k_{\text{isc}}/(k_{\text{m}} + k_{\text{isc}})$ , directly from fitting the TA spectrum in panel (a). (c) t-SVD (eq. S13) of panel (a) (black solid lines in panel (c)), and reproduction (black dashed lines) by a weighted superposition of the characteristic spectra for excited singlet and triplet states (blue and orange lines, defined acc. to eq. S14). (d) and (e) resulting dynamics of excited singlet and triplet states, according to eq. S12 (blue and orange symbols, respectively) and fitted dynamics according to panel b) (blue and orange solid lines, respectively).

**Table 7.** PLQY of 4DP-IPN at r.t. under N<sub>2</sub> purged condition.

solvent	$\Phi_F$
CH <sub>3</sub> CN	0.18
DMSO	0.23

**4.6 UV-Vis and PL spectra, CV curves, and  $^1\text{H-NMR}$  and  $^{13}\text{C-NMR}$  spectra of selected OPCs and GPC traces and  $^1\text{H-NMR}$  spectra of the resulting polymers**

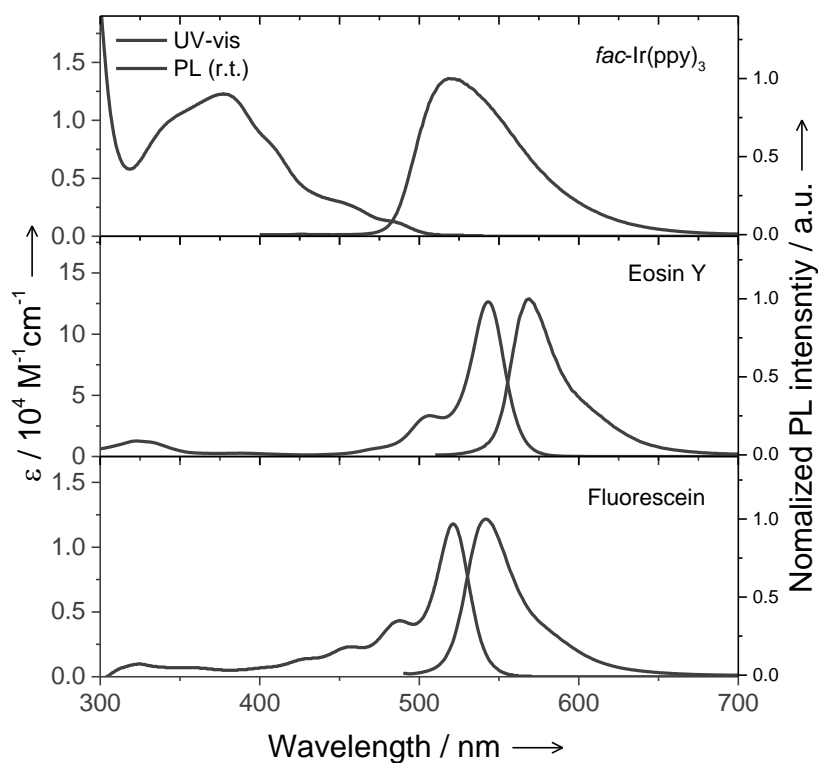


**Figure 36.** UV-Vis and PL spectra of PCs were purchased commercially in DMSO ( $20 \mu\text{M}$ ).

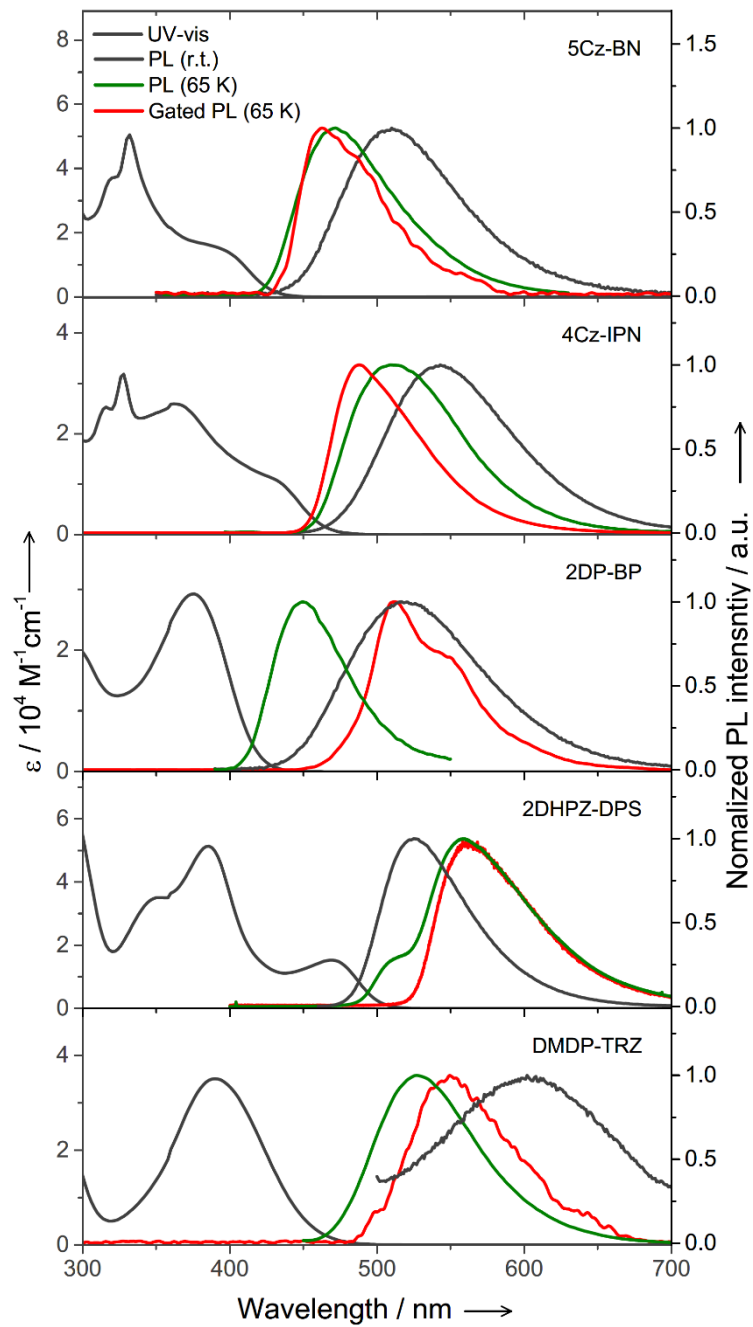


**Figure 37.** UV-Vis and PL spectra of selected OPCs in DMF (20 μM).

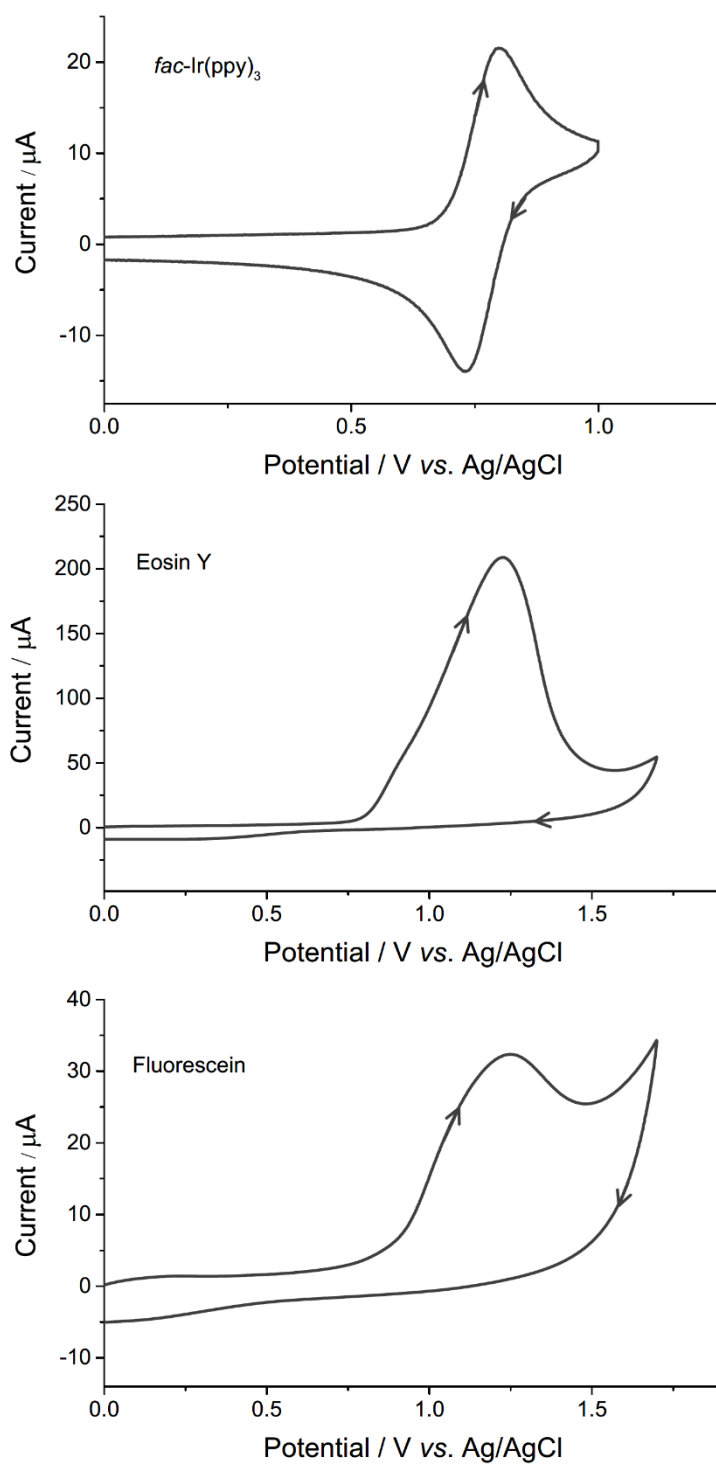


**Figure 38.** CV curves of PCs were purchased commercially in  $\text{CH}_3\text{CN}$  (2 mM). For eosin Y and fluorescein, in  $\text{CH}_3\text{CN}:\text{H}_2\text{O}$  (1:1 v/v) (2 mM).

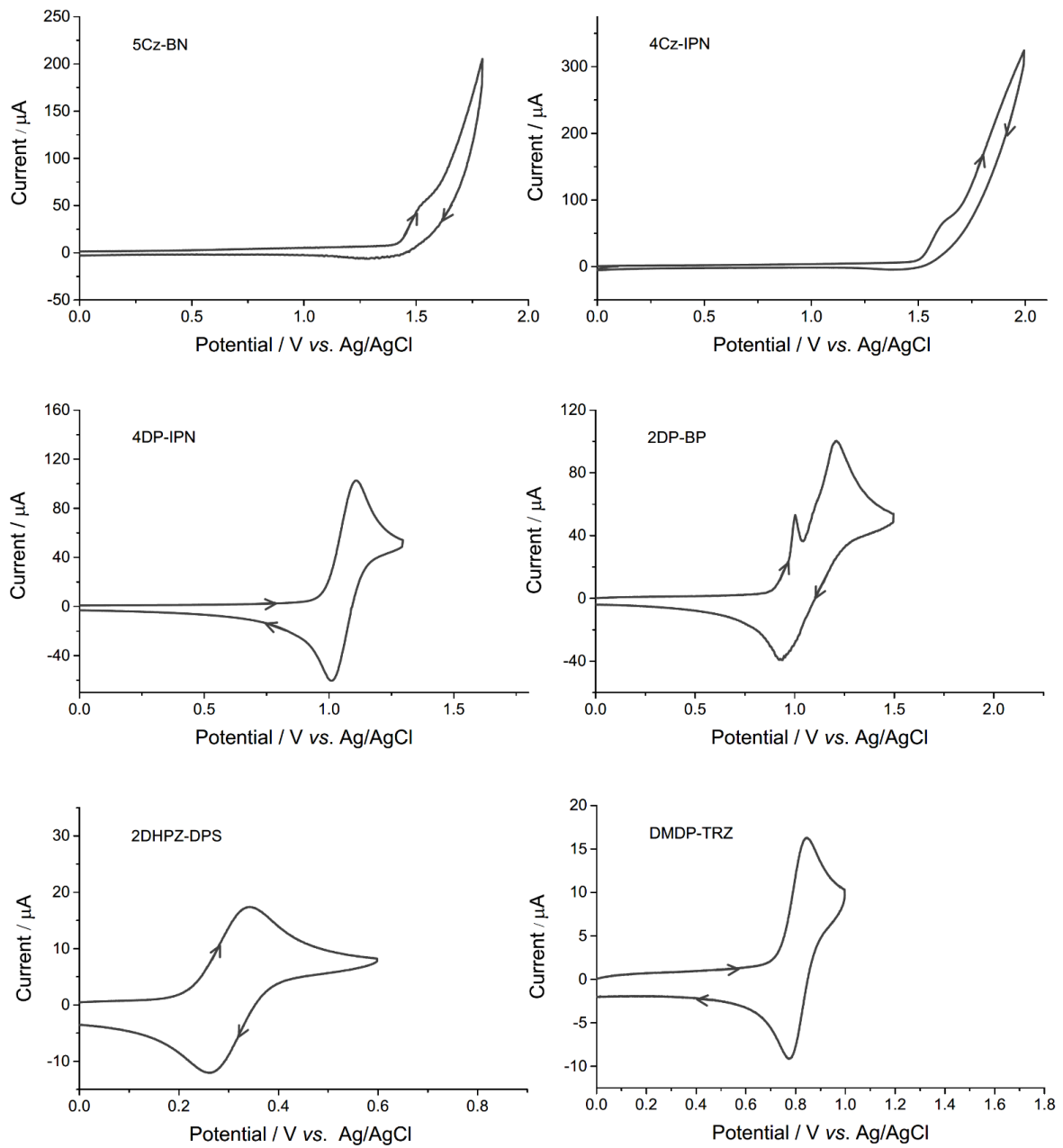


**Figure 39.** CV curves of selected OPCs in CH<sub>3</sub>CN (2 mM).

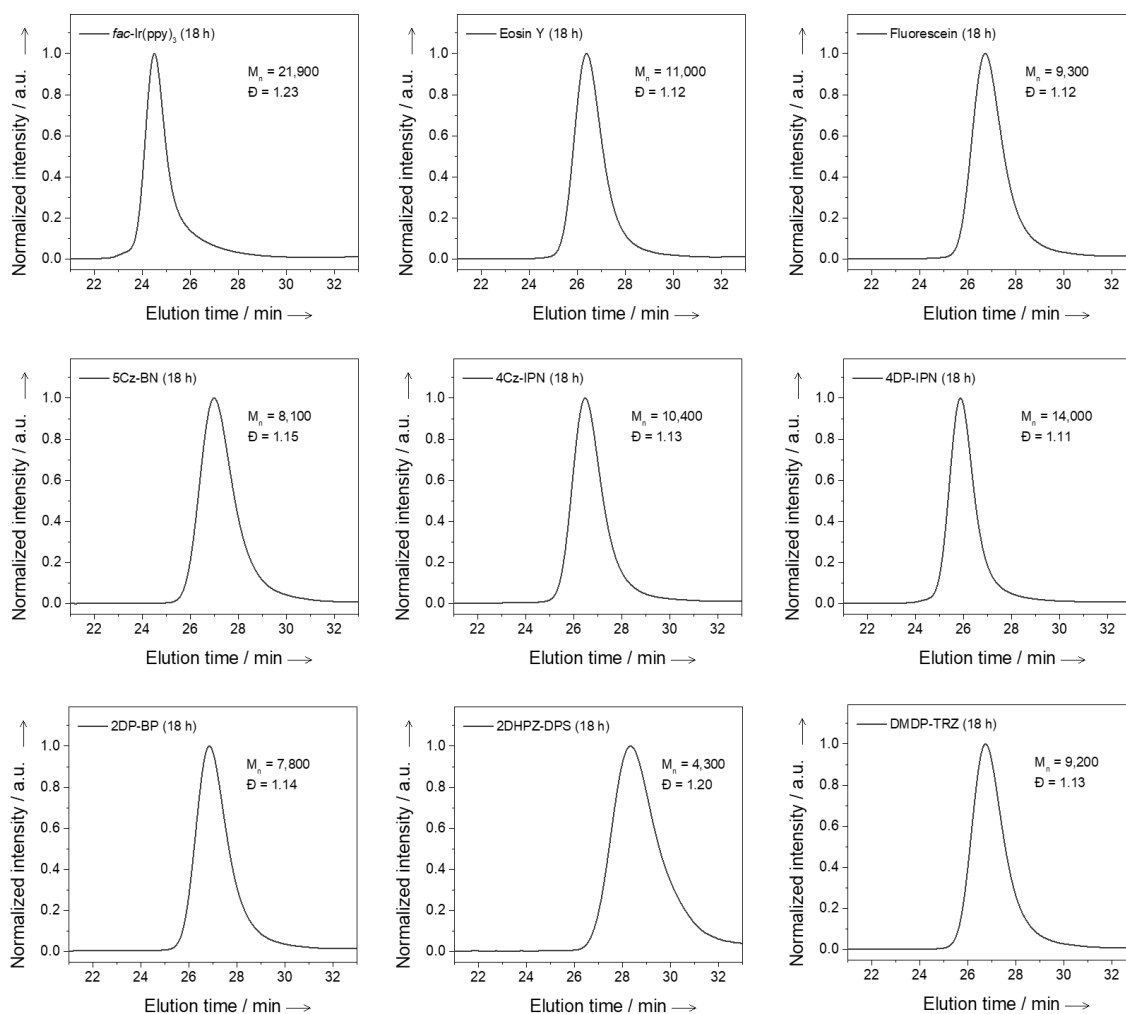


**Figure 40.** GPC traces of PET-RAFT polymerizations of MMA for **Table 2**. Experimental condition: [MMA]:[CPADB]:[Ir(ppy)<sub>3</sub>] = 200:1:0.0002 and [MMA]:[CPADB]:[OPC] = 200:1:0.001 in DMSO under a 3W 455 nm LED at room temperature under argon.

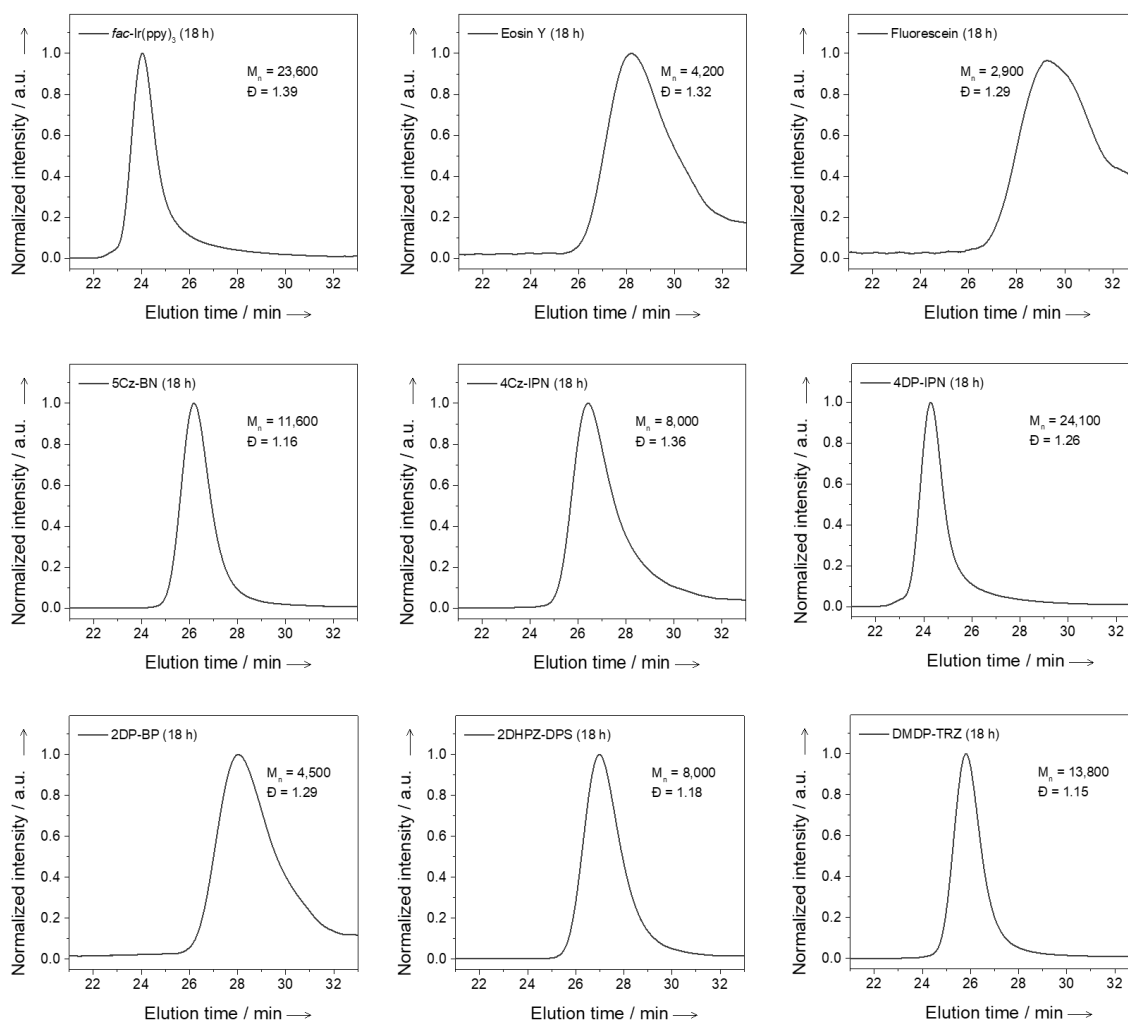


**Figure 41.** GPC traces of PET-RAFT polymerizations of MMA for **Table 2**. Experimental condition: [MMA]:[CPADB]:[Ir(ppy)<sub>3</sub>] = 200:1:0.0002 and [MMA]:[CPADB]:[OPC] = 200:1:0.001 in DMSO under a 3W 455 nm LED at room temperature under air.



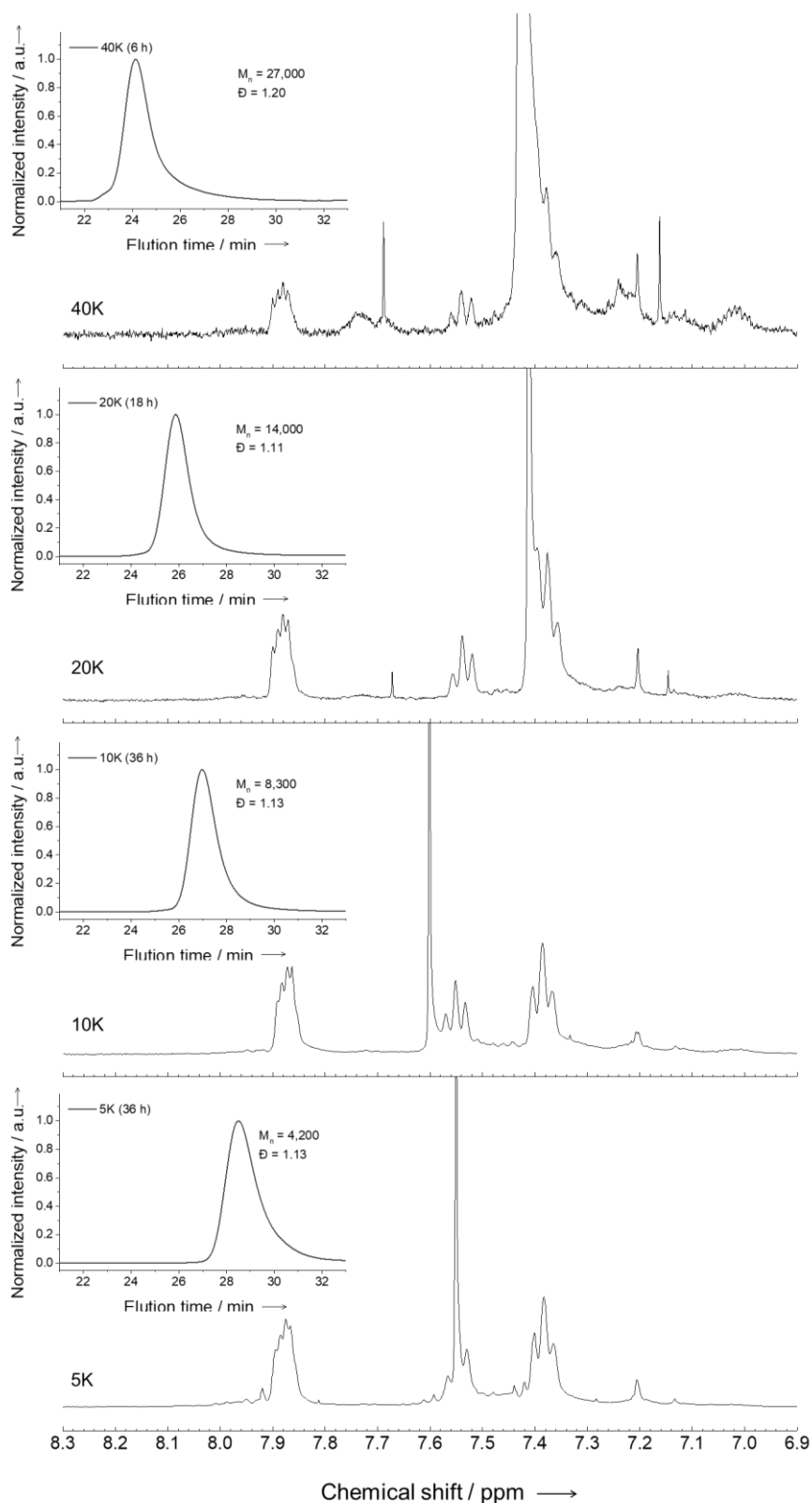


**Figure 42.**  $^1\text{H-NMR}$  spectra and GPC curves of the molecular weight controlled PMMA in the presence of argon using CPADB and 4DP-IPN of 5 ppm.

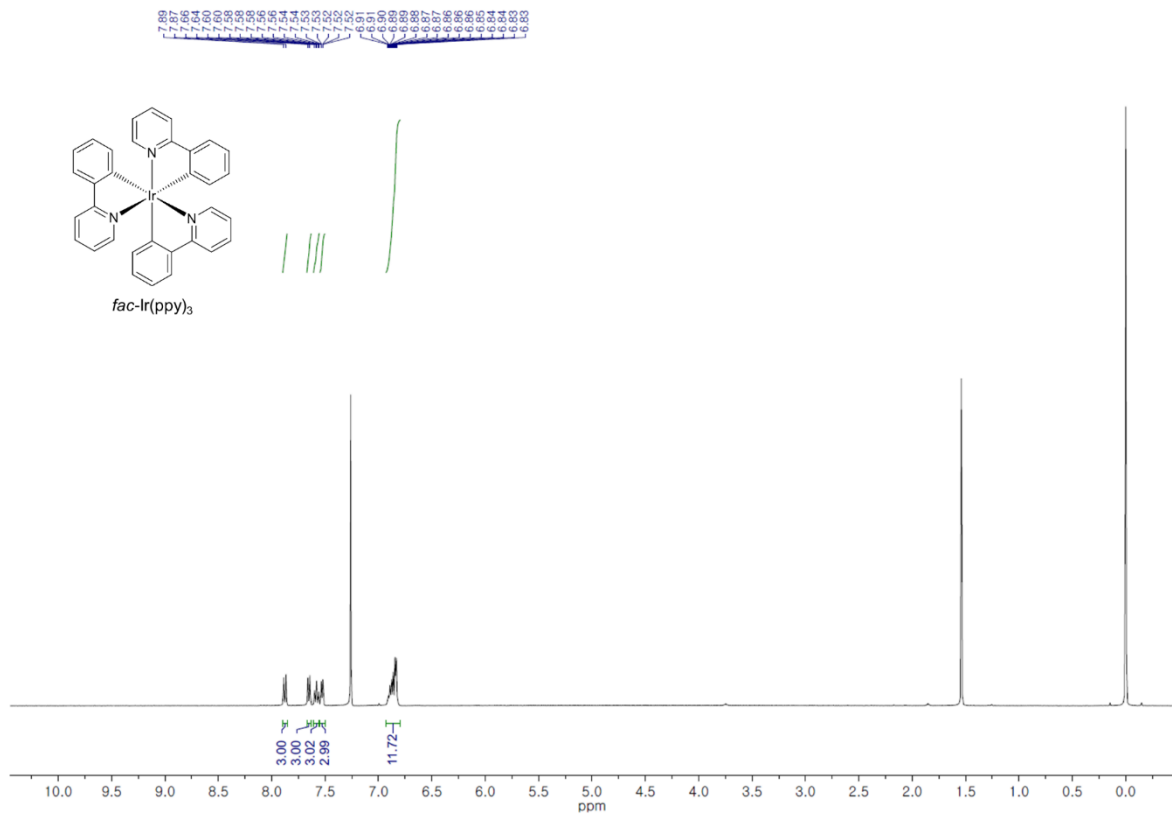


Figure 43.  $^1\text{H-NMR}$  of  $\text{Ir(ppy)}_3$  in  $\text{CDCl}_3$  at r.t..

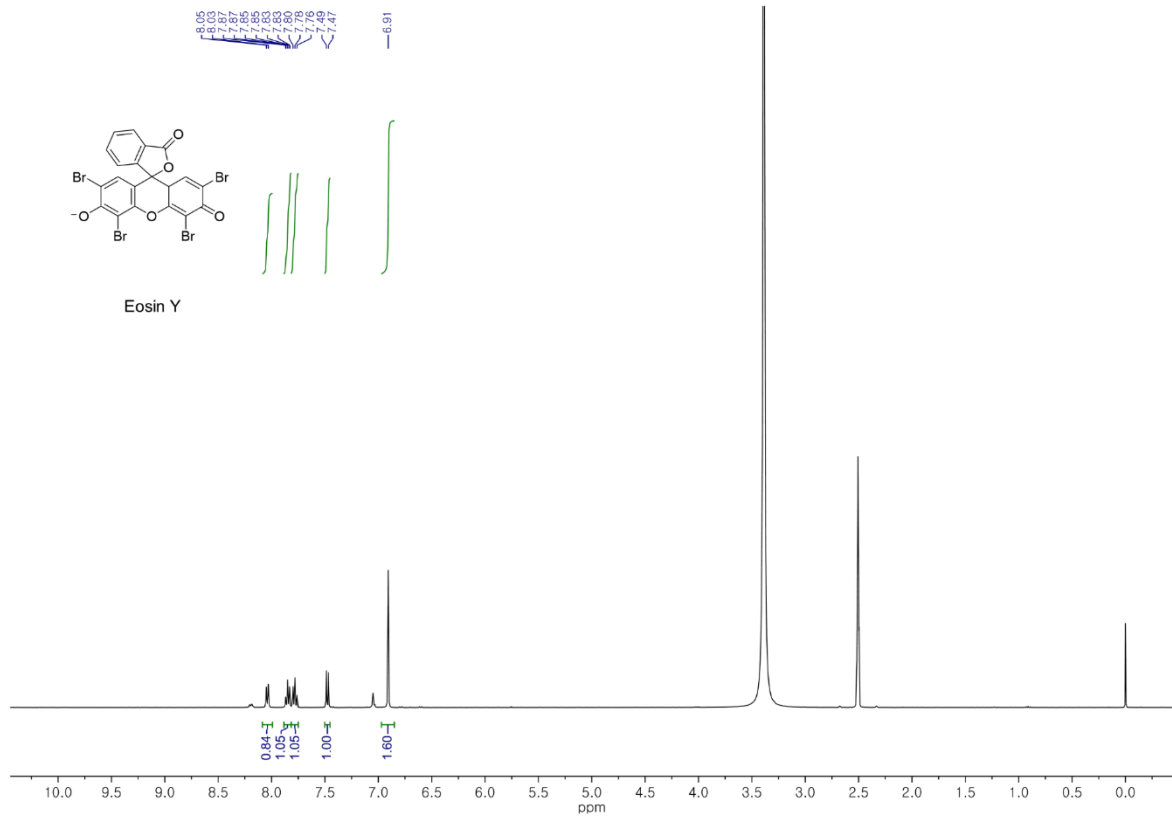


Figure 44.  $^1\text{H-NMR}$  of eosin Y in  $\text{CDCl}_3$  at r.t..

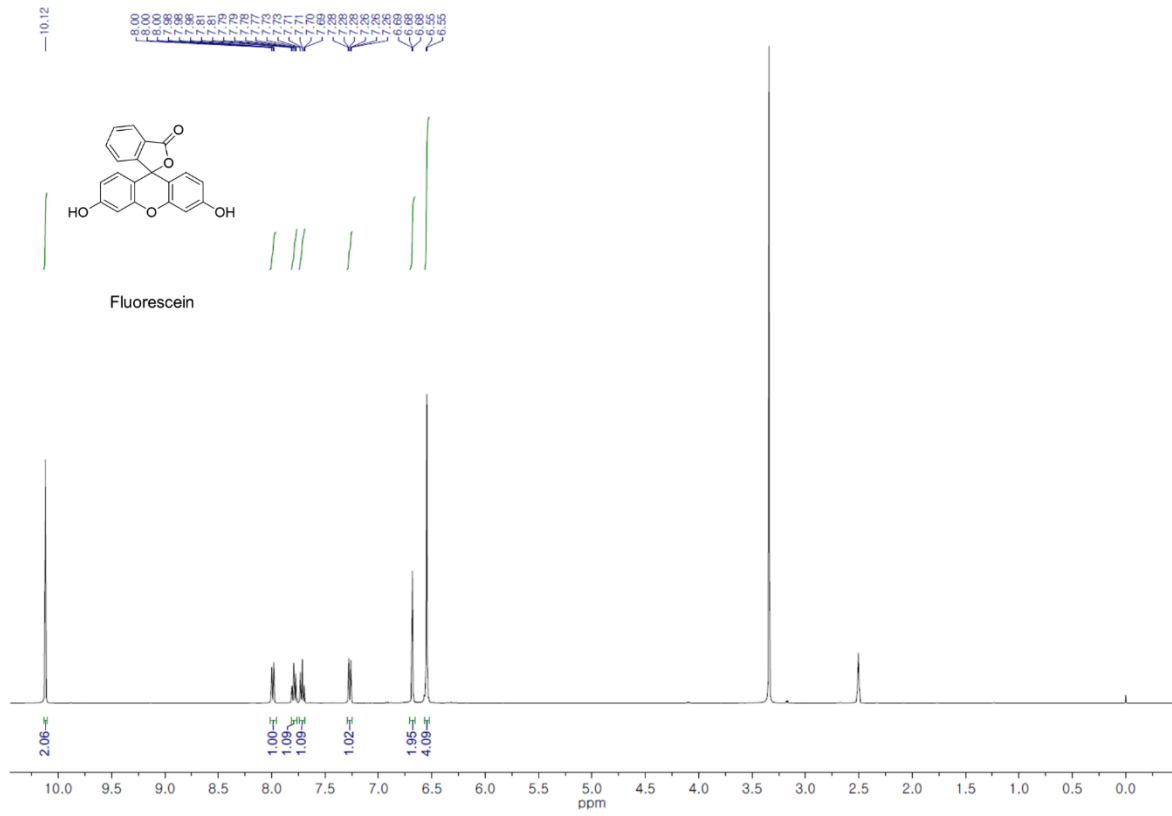


Figure 45. <sup>1</sup>H-NMR of fluorescein in CDCl<sub>3</sub> at r.t..

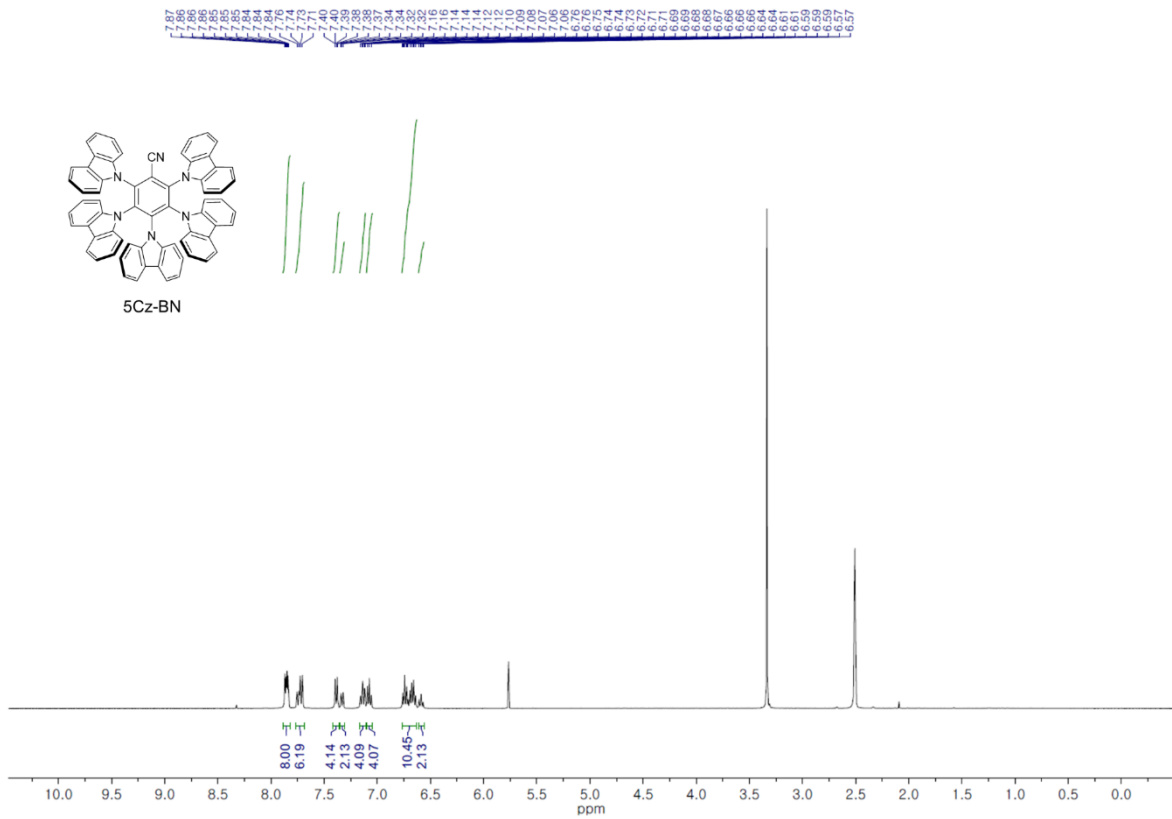


Figure 46. <sup>1</sup>H-NMR of 5Cz-BN in CDCl<sub>3</sub> at r.t..

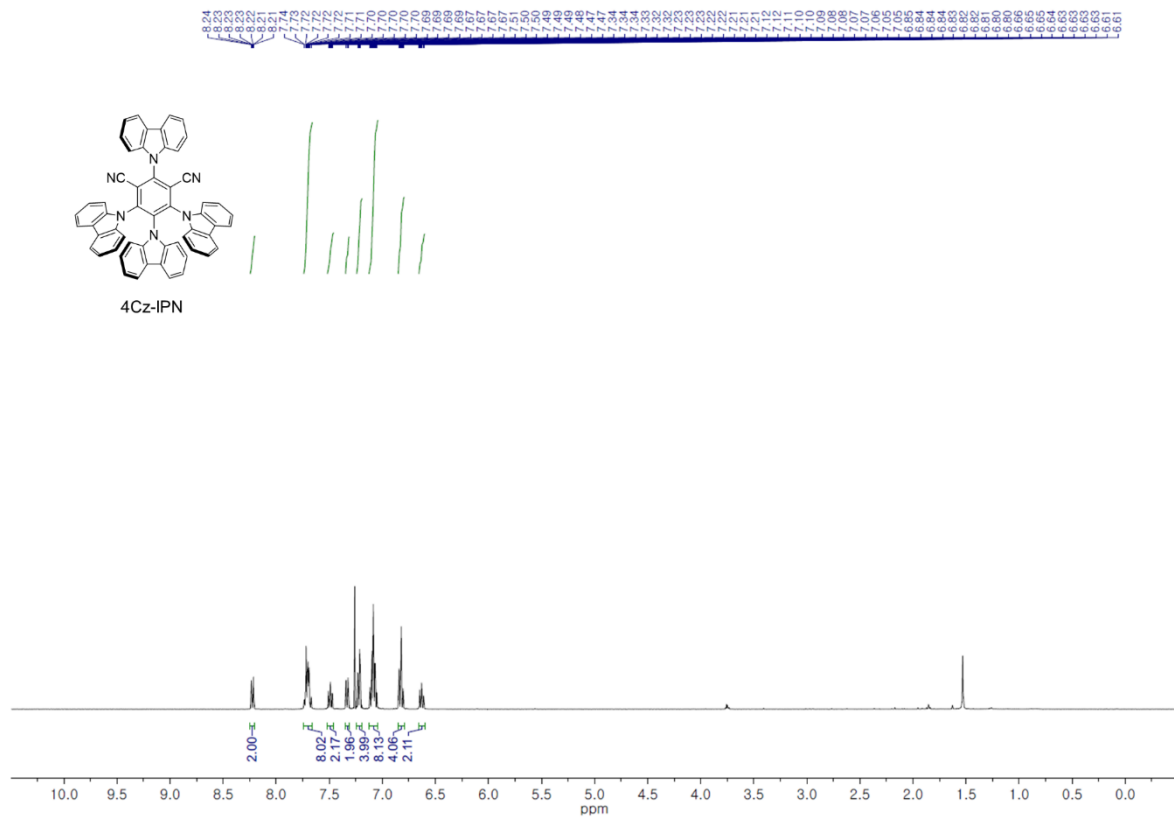


Figure 47. <sup>1</sup>H-NMR of 4Cz-IPN in CDCl<sub>3</sub> at r.t..

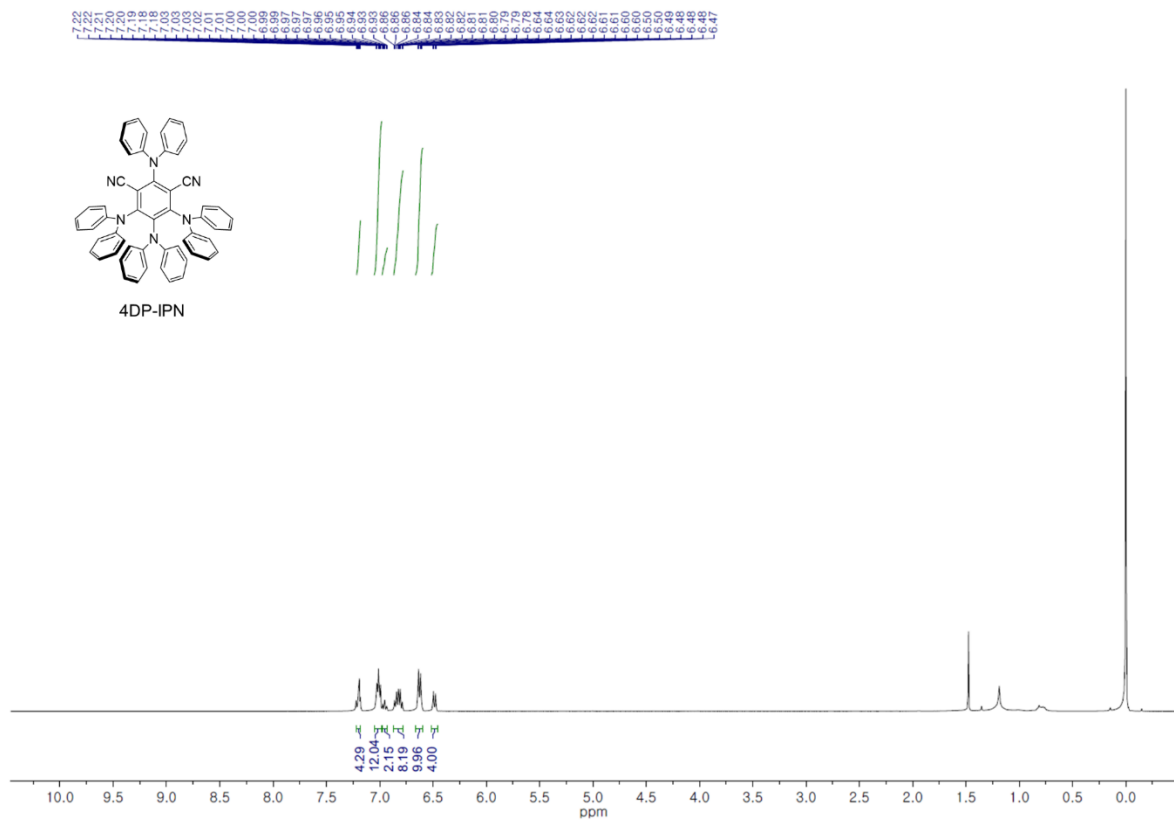
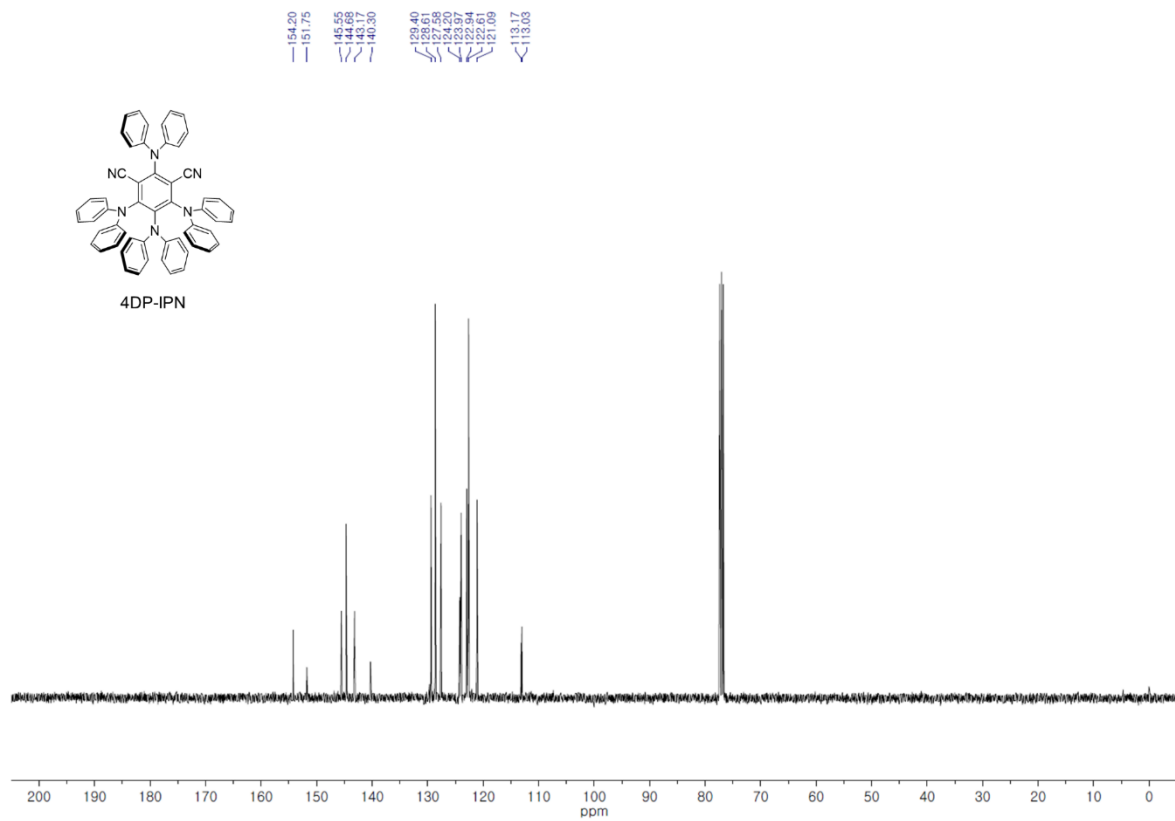
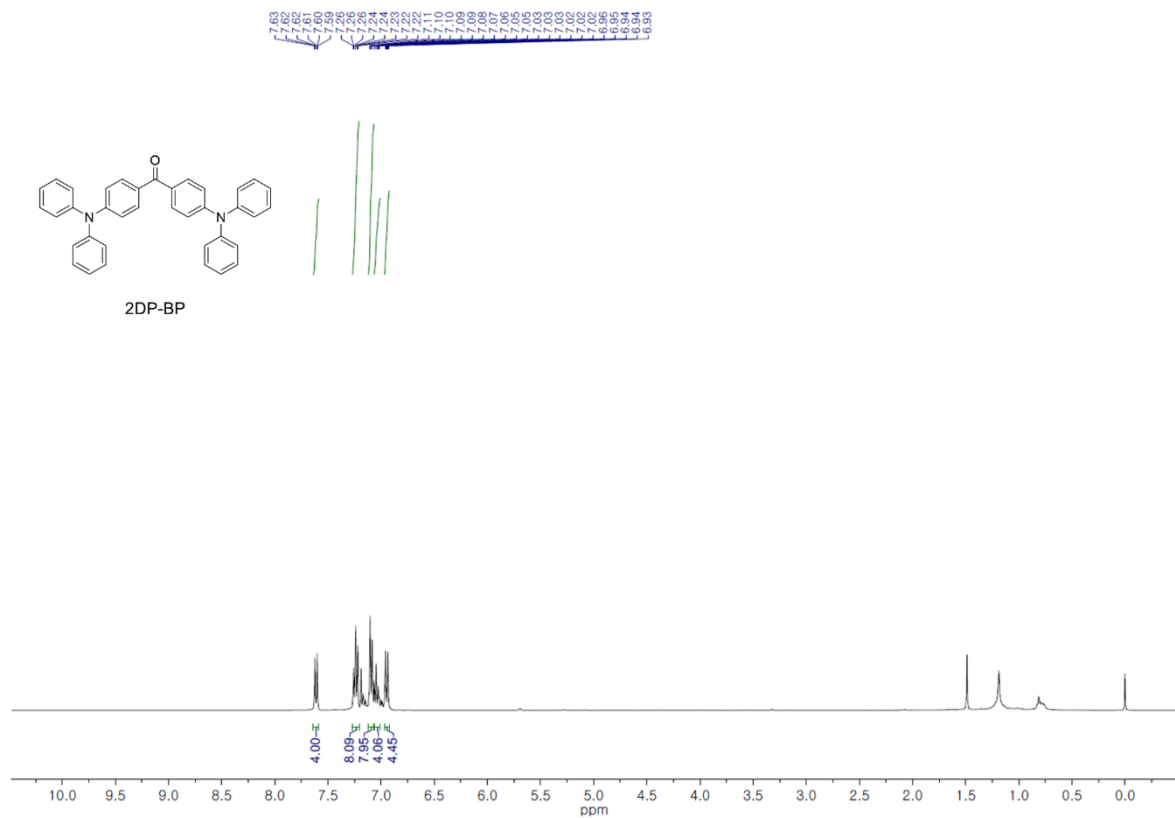


Figure 48. <sup>1</sup>H-NMR of 4DP-IPN in CDCl<sub>3</sub> at r.t..



**Figure 49.** <sup>13</sup>C-NMR of 4DP-IPN in CDCl<sub>3</sub> at r.t..



**Figure 50.** <sup>1</sup>H-NMR of 2DP-BP in CDCl<sub>3</sub> at r.t..

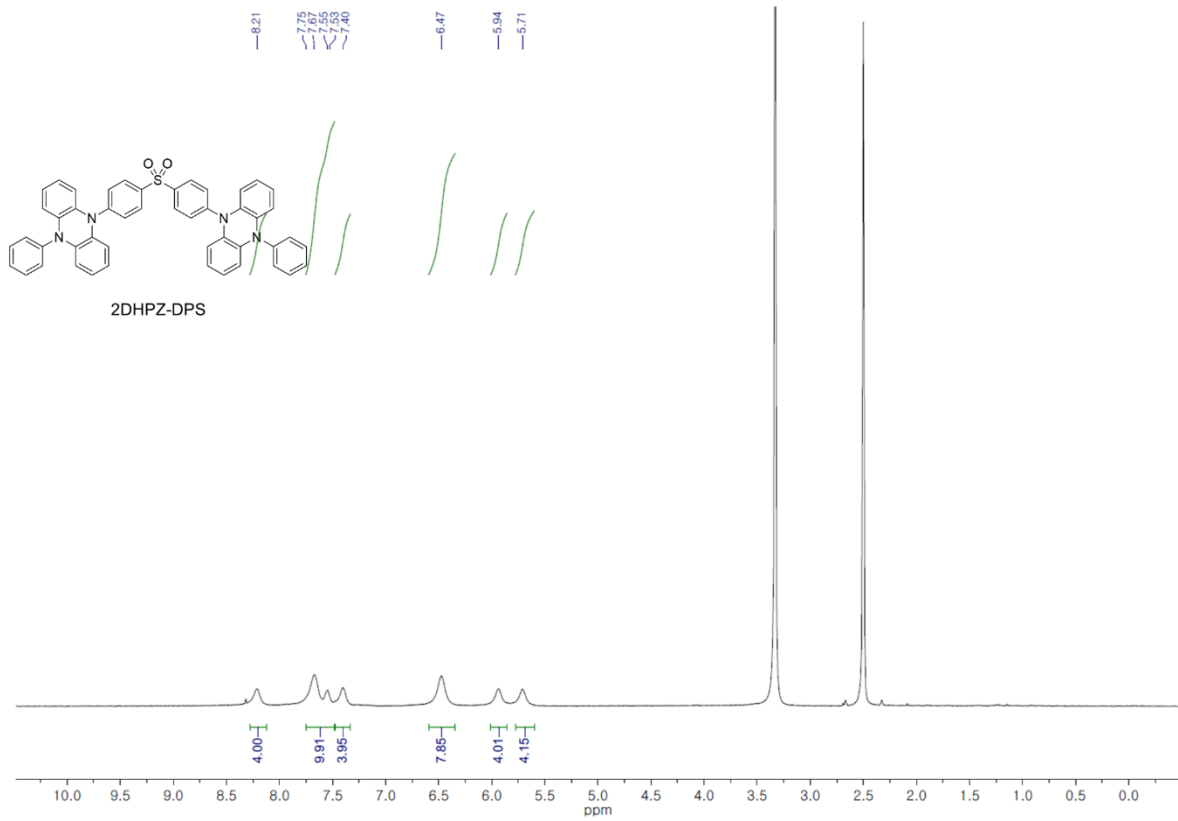


**Figure 51.**  $^1\text{H-NMR}$  of 2DHPZ-DPS in  $\text{CDCl}_3$  at r.t..

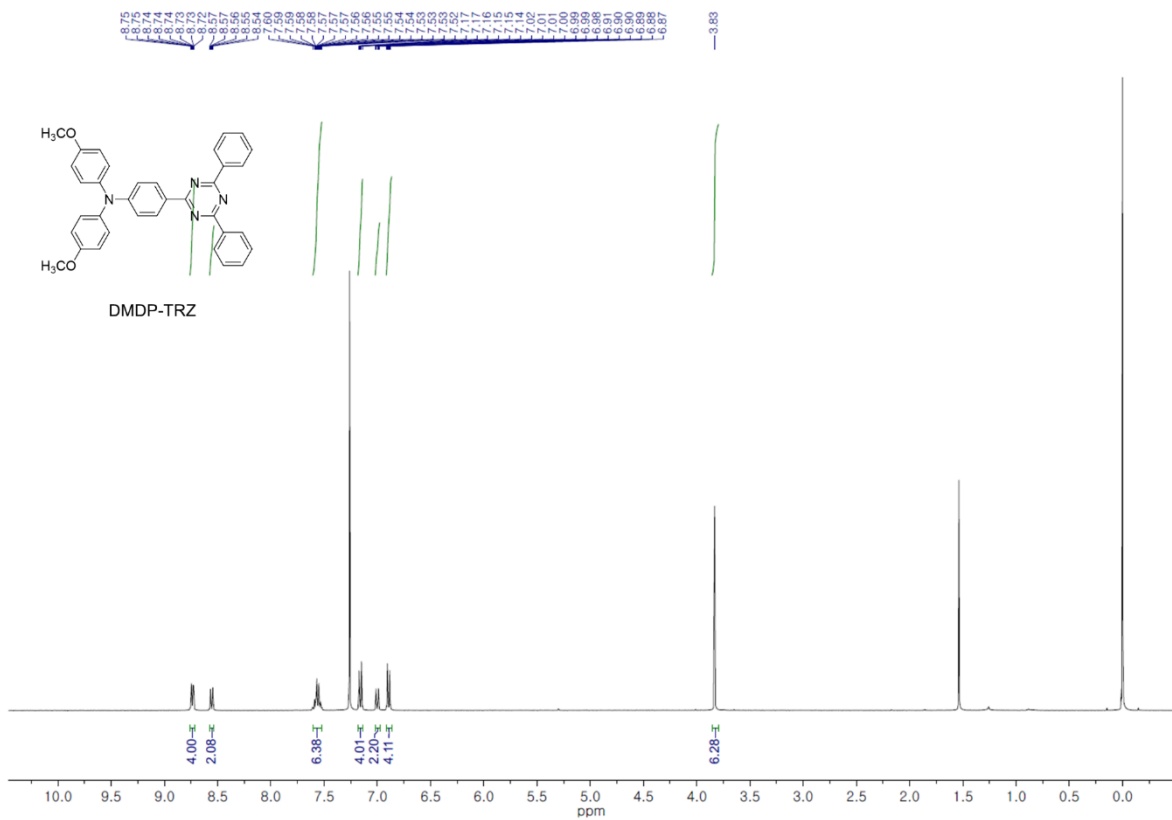


**Figure 52.**  $^1\text{H-NMR}$  of DMDP-TRZ in  $\text{CDCl}_3$  at r.t..

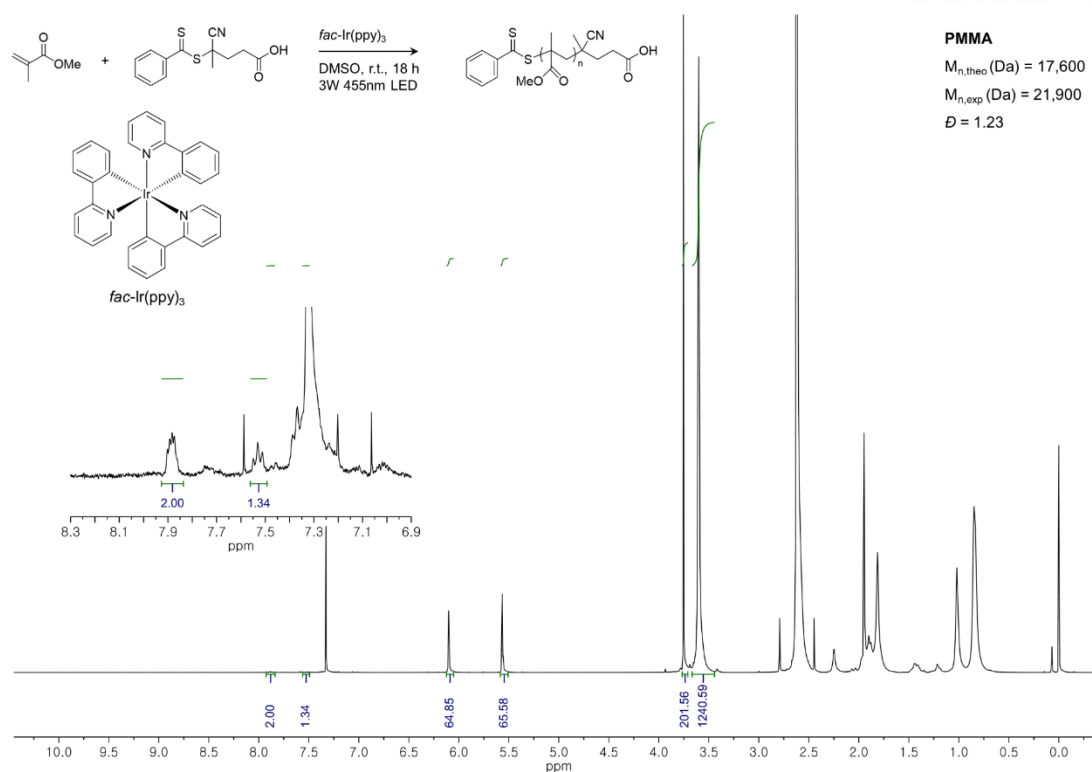


**Figure 53.** In-situ  $^1\text{H-NMR}$  of PMMA in the presence of CPADB, MMA, and  $\text{Ir}(\text{ppy})_3$  of 1 ppm under argon in  $\text{CDCl}_3$  at r.t. (For **Table 2.** entry 1).

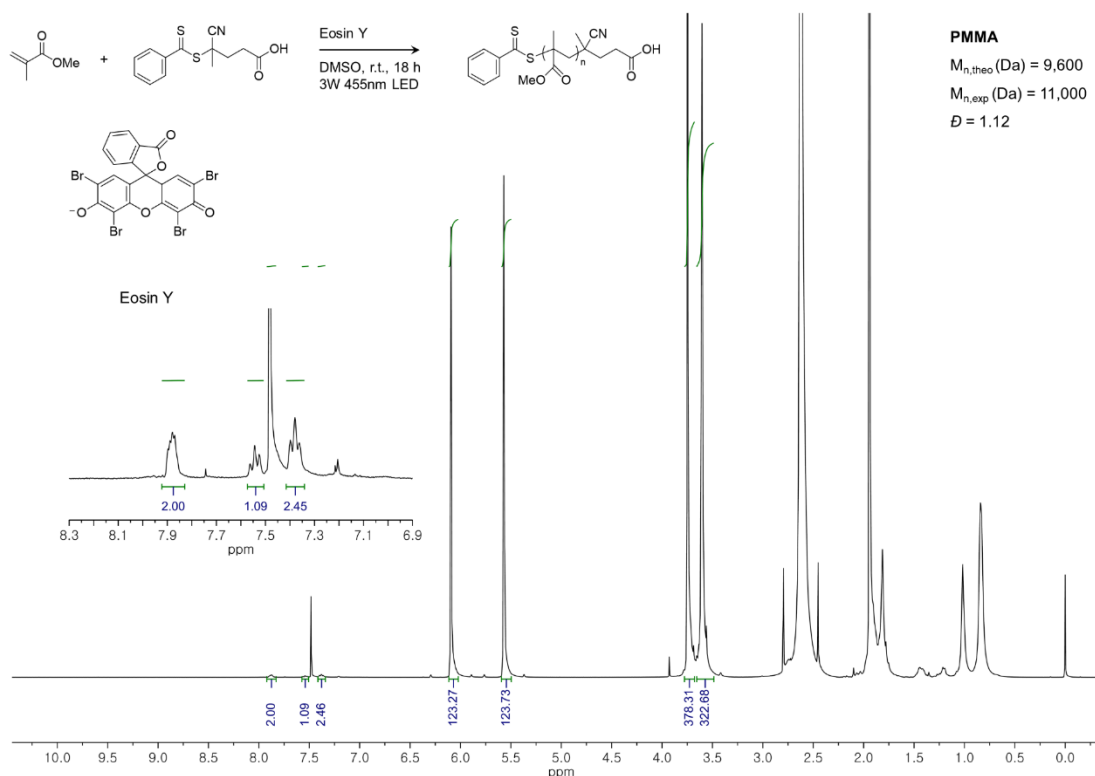


**Figure 54.** In-situ  $^1\text{H-NMR}$  of PMMA in the presence of CPADB, MMA, and eosin Y of 5 ppm under argon in  $\text{CDCl}_3$  at r.t. (For **Table 2.** entry 3).

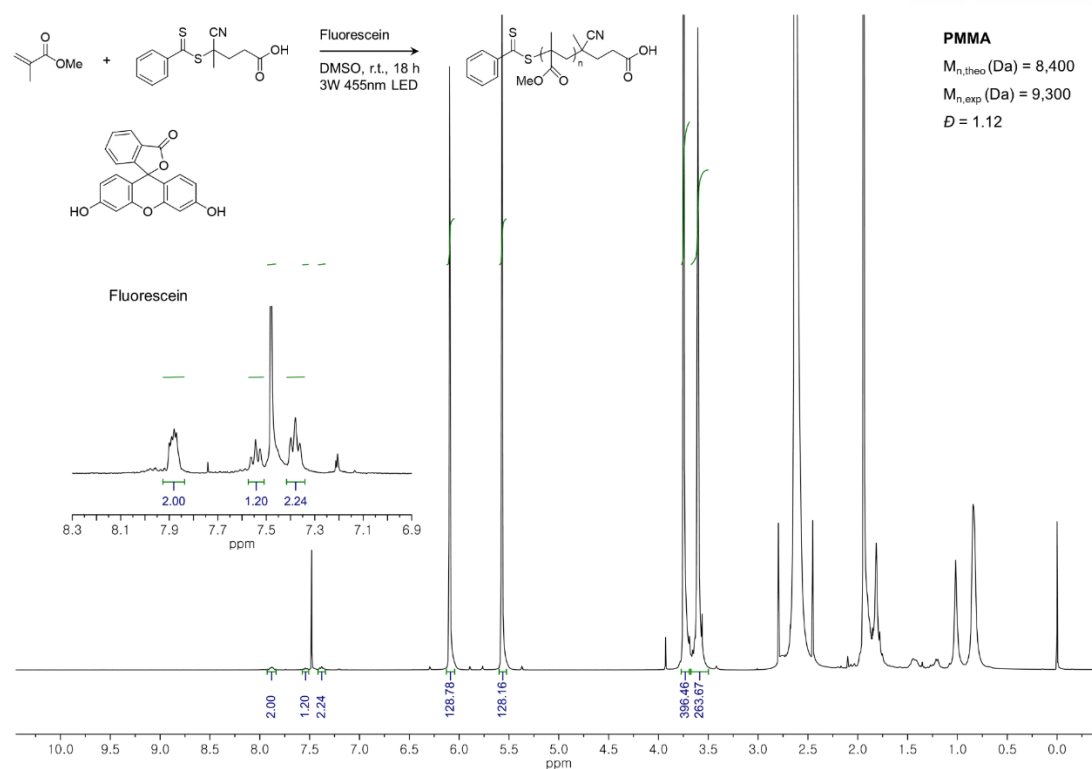


**Figure 55.** In-situ  $^1\text{H-NMR}$  of PMMA in the presence of CPADB, MMA, and fluorescein of 5 ppm under argon in  $\text{CDCl}_3$  at r.t. (For **Table 2.** entry 5).

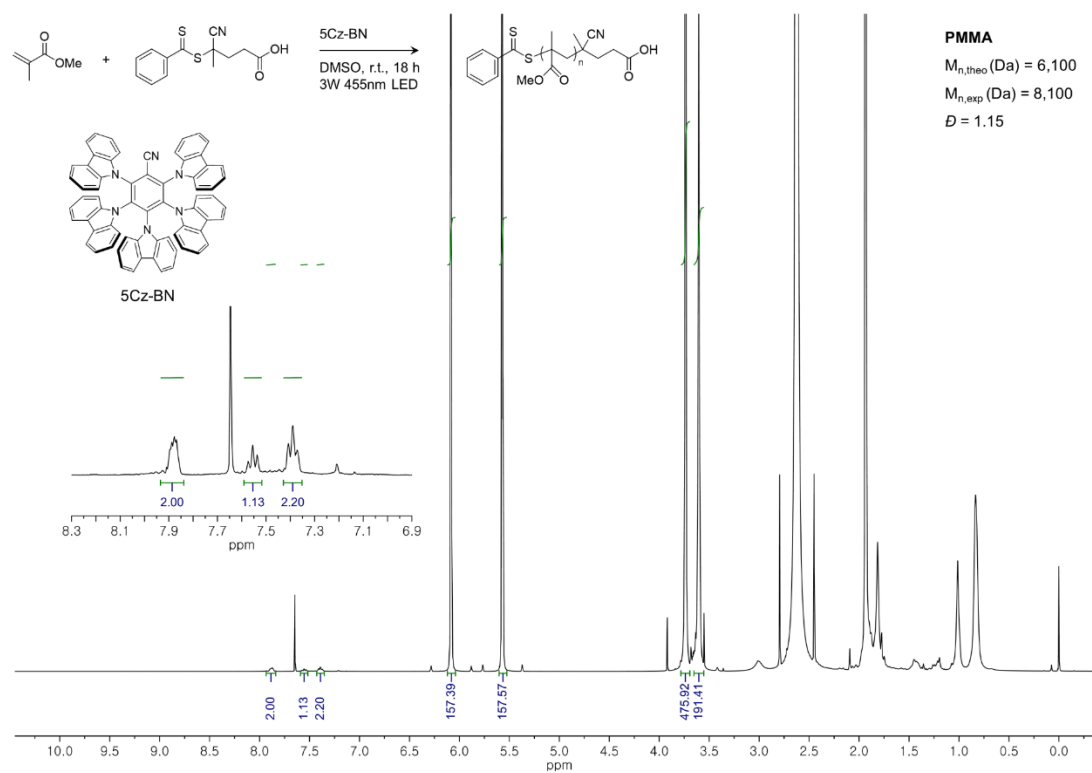


**Figure 56.** In-situ  $^1\text{H-NMR}$  of PMMA in the presence of CPADB, MMA, and 5Cz-BN of 5 ppm under argon in  $\text{CDCl}_3$  at r.t. (For **Table 2.** entry 7).



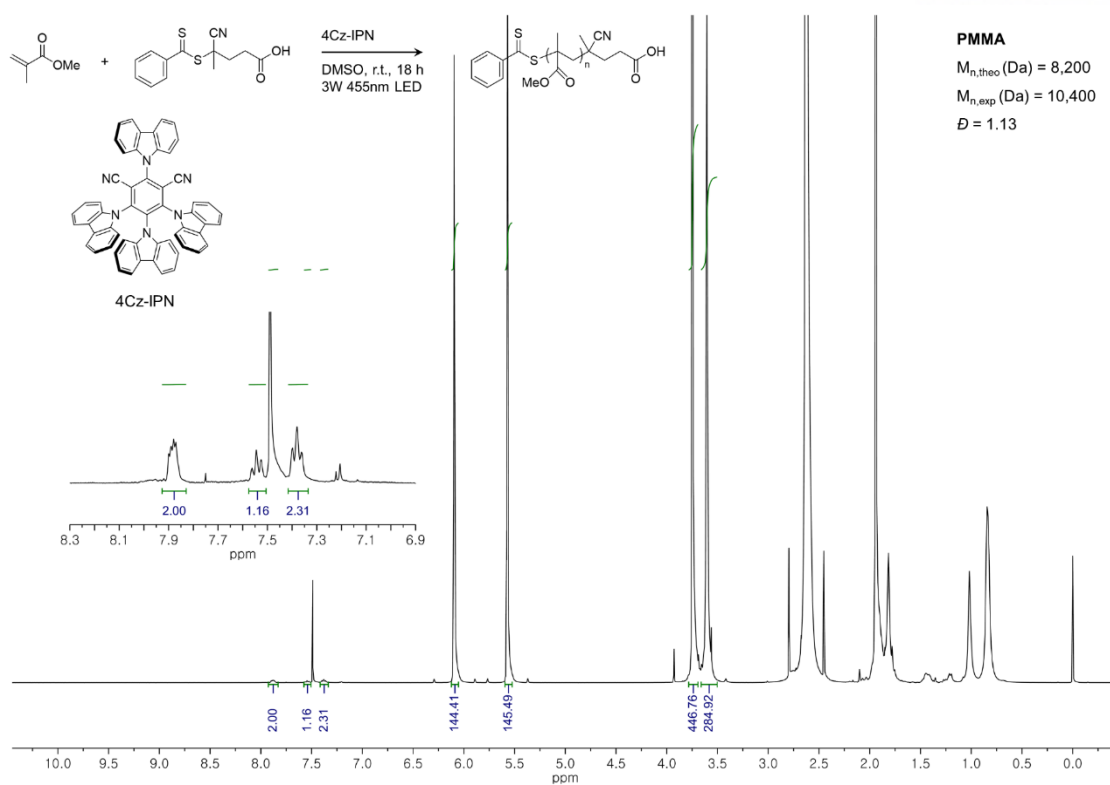


**Figure 57.** In-situ  $^1\text{H-NMR}$  of PMMA in the presence of CPADB, MMA, and 4Cz-IPN of 5 ppm under argon in  $\text{CDCl}_3$  at r.t. (For **Table 2.** entry 9).

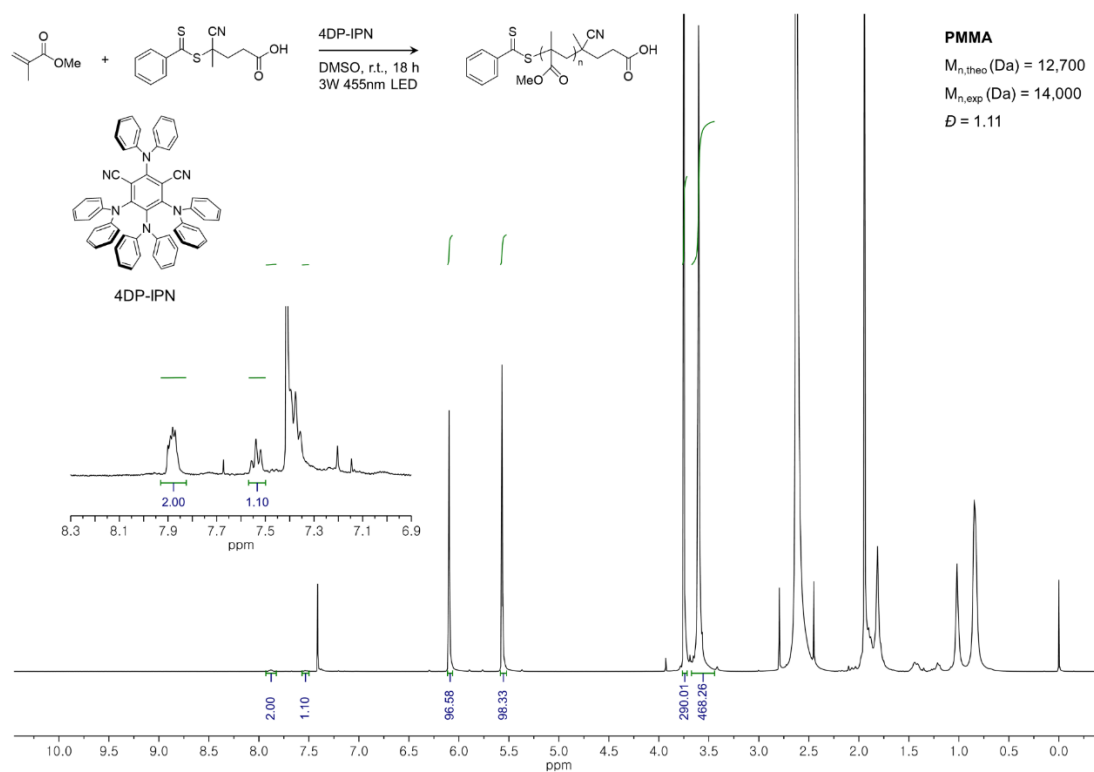


**Figure 58.** In-situ  $^1\text{H-NMR}$  of PMMA in the presence of CPADB, MMA, and 4DP-IPN of 5 ppm under argon in  $\text{CDCl}_3$  at r.t. (For **Table 2.** entry 11).

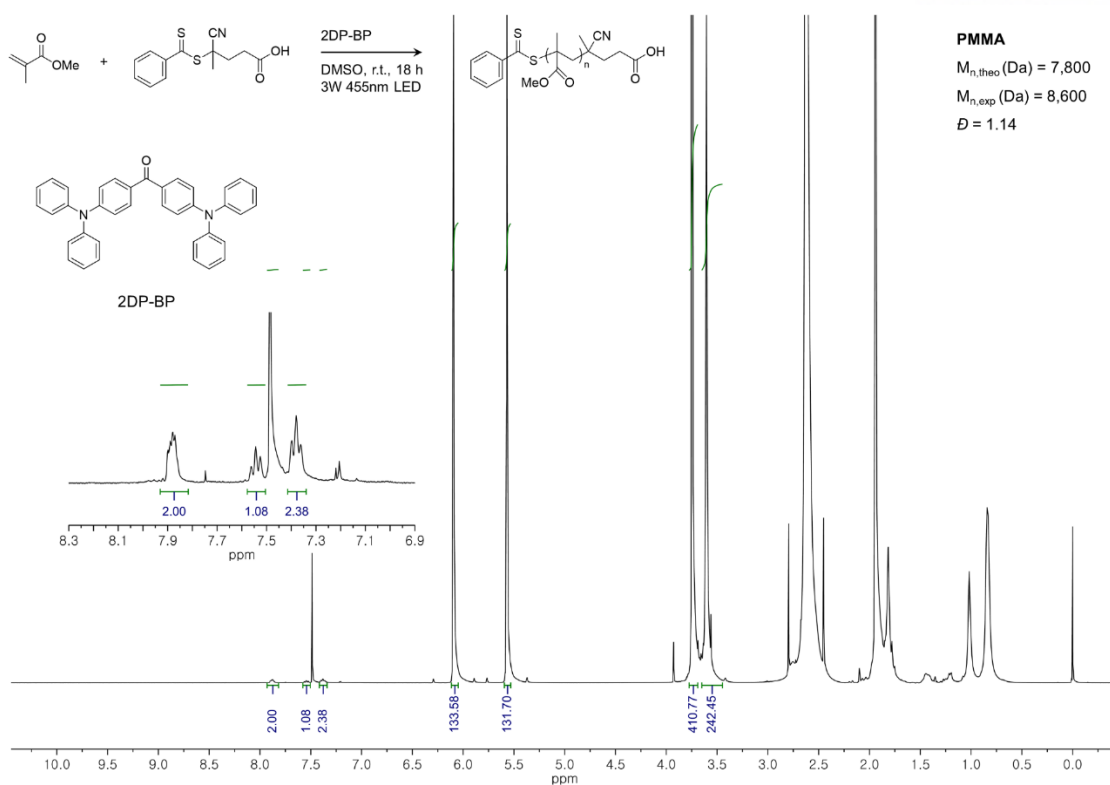


**Figure 59.** In-situ  $^1\text{H-NMR}$  of PMMA in the presence of CPADB, MMA, and 2DP-BP of 5 ppm under argon in  $\text{CDCl}_3$  at r.t. (For **Table 2.** entry 13).

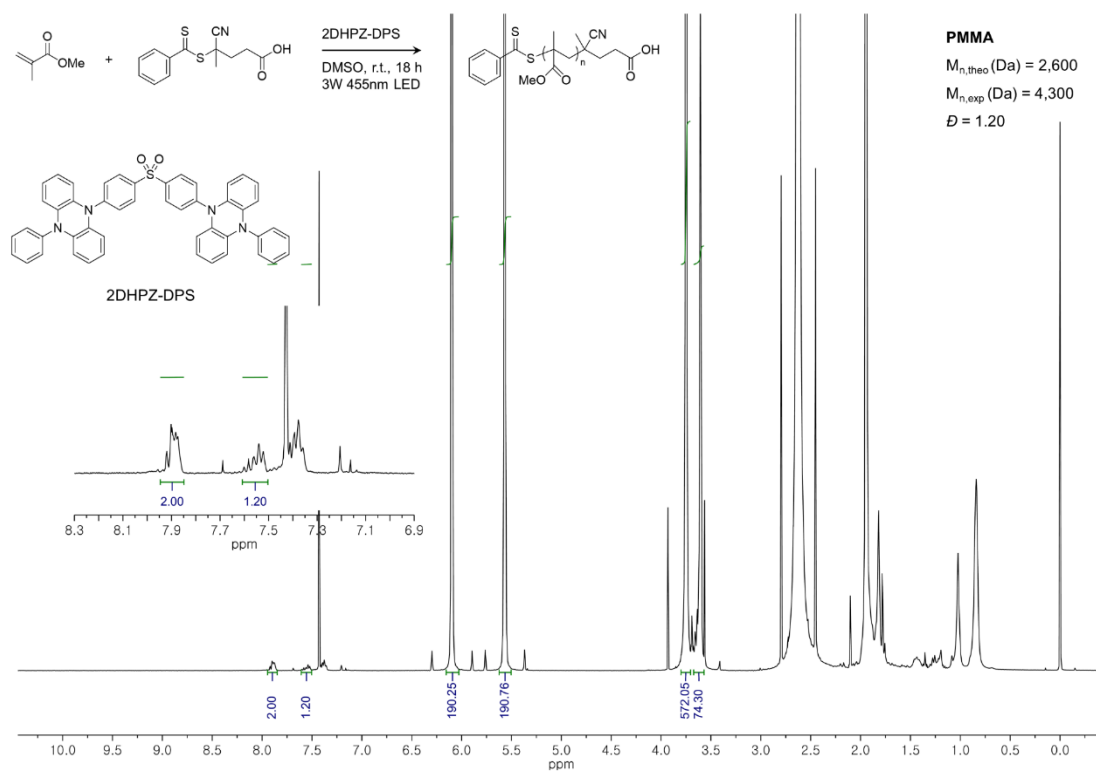


**Figure 60.** In-situ  $^1\text{H-NMR}$  of PMMA in the presence of CPADB, MMA, and 2DHPZ-DPS of 5 ppm under argon in  $\text{CDCl}_3$  at r.t. (For **Table 2.** entry 15).

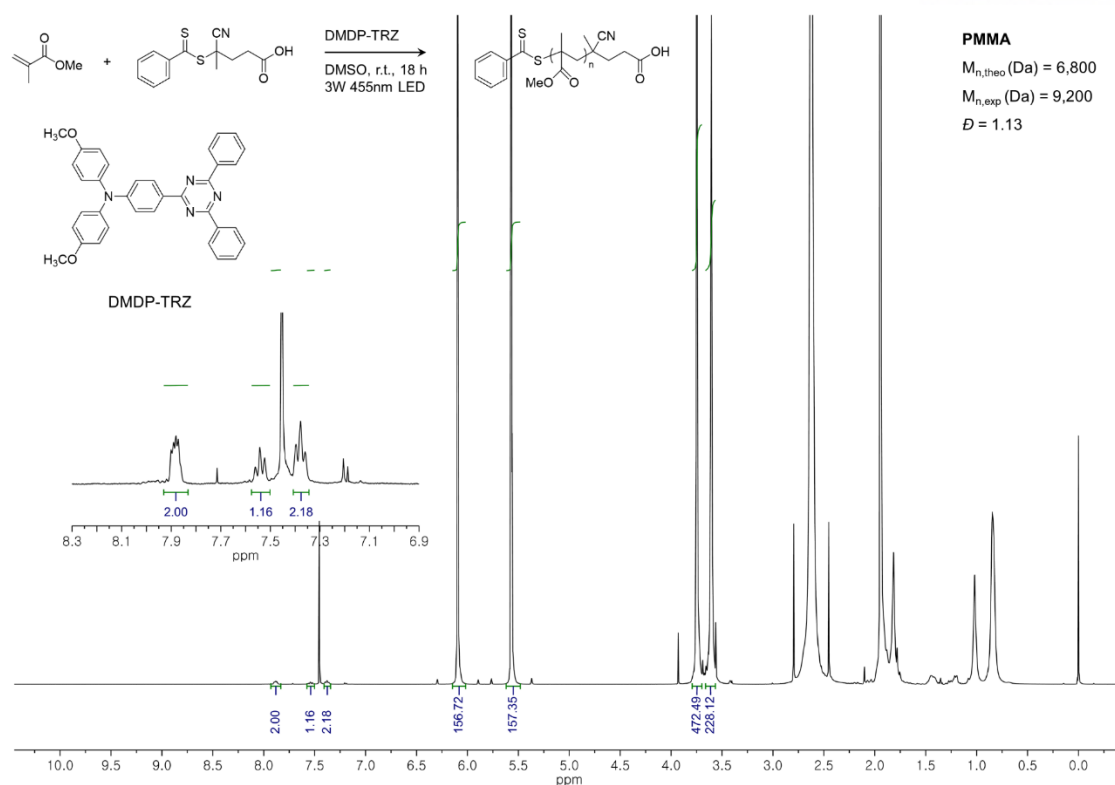


**Figure 61.** In-situ  $^1\text{H-NMR}$  of PMMA in the presence of CPADB, MMA, and DMDP-TRZ of 5 ppm under argon in  $\text{CDCl}_3$  at r.t. (For **Table 2.** entry 17).

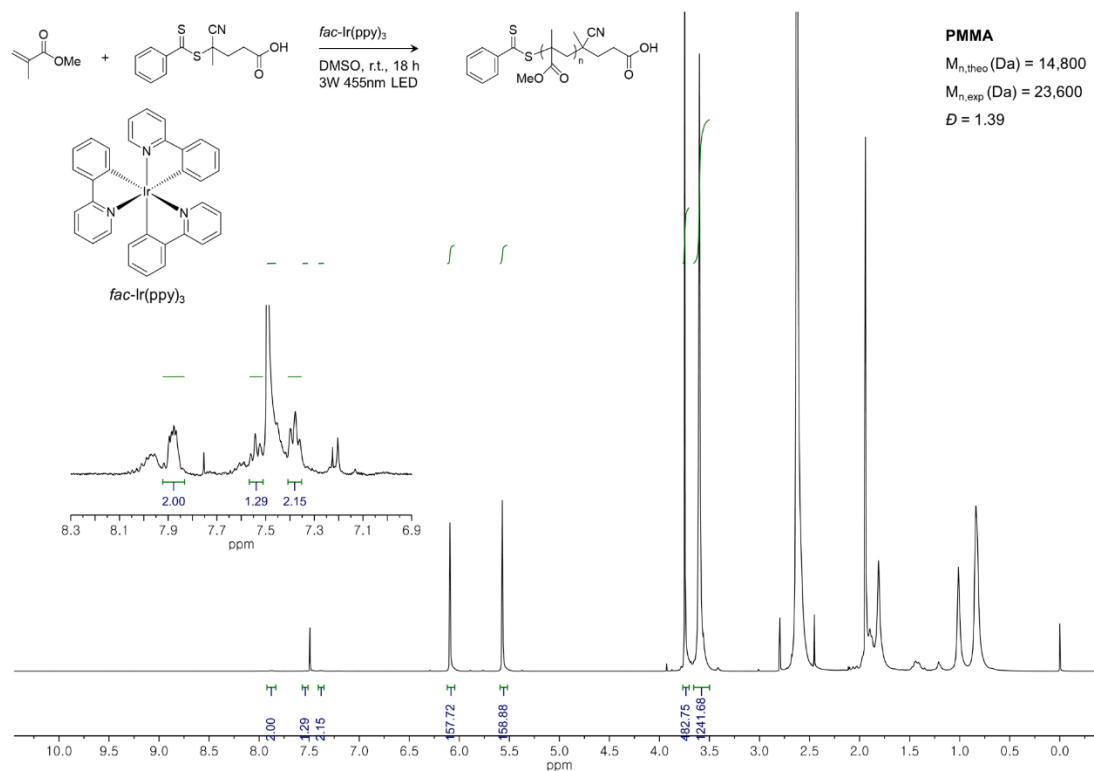


**Figure 62.** In-situ  $^1\text{H-NMR}$  of PMMA in the presence of CPADB, MMA, and  $\text{Ir(ppy)}_3$  of 1 ppm under air in  $\text{CDCl}_3$  at r.t. (For **Table 2.** entry 2).

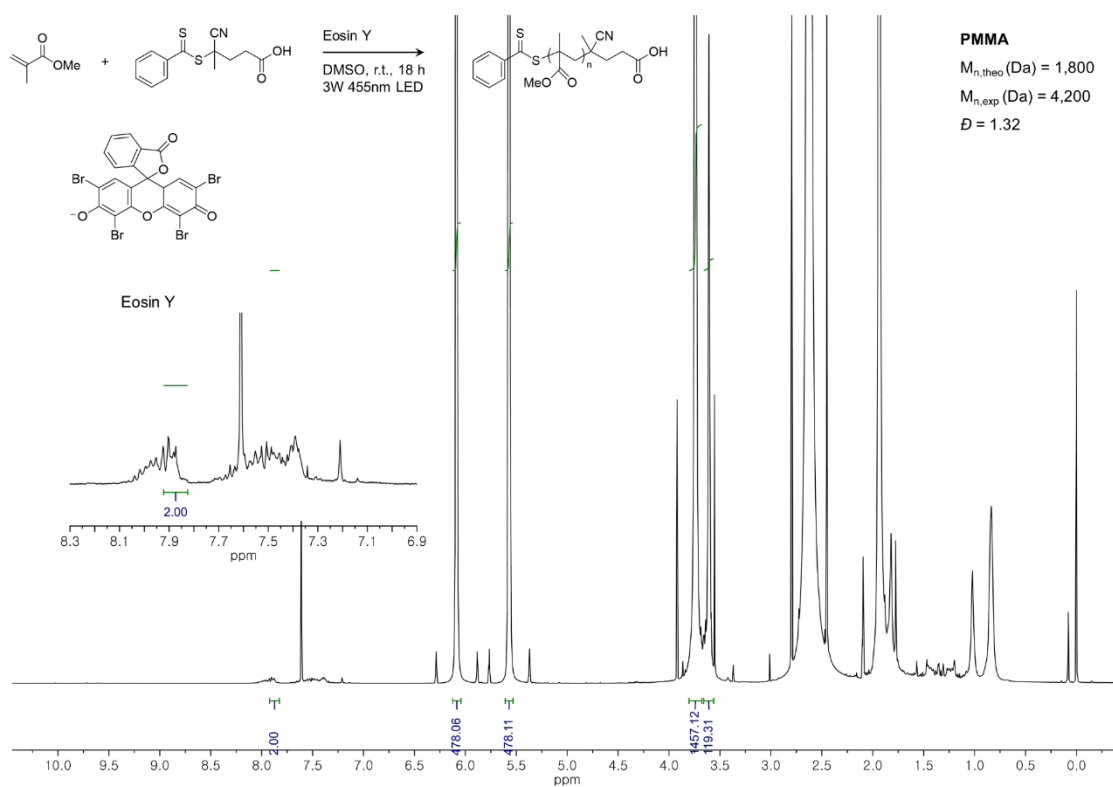


**Figure 63.** In-situ  $^1\text{H-NMR}$  of PMMA in the presence of CPADB, MMA, and eosin Y of 5 ppm under air in  $\text{CDCl}_3$  at r.t. (For **Table 2.** entry 4).

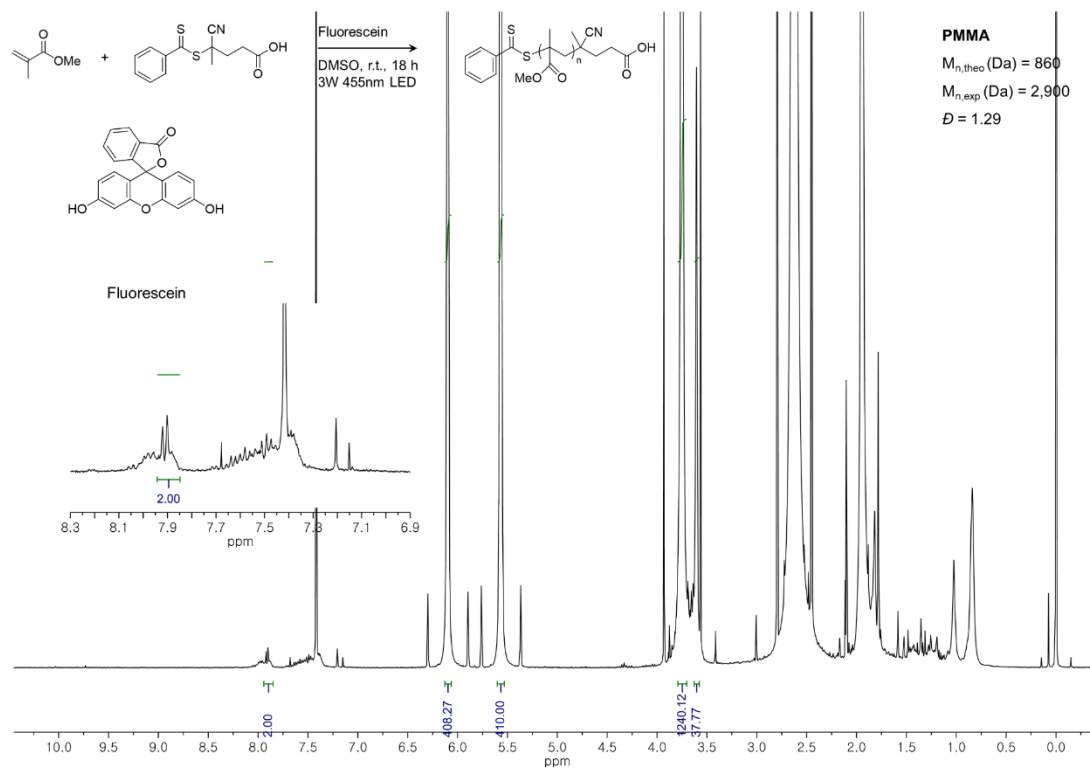


**Figure 64.** In-situ  $^1\text{H-NMR}$  of PMMA in the presence of CPADB, MMA, and fluorescein of 5 ppm under air in  $\text{CDCl}_3$  at r.t. (For **Table 2.** entry 6).

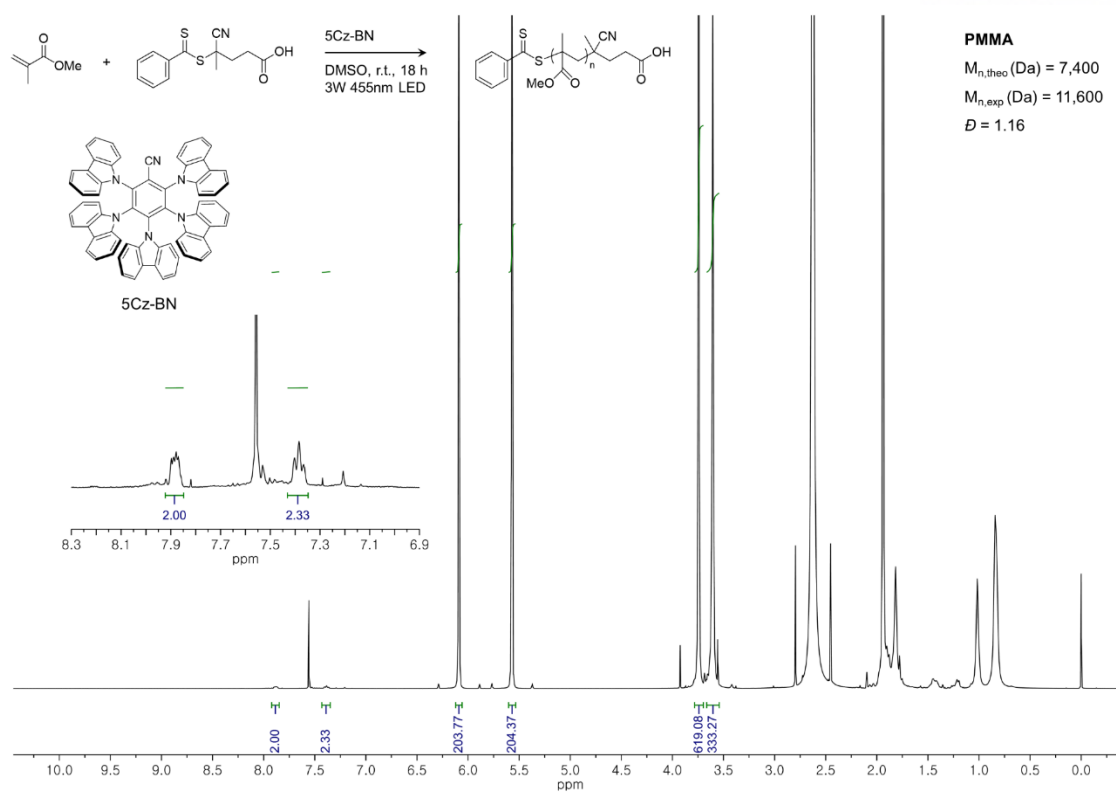


**Figure 65.** In-situ  $^1\text{H-NMR}$  of PMMA in the presence of CPADB, MMA, and 5Cz-BN of 5 ppm under air in  $\text{CDCl}_3$  at r.t. (For **Table 2.** entry 8).

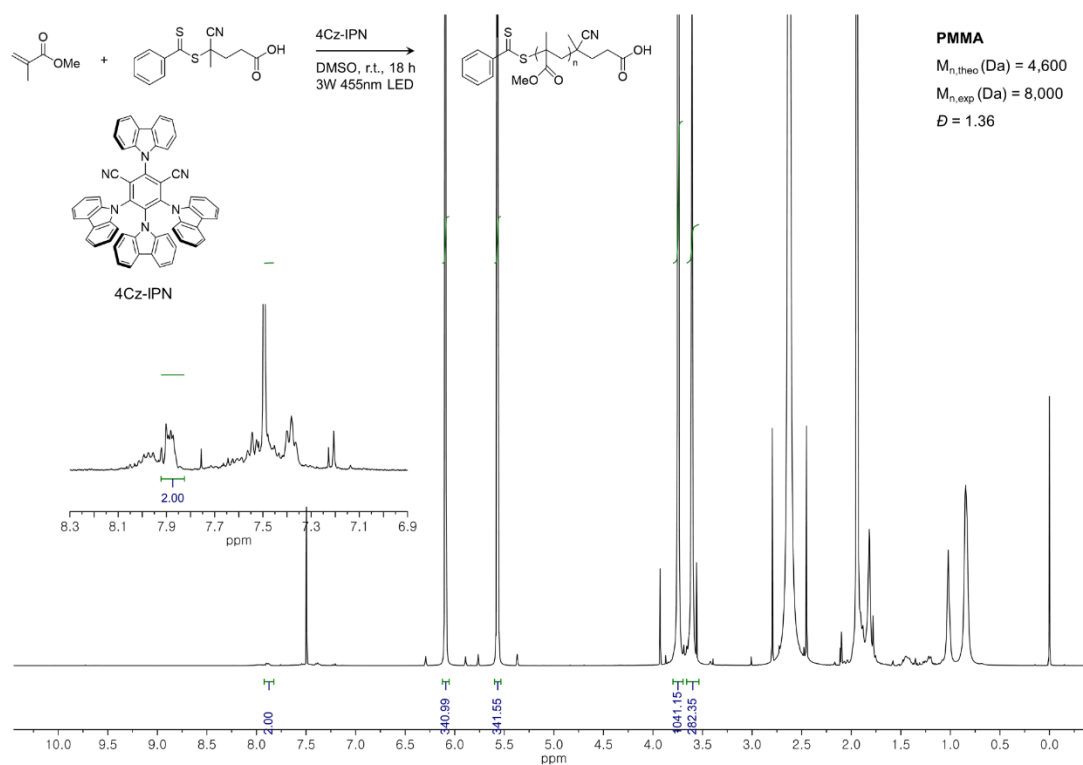


**Figure 66.** In-situ  $^1\text{H-NMR}$  of PMMA in the presence of CPADB, MMA, and 4Cz-IPN of 5 ppm under air in  $\text{CDCl}_3$  at r.t. (For **Table 2.** entry 10).

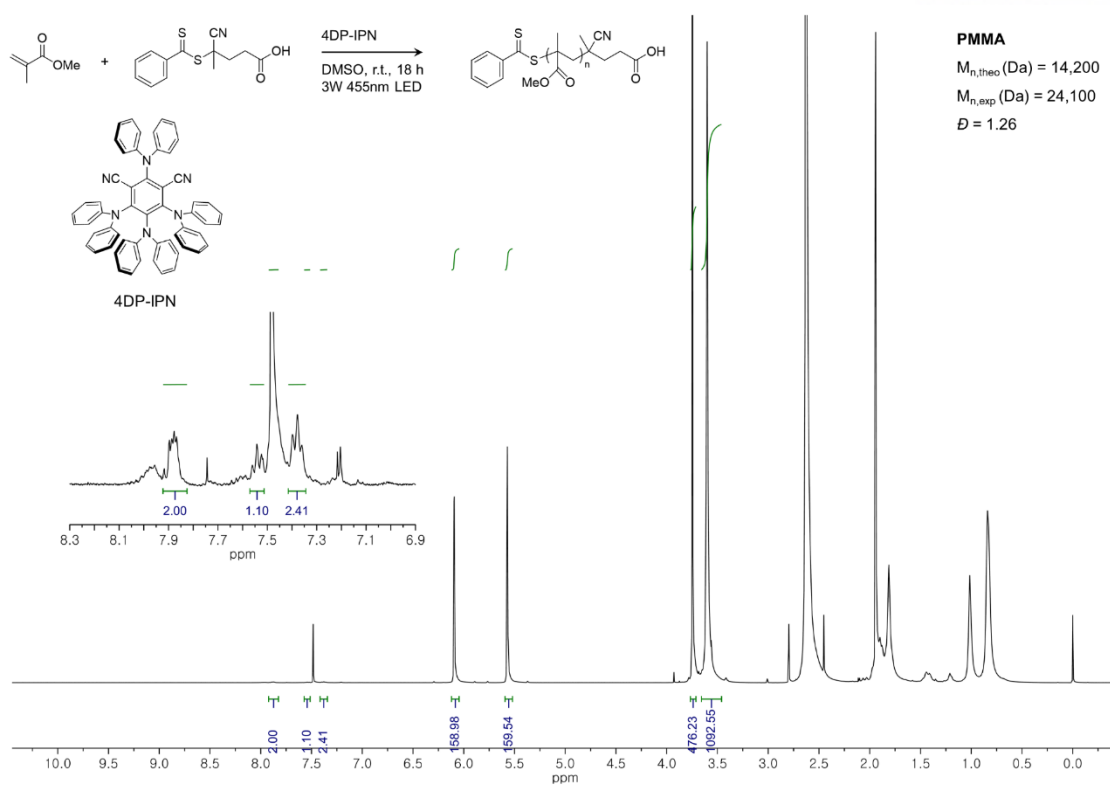


**Figure 67.** In-situ  $^1\text{H-NMR}$  of PMMA in the presence of CPADB, MMA, and 4DP-IPN of 5 ppm under air in  $\text{CDCl}_3$  at r.t. (For **Table 2.** entry 12).

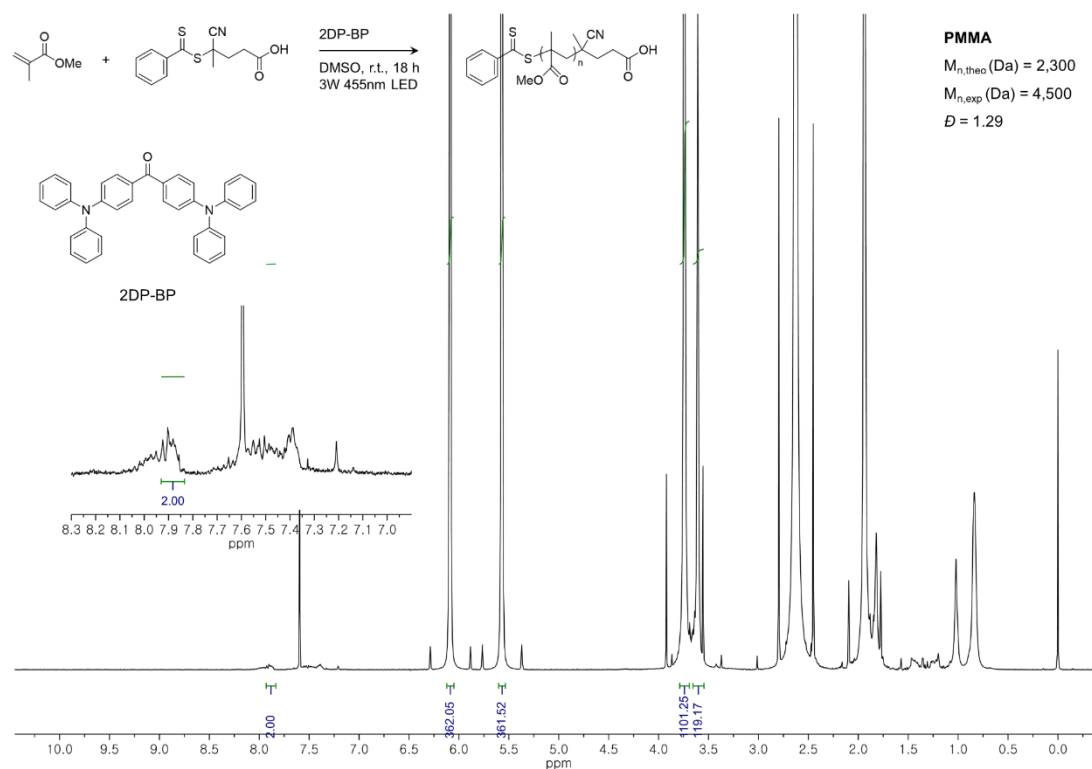


**Figure 68.** In-situ  $^1\text{H-NMR}$  of PMMA in the presence of CPADB, MMA, and 2DP-BP of 5 ppm under air in  $\text{CDCl}_3$  at r.t. (For **Table 2.** entry 14).

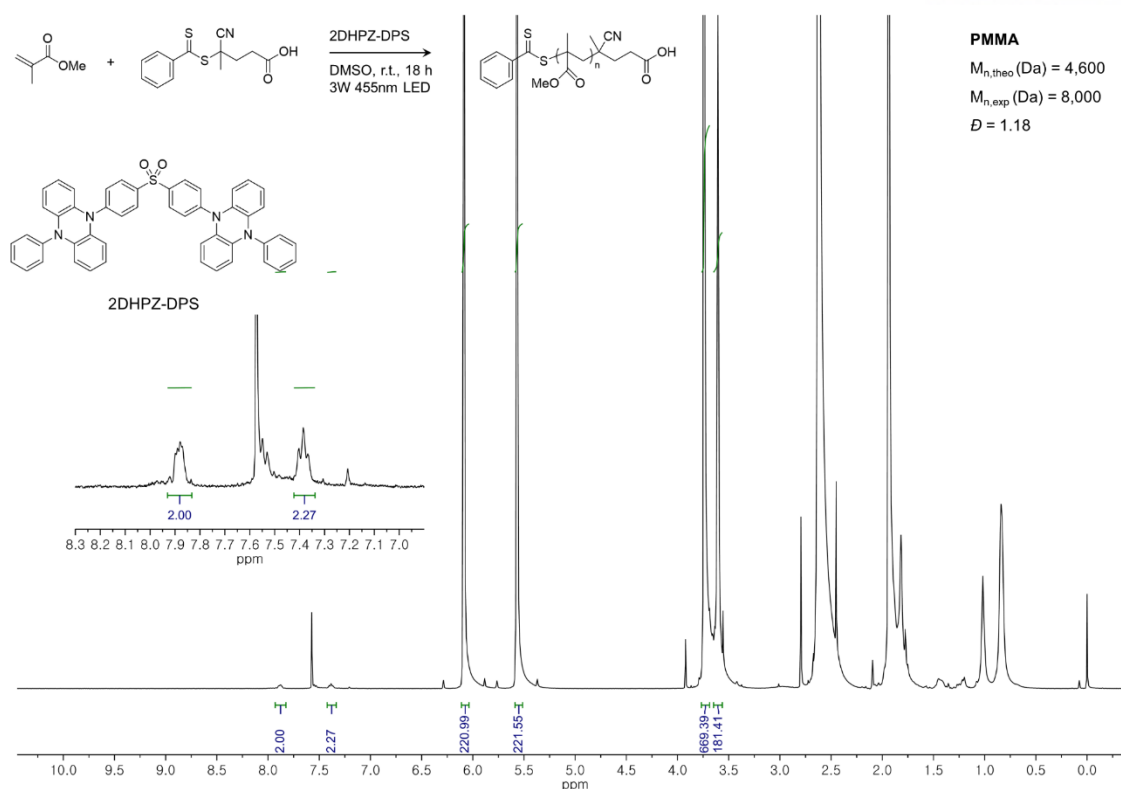


**Figure 69.** In-situ  $^1\text{H-NMR}$  of PMMA in the presence of CPADB, MMA, and 2DHPZ-DPS of 5 ppm under air in  $\text{CDCl}_3$  at r.t. (For **Table 2.** entry 16).

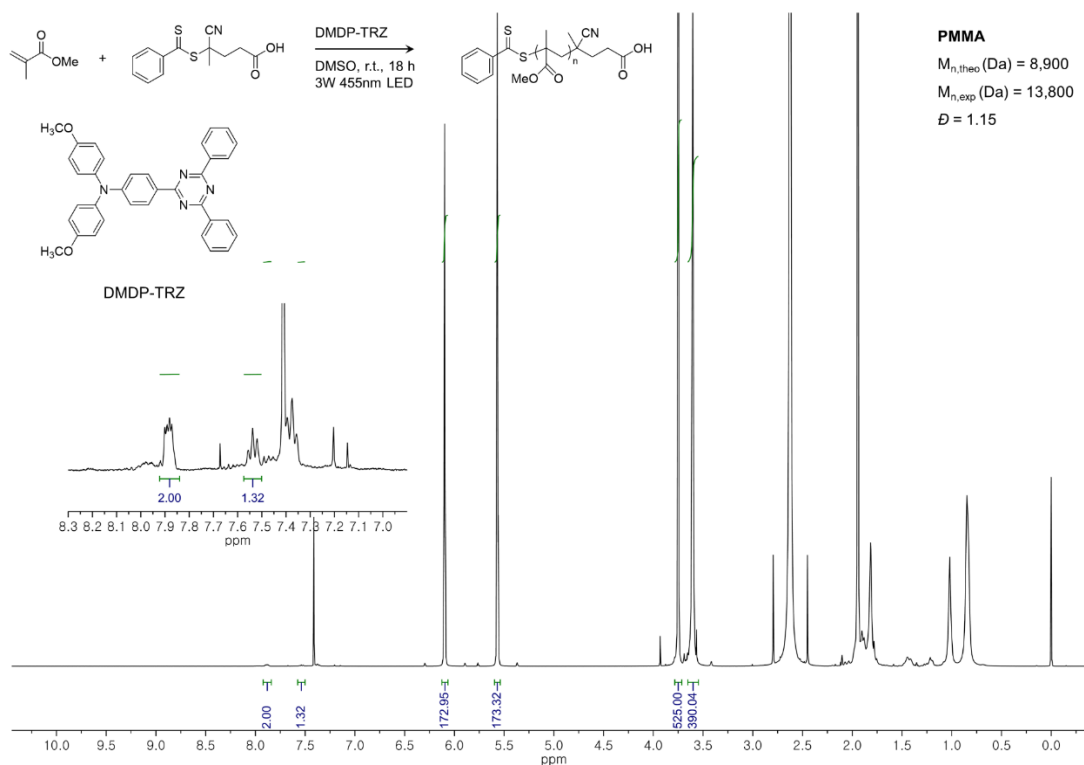


**Figure 70.** In-situ  $^1\text{H-NMR}$  of PMMA in the presence of CPADB, MMA, and DMDP-TRZ of 5 ppm under air in  $\text{CDCl}_3$  at r.t. (For **Table 2.** entry 18).

## V. Conclusion

PET-RAFT polymerization that fulfills the green chemistry is becoming more and more attractive because of its abilities for precision polymer synthesis as well as characteristics from conventional RAFT polymerization. This is a powerful tool, and now, the current interests are focused on the utilization of low-cost and eco-compatible photocatalysts for PET-RAFT polymerization. To improve these aims, a highly efficient visible-light OPCs were successfully identified through a systematic OPC discovery based on a targeted design model. Only sparing amounts of catalyst at ppm-level, that is 5 ppm, for PET-RAFT polymerizations were necessary, that is comparable to those of transition-metal complexes. Due to the high efficiency and the versatility of photocatalysts, we can minimize the use of resources. Moreover, excellent oxygen tolerance was achieved using the discovered OPC combined with trithiocarbonate-based CTA under low-energy light irradiation conditions. Thus, the concerns of monomer loss during degassing are avoided, and cost as well as time would be also reduced on possibly larger scale polymer production. In depth experimental and computational investigations revealed that (1) strong visible-light absorption and efficient generation of long-lived triplet states of the OPC due to its unique molecular structure, and (2) the oxidation stability and no rate retardation of trithiocarbonate-based CTA are the key to the outstanding oxygen tolerance and ppm-level catalyst loadings.

We expect that our work on organocatalyzed PET-RAFT polymerization might resolve various challenging tasks related to polymer synthesis. The next generation of photocatalysts must be able to realize the polymerizations under a ultra-mild condition, that is sun-light irradiation at room temperature system. There may still be some time, but will open new scientific perspectives in medical applications, complex coatings by using highly penetrating irradiation, and industrial polymerization in complex systems such high-pressure reactors and 3D printing.



## VI. References

1. Song, Y.; Kim, Y.; Noh, Y.; Singh, V. K.; Behera, S. K.; Abudulimu, A.; Chung, K.; Wannemacher, R.; Gierschner, J.; Lüer, L.; Kwon, M. S. *Macromolecules* **2019**, 52(15), 5538-5545.
2. Chiefari, J.; Chong, Y. K.; Ercole, F.; Krstina, J.; Jeffery, J.; Le, T. P. L.; Mayadunne, R. T. A.; Meijs, G. F.; Moad, C. L.; Moad, G.; Rizzardo, E.; Thang, S. H. *Macromolecules* **1998**, 31, 5559–5562.
3. Moad, G.; Rizzardo, E.; Thang, S. H. *Chem. – Asian J.* **2013**, 8,1634–1644.
4. Matyjaszewski, K.; Xia, J. *Chem. Rev.* **2001**, 101, 2921–2990.
5. Pan, X.; Tasdelen, M. A.; Laun, J.; Junkers, T.; Yagci, Y.; Matyjaszewski, K. *Prog. Polym. Sci.* **2016**, 62, 73–125.
6. Corrigan, N.; Shanmugam, S.; Xu, J.; Boyer, C. *Chem. Soc. Rev.* **2016**, 45, 6165–6212.
7. Dummur, F.; Gigmès, D.; Fouassier, J.-P.; Lalevée, J. *Acc. Chem. Res.* **2016**, 49, 1980–1989.
8. Dadashi-Silab, S.; Doran, S.; Yagci, Y. *Chem. Rev.* **2016**, 116, 10212–10275.
9. Chen, M.; Zhong, M.; Johnson, J. A. *Chem. Rev.* **2016**, 116, 10167–10211.
10. Asandei, A. D. *Chem. Rev.* **2016**, 116, 2244–2274.
11. Zivic, N.; Bouzrati-Zerelli, M.; Kermagoret, A.; Dumur, F.; Fouassier, J. P.; Gigmès, D.; Lalevée, J. *ChemCatChem* **2016**, 8(9), 1617-1631.
12. Pan, X.; Fantin, M.; Yuan, F.; Matyjaszewski, K. *Chem. Soc. Rev.* **2018**, 47, 5457–5490.
13. Discekici, E. H.; Anastasaki, A.; de Alaniz, J. R.; Hawker, C. J. *Macromolecules* **2018**, 51, 7421–7434.
14. Theriot, J. C.; McCarthy, B. G.; Lim, C.-H.; Miyake, G. M. *Macromol. Rapid Commun.* **2017**, 38, No. 1700040.
15. McKenzie, T. G.; Fu, Q.; Uchiyama, M.; Satoh, K.; Xu, J.; Boyer, C.; Kamigaito, M.; Qiao, G. G. *Adv. Sci.* **2016**, 3, No. 1500394.
16. Yeow, J.; Boyer, C. *Adv. Sci.* **2017**, 4, No. 1700137.
17. Mueller, A. H. E.; Zhuang, R.; Yan, D.; Litvinenko, G. *Macromolecules*, **1995**, 28, 4326–4333.
18. Quinn, J. F.; Barner, L.; Barner-Kowollik, C.; Rizzardo, E.; Davis, T. P. *Macromolecules*, **2002**, 35, 7620–7627.

19. Dietlin, C.; Schweizer, S.; Xiao, P.; Zhang, J.; Morlet-Savary, F.; Graff, B.; Fouassier, J. P.; Lalevée, J. *Polym. Chem.* **2015**, *6*, 3895–3912.
20. Xu, J.; Jung, K.; Atme, A.; Shanmugam, S.; Boyer, C. *J. Am. Chem. Soc.* **2014**, *136*, 5508–5519.
21. Phommalyasack-Lovan, J.; Chu, Y.; Boyer, C.; Xu, J. *Chem. Commun.* **2018**, *54*, 6591–6606.
22. Singh, V. K.; Yu, C.; Badgujar, S.; Kim, Y.; Kwon, Y. H.; Kim, D.; Lee, J.; Akhter, T.; Thangavel, G.; Park, L. S.; Lee, J.; Nandajan, P. C.; Wannemacher, R.; Milián-Medina, B.; Lüer, L.; Kim, K. S.; Gierschner, J.; Kwon, M. S. *Nat. Catal.* **2018**, *1*, 794–804.
23. Chen, M.; MacLeod, M. J.; Johnson, J. A. *ACS Macro Lett.* **2015**, *4*, 566–569.
24. Xu, J.; Shanmugam, S.; Duong, H. T.; Boyer, C. *Polym. Chem.* **2015**, *6*, 5615–5624.
25. Xu, J.; Shanmugam, S.; Fu, C.; Aguey-Zinsou, K.-F.; Boyer, C. *J. Am. Chem. Soc.* **2016**, *138*, 3094–3106.
26. Huang, Z.; Zhang, L.; Cheng, Z.; Zhu, X. *Polymers* **2017**, *9*, 4.
27. Tu, K.; Xu, T.; Zhang, L.; Cheng, Z.; Zhu, X. *RSC Adv.* **2017**, *7*, 24040–24045.
28. Yang, Q.; Zhang, X.; Ma, W.; Ma, Y.; Chen, D.; Wang, L.; Zhao, C.; Yang, W. *J. Polym. Sci., Part A: Polym. Chem.* **2018**, *56*, 229–236.
29. Fu, Q.; Runa, Q.; McKenzie, T. G.; Reyhani, A.; Tang, J.; Qiao, G. G. *Macromolecules* **2017**, *50*, 509–7516.
30. Jiang, J.; Ye, G.; Wang, Z.; Lu, Y.; Chen, J.; Matyjaszewski, K. *Angew. Chem., Int. Ed.* **2018**, *57*, 12037–12042.
31. Gong, H.; Zhao, Y.; Shen, X.; Lin, J.; Chen, M. *Angew. Chem., Int. Ed.* **2018**, *57*, 333–337.
32. Wu, C.; Corrigan, N.; Lim, C.-H.; Jung, K.; Zhu, J.; Miyake, G.; Xu, J.; Boyer, C. *Macromolecules* **2019**, *52*, 236–248.
33. Bagheri, A.; Yeow, J.; Arandiyán, H.; Xu, J.; Boyer, C.; Lim, M. *Macromol. Rapid Commun.* **2016**, *37*, 905–910.
34. Monroe, B. M.; Weed, G. C. *Chem. Rev.* **1993**, *93*, 435 – 448.
35. Avens, H. J.; Bowman, C. N.; *J. Polym. Sci. Part A* **2009**, *47*, 6083 – 6094.
36. Huang, Z.; Zhang, L.; Cheng, Z.; Zhu, X. *Polymers* **2017**, *9*(1), 4.
37. (a) Berberan-Santos, M. N.; Garcia, J. M. M. *J. Am. Chem. Soc.* **1996**, *118*, 9391. (b) Baleizão, C;

- Berberan-Santos, M. N. *J. Chem. Phys.* **2007**, 126, 204510.
38. Roth, H.G.; Romero, A.; Nicewicz, D.A. *Synlett.* **2016**, 27, A-J.
39. Brownson, D. A. C.; Banks, C. E. **2014**.
40. Pavlishchuk, V. V.; Addison, A. W. *Inorg. Chim. Acta* **2000**, 298, 97.
41. Gaussian 09, Revision D.01, Frisch, M. J.; Trucks, G. W.; Schlegel, H. B.; Scuseria, G. E.; Robb, M. A.; Cheeseman, J. R.; Scalmani, G.; Barone, V.; Mennucci, B.; Petersson, G. A.; Nakatsuji, H.; Caricato, M.; Li, X.; Hratchian, H. P.; Izmaylov, A. F.; Bloino, J.; Zheng, G.; Sonnenberg, J. L.; Hada, M.; Ehara, M.; Toyota, K.; Fukuda, R.; Hasegawa, J.; Ishida, M.; Nakajima, T.; Honda, Y.; Kitao, O.; Nakai, H.; Vreven, T.; Montgomery, J. A.; Peralta, J. E.; Ogliaro, F.; Bearpark, M.; Heyd, J. J.; Brothers, E.; Kudin, K. N.; Staroverov, V. N.; Kobayashi, R.; Normand, J.; Raghavachari, K.; Rendell, A.; Burant, J. C.; Iyengar, S. S.; Tomasi, J.; Cossi, M.; Rega, N.; Millam, J. M.; Klene, M.; Knox, J. E.; Cross, J. B.; Bakken, V.; Adamo, C.; Jaramillo, J.; Gomperts, R.; Stratmann, R. E.; Yazyev, O.; Austin, A. J.; Cammi, R.; Pomelli, C.; Ochterski, J. W.; Martin, R. L.; Morokuma, K.; Zakrzewski, V. G.; Voth, G. A.; Salvador, P.; Dannenberg, J. J.; Dapprich, S.; Daniels, A. D.; Farkas, O.; Foresman, J. B.; Ortiz, J. V.; Cioslowski, J.; Fox, D. J. *Gaussian, Inc., Wallingford CT* **2009**.
42. (a) Macchi, G.; Milián Medina, B.; Zambianchi, M.; Tubino, R.; Cornil, J.; Barbarella, G.; Gierschner, J.; Meinardi, F. *Phys. Chem. Chem. Phys.* 2009, 11, 984; (b) Milián Medina, B.; Wasserberg, D.; Meskers, S. C. J.; Mena-Osteritz, E.; Bäuerle, P.; Gierschner, J. *J. Phys. Chem. A* **2008**, 112, 13282.
43. Milián-Medina, B.; Gierschner, J. *Org. Electron.* **2012**, 13, 895.
44. Romero, N. A.; Nicewicz, D. A. *Chem. Rev.* **2016**, 116, 10075–10166.
45. Prier, C. K.; Rankic, D. A.; MacMillan, D. W. C. *Chem. Rev.* **2013**, 113, 5322–5363.
46. Discekici, E. H.; Treat, N. J.; Poelma, S. O.; Mattson, K. M.; Hudson, Z. M.; Luo, Y.; Hawker, C. J.; de Alaniz, J. R. *Chem. Commun.* **2015**, 51, 11705–11708.
47. Bhanu, V. A.; Kishore, K. *Chem. Rev.* **1991**, 91, 99–117.
48. Robertson, C. A.; Hawkins Evans, D.; Abrahamse, H. *J. Photochem. Photobiol., B* **2009**, 96, 1–8.
49. Christmann, J.; Ibrahim, A.; Charlot, V.; Croutxé-Barghorn, C.; Ley, C.; Allonas, X. *ChemPhysChem* **2016**, 17, 2309–2314.
50. Corrigan, N.; Xu, J.; Boyer, C.; Allonas, X. *ChemPhotoChem* **2019**, 3, 1–8.
51. Shanmugam, S.; Xu, J.; Boyer, C. *Macromolecules* **2014**, 47, 4930–4942.
52. Shanmugam, S.; Xu, J.; Boyer, C. *J. Am. Chem. Soc.* **2015**, 137, 9174–9185.

53. McKenzie, T. G.; da M. Costa, L. P.; Fu, Q.; Dunstan, D. E.; Qiao, G. G. *Polym. Chem.* **2016**, *7*, 4246–4253.
54. Sánchez-Arroyo, A. J.; Pardo, Z. D.; Moreno-Jimenez, F.; Herrera, A.; Martin, N.; Garcia-Fresnadillo, D. *J. Org. Chem.* **2015**, *80*, 10575–10584.
55. Li, C.; He, J.; Zhou, Y.; Gu, Y.; Yang, Y. *J. Polym. Sci., Part A: Polym. Chem.* **2011**, *49*, 1351–1360.
56. Perrier, S. *Macromolecules* **2017**, *50*, 7433–7447.
57. Ting, S. R. S.; Davis, T. P.; Zetterlund, P. B. *Macromolecules* **2011**, *44*, 4187–4193.
58. Moad, G. *Macromol. Chem. Phys.* **2014**, *215*, 9–26.